Title

Climate change and California surface hydrology

Author

Schwartz, Marla Ann

Publication Date

2016

UNIVERSITY OF CALIFORNIA

Los Angeles

Climate change and California surface hydrology

A dissertation submitted in partial satisfaction
of the requirements for the degree Doctor of Philosophy
in Atmospheric and Oceanic Sciences

by

Marla Ann Schwartz

2016

ABSTRACT OF THE DISSERTATION

Climate change and California surface hydrology

by

Marla Ann Schwartz

Doctor of Philosophy in Atmospheric and Oceanic Sciences
University of California, Los Angeles, 2016
Professor Alexander Dean Hall, Chair

Understanding 21st century changes in California surface hydrology is critical to ensuring enough freshwater resources for the state's municipal, ecological and agricultural purposes and assessing future ecosystem health and wildfire risk. To project 21st century surface hydrology over California – a region with highly complex topography that is not well captured by global climate models (GCMs) – downscaling is necessary. This work projects future changes in surface hydrology over the Los Angeles and Sierra Nevada regions through dynamical and statistical downscaling techniques.

Dynamical downscaling is employed over Los Angeles to produce 2-km resolution regional projections for the mid-21st-century under an aggressive warming scenario. These projections reveal annual mean runoff and actual evapotranspiration are nearly insensitive to warming. This insensitivity is an artifact of the region's Mediterranean-type climate: Because the warm season receives almost no precipitation, the strongest warming-induced potential evapotranspiration enhancement coincides with dry soils, severely constraining actual evapotranspiration increases. This surprising result highlights that this important semi-arid region is less susceptible to long-term changes in runoff and soil moisture due to its Mediterranean climate.

Over the Sierra Nevada Mountains, dynamical downscaling is used to produce high-resolution (3-km) simulations of end-of-21st-century surface hydroclimate. The high resolution and physical realism of these simulations provides unprecedented detail into the elevational dependence of hydroclimate changes and allows us to examine hydroclimate changes at the watershed level. These downscaled simulations reveal future warming leads to a shift toward significantly earlier snowmelt-driven surface runoff timing at each elevation throughout the Sierra Nevada, particularly in mid-elevations (2000-2750m) in the western and northern Sierra. Moreover, these projections show that any precipitation increases are outweighed by warming induced snowpack reductions and evapotranspiration increases, resulting in statistically significant drying of spring and summer soils and a substantial lengthening of the summer dry period. Relationships and patterns that emerge through dynamical downscaling over the Sierra Nevada are exploited to build simple statistical models that mimic dynamical model behavior. Using this hybrid dynamical-statistical downscaling model, high-resolution end-of-21st-century runoff timing and soil moisture changes are projected for all available GCMs from phase 5 of the Coupled Model Intercomparison Project and the four forcing scenarios adopted by the Intergovernmental Panel on Climate Change's Fifth Assessment Report. These multi-model projections allow us to quantify and characterize ensemble-mean changes and the associated uncertainty due to inter-model GCM spread, as well as the consequences associated with choice of emissions scenario. Averaged across the Sierra, April-September soil moisture is projected to decrease 17.1% in the 35-model ensemble mean under RCP8.5 (with an approximate intermodel range of -12.9% to -21.0%), but only 9.1% with an approximate intermodel range of -5.7% to -12.9%) under RCP4.5, a reasonable mitigation scenario.

The dissertation of Marla Ann Schwartz is approved.

Steven A. Margulis

J. David Neelin

Ulrike Seibt

Alexander Dean Hall, Committee Chair

University of California, Los Angeles

2016

Contents

List of Figures

List of Tables

ACKNOWLEDGMENTS

The material in Chapter 2 is a version of a manuscript in review and conditionally accepted for publication in Journal of Climate. The manuscript title is “Mean surface runoff insensitive to warming in a key Mediterranean-type climate: A case study of the Los Angeles Region,” co-authored with Alex Hall and Fengpeng Sun. Support for this work was provided by the City of Los Angeles and the US Department of Energy as part of the American Recovery and Reinvestment Act of 2009. Additional funding was provided by the National Science Foundation (Grant #EF-1065863, Collaborative Research: Do Microenvironments Govern Macroecology?).

Chapter 3 is a draft of a manuscript in progress to be co-authored with Alex Hall, Fengpeng Sun, Daniel Walton and Neil Berg. The manuscript title is “Significant and inevitable end-of-21st-century advances in surface runoff timing in California’s Sierra Nevada.” Chapter 4 is a draft of a manuscript in progress to be co-authored with Neil Berg, Alex Hall, Fengpeng Sun and Daniel Walton. The manuscript title is “Future soil moisture drying in the Sierra Nevada.” Support for Chapters 3 and 4 was provided by the Metabolic Studio in partnership with the Annenberg Foundation (Grant #12-469: Climate Change Projections in the Sierra Nevada) and the US Department of Energy (Grant #DE-SC0014061: Developing Metrics to Evaluate the Skill and Credibility of Downscaling).

I would like to thank Alex Hall for his guidance and insight, which have been instrumental in the development of this work. I also thank Steve Margulis, David Neelin and Ulli Seibt for their helpful comments and suggestions on this research. Lastly, thank you to my fellow students, officemates and colleagues for discussions and support (both scientific and comedic) along the way.

Marla Ann Schwartz

Los Angeles, California
May 2016

Marla Ann Schwartz

EDUCATION

University of California, Los Angeles, CA

M.S., Atmospheric and Oceanic Sciences, June 2013

Columbia University, New York, NY

B.A., Mathematics, May 2010

FELLOWSHIPS AND AWARDS

Morris Neiburger Award for excellence in graduate teaching (UCLA AOS), 2015

Brian Bosart Memorial Award for service to students and the department (UCLA AOS), 2015

Global Environment Teaching Fellowship, UCLA Institute of the Environment & Sustainability, 2012-2013

Graduate Research Summer Fellowship (UCLA AOS), Summer 2011

Edwin W. Pauley Fellowship, UCLA, 2010-2011

PUBLICATIONS

Sun F., A. Hall, M. Schwartz, D. Walton and N. Berg, 2015: Twenty-first-century snowfall and snowpack changes over the southern California Mountains. Journal of Climate, 29, 91-110. doi:10.1175/JCLI- D-15-00199.1.

Schwartz, M., Mid-21st century changes to surface hydrology over the Los Angeles Region, 2013: Master's Thesis, University of California, Los Angeles. Available online at http://escholarship.org/uc/item/8zt5x06t.

1 Research Overview

The overarching goal of this work is to investigate 21st-century changes in California surface hydrology. Global climate models (GCMs) provide insight into future hydroclimate trends, but their coarse resolution fails to capture climatic variables at a scale necessary for regional-scale analysis (Giorgi and Mearns 1991; Leung et al. 2003). The latest generation of GCMs in the World Climate Research Programme's Coupled Model Intercomparison Project Phase 5 (CMIP5; Taylor et al. 2012) have horizontal resolutions between 1° to 2.5° (~ 100 – 250 km). California's complex coastlines and topographical features show variation on much smaller scales and play a dominant role in shaping regional-scale processes, including orographic precipitation, land-sea breezes and valley circulations. Such regional-scale processes have been shown to be critical in understanding climate variability in California (Cayan, 1996; Conil and Hall, 2006; Hughes et al. 2007). Thus, current GCM resolution is far too low to understand surface hydrology at scales relevant for climate change adaptation and planning.

These limitations have motivated efforts to regionalize GCM climate change signals to much higher spatial resolutions through a variety of downscaling methods (Giorgi et al. 1994, Snyder et al. 2002, Timbal et al. 2003, Hayhoe et al. 2004, Leung et al. 2004, Tebaldi et al. 2005, Duffy et al. 2006, Salathé et al. 2010, Pierce et al. 2013a). Downscaling aims to determine how large-scale climate change signals are expressed on higher resolution spatial scales.

Downscaling is typically done either (1) dynamically, in which a regional climate model is forced at the boundaries by coarse-resolution reanalysis or GCM output, or (2) statistically, in which empirical relationships between large-scale predictors and regional-scale predictands are developed. Statistical downscaling has aided previous studies of climate change impacts to surface hydrology, and its low computational cost allows statistical downscaling to be quickly applied to many GCMs and forcing scenarios (Pierce and Cayan 2013). However, statistical downscaling methods have been criticized because they may miss key physical processes such as snow albedo feedback (Walton et al. 2016) and may show substantially reduced accuracy when applied to a warmer climate (Gutierrez et al. 2013).

Dynamical downscaling directly simulates complex fine-scale physical processes that emerge from California's topography and coastlines, like orographic precipitation, snowpack accumulation and melt, land-sea breezes and valley circulations. Having more physically realistic simulation of these key inputs should improve modeling of surface hydrology throughout California. However, running a regional climate model is very computationally expensive. As a result, dynamical downscaling studies are usually limited to only one or two downscaled GCMs or Representative Concentration Pathway (RCP) forcing scenarios adopted by the Intergovernmental Panel on Climate Change's Fifth Assessment Report (IPCC AR5). This provides limited information to quantify and characterize uncertainty in future surface hydrology projections due to inter-model GCM spread, as well as the consequences associated with choice of emissions scenario.

Perhaps due to the computational demands of regional climate models, there have been limited downscaling-based CMIP5 analyses of 21st century changes to surface hydrology over California. The overarching goal of this work is to employ downscaling techniques to make high-resolution multi-model projections of climate change at the regional scale for both the Los Angeles region (Chapter 2) and Sierra Nevada Mountains (Chapters 3-5), a high-elevation mountain range whose seasonal snow cover represents a critical water resource for California.

Through these projections, we investigate 21st-century effects of anthropogenic climate change to California surface hydrology.

Chapter 2 employs dynamical downscaling to investigate the sensitivity of surface hydrology in the Los Angeles region to climate change. We produce 2-km resolution regional projections for the mid-21st century (2041-2060) under the "business-as-usual" (RCP8.5) forcing scenario for five CMIP5 GCMs. Future projections are compared to a validated reanalysis-driven simulation of a baseline period (1981-2000) to quantify surface hydrology changes. Precipitation changes are likely to be small and are within the range of baseline interannual variability. Runoff changes are strongly controlled by precipitation changes, suggesting temperature-driven changes in actual evapotranspiration are small. A series of temperature sensitivity experiments are performed in which a land surface model is forced by the meteorology of the baseline period, but with uniform near-surface air temperature increases of 2º, 4º and 6º C. Results from these idealized experiments reveal annual mean actual evapotranspiration and runoff are nearly insensitive to warming. This insensitivity is an artifact of the region's Mediterranean-type climate: Because the warm season receives almost no precipitation, the strongest warming-induced potential evapotranspiration enhancement coincides with dry soils, severely constraining actual evapotranspiration increases. Surface hydrology in other Mediterranean climate regions may respond similarly. This result greatly mitigates a potential vulnerability of water resources to a changing climate in an important semi-arid region of the world. It also reveals that a regional climate change adaptation strategy relying on local water resources is a viable one.

Chapter 3 produces runoff timing projections for California's Sierra Nevada. First, future climate change projections (RCP8.5 forcing scenario, 2081–2100 period) from five CMIP5 GCMs are downscaled dynamically. These projections reveal that future warming leads to a shift toward earlier snowmelt-driven surface runoff timing throughout the Sierra Nevada. Relationships between warming and surface runoff timing from the dynamical simulations are used to build a simple statistical model that mimics the dynamical model's projected runoff timing changes given GCM or downscaled warming as input. Using this statistical model, we project high-resolution end-of-21st-century runoff timing changes for all available CMIP5 GCMs and the four forcing scenarios adopted by the IPCC AR5. These multi-model projections allow us to quantify ensemble-mean runoff timing changes and its uncertainty due to both intermodel variability and choice of forcing scenario. Under a business-as-usual forcing scenario (RCP8.5), the ensemble mean domain-average advance in runoff timing is nearly 50 days, which is highly likely to be a detectable shift in runoff timing that is significantly distinct from interannual climate variability. Changes to surface runoff timing projected in this study have implications for surface hydrology, water resources and ecosystems.

Chapter 4 examines soil moisture in California's Sierra Nevada, which plays a key role in the region's climate and affects wildfire risk, ecosystem health and agriculture in the surrounding areas. A hybrid dynamical-statistical technique that incorporates aspects of both dynamical and statistical downscaling techniques is used to project high-resolution (3-km) future changes to Sierra Nevada soil moisture. First, we dynamically downscale end-of-21st-century climate change signals from five GCMs under RCP8.5. These projections reveal that any precipitation increases are outweighed by warming induced snowpack reductions and evapotranspiration increases, resulting in statistically significant drying of spring and summer soils. Next, relationships between soil moisture, snowpack and near-surface warming from the dynamical simulations are exploited to build a statistical model that can project future soil moisture for any GCM. This statistical model is applied to all available CMIP5 GCMs and RCPs, producing an ensemble that allows for robust estimates of most likely soil moisture changes and uncertainty quantification. For all GCMs and RCPs, strong April-September soil moisture drying occurs at elevations between 2000-2500m, despite increasing precipitation in many GCMs. Averaged across the Sierra, April-September soil moisture is projected to decrease -14.9% in the 35-model ensemble mean under RCP8.5, substantially increasing the length of the summer dry period.

Chapter 5 relies on the dynamically downscaled multi-model end-of-21st-century surface runoff timing projections from Chapter 3. We examine important elevational-variations in warming-driven runoff timing changes to explore whether individual watersheds in the Sierra Nevada Mountain Range will respond to climate change differently due to the non-uniform expression of climate change across the landscape or inherent physical watershed characteristics. Through this exploration, we find that the greatest advances in surface runoff timing are found at elevations between 1800m to 2500m. We also explore watershed-average changes in runoff timing, finding runoff timing in watersheds with mean elevations close to the historical snowline (or with a large portion of area close to this snowline) are most sensitive to future warming scenarios. This sensitivity arises because those watersheds have regions with elevations high enough to sustain and accumulate seasonal snow cover (that contributes to snowmelt-driven surface runoff) but not cold enough to remain below freezing under warming scenarios. This quantitative information at the watershed scale is critical for water management, and helps to bridge the gap between the climate modeling community and state water planners.

Collectively, these downscaling-based assessments of the CMIP5 ensemble’s projections over the Los Angeles and Sierra Nevada Mountain regions offer a high-resolution picture of future regional hydroclimate and investigate the response of California surface hydrology to future climate change.

2 Mean surface runoff insensitive to warming in a key Mediterranean-type climate: A case study of the Los Angeles Region

2.1 Introduction

Mediterranean-type climate zones (California, lands around the Mediterranean Sea, central Chile, southwestern South Africa, and southwestern and southern Australia) are characterized by warm, dry summers and cool, rainy winters (Myers et al. 2000; Cowling et al. 2005; Kottek et al. 2006). The florae of these regions are among the world's richest, harboring almost 20% of all known vascular plant species despite occupying less than 5% of the earth's surface (Cowling et al. 1996). Mediterranean-type climate regions have also been recognized as particularly threatened by global climate change (IPCC 2014).

A potentially unique surface hydrological response to climate change may arise from the seasonality of Mediterranean-type hydrology. Projected temperature increases, along with increased downward longwave radiation from greater concentrations of greenhouse gases, would enhance potential evapotranspiration (PET), the amount of water that would evaporate and transpire given an unlimited supply of surface water. As we will show, the PET enhancement is especially large in the warm months. However, because rain comes during the cool months, soil moisture levels are low during the warm months. As a result, the time of the strongest PET enhancement may coincide with the driest soils. Thus it is unclear whether actual evapotranspiration (AET) will respond strongly to warming. Surface runoff may likewise be only weakly affected by warming. Therefore, it is important to investigate how climate-change induced temperature and precipitation changes will impact surface hydrology in Mediterranean-type climate regions.

This study explores the hydrologic response of California's Los Angeles region as a case study. Previous studies have documented observed changes in California's hydroclimate over the past few decades, as well as potential future changes to hydrology and water resources in the western United States (Roos 1991; Hamlet et al. 2005; Maurer 2007; Barnett et al. 2008; Bates et al. 2008; Adam et al. 2009; Kapnick and Hall 2010). However, a high-resolution assessment of the response of surface hydrology in the Los Angeles region to future climate change has not been done before.

This study is informative due to its implications for other Mediterranean-type climate zones, and it is crucial for informed local water resources planning. The Greater Los Angeles region depends on numerous sources of fresh water, both imported and local. Though the majority of Los Angeles' water is imported via the Los Angeles and Colorado River Aqueducts, local water accounted for 11% of the Los Angeles Department of Water and Power's water supply from 2005-2010 (Blanco et al. 2012). In some nearby cities within the Greater Los Angeles region, local water sources contribute an even larger portion. For example, local water supplied about 40% of the overall water demand between 1995 and 2009 in the city of Camarillo (City of Camarillo 2010) and 55% of the water demand in Long Beach for 2010 (Long Beach Water Department 2010).

Cities in Mediterranean-type climates outside of California also rely heavily on local water, including Cape Town, South Africa, which chiefly depends on dams in the mountains of the southwestern Cape for both industrial and domestic water supply (Ziervogel et al. 2010). Adelaide, Australia sources water from neighboring catchments in the Mount Lofty Ranges and approximately half of Adelaide's demand has been supplied from the nearby Myponga, Mount Bold, and Happy Valley reservoirs (Paton et al. 2013). In central Chile, snowpack accumulated in the nearby central Andes represents a critical resource for local irrigation, consumption, industries and hydroelectric generation (Masiokas et al. 2006).

General circulation models (GCMs) provide insight into future climate trends, but their coarse resolution fails to capture climatic variables at a scale necessary for regional-scale analysis (Giorgi and Mearns, 1991). The latest generation of GCMs in the World Climate Research Programme's Coupled Model Intercomparison Project Phase 5 (CMIP5; Taylor et al. 2012) have horizontal resolutions between 1° to 2.5° (~ 100 – 250 km). Los Angeles' complex coastlines and topographical features show variation on much smaller scales and play a dominant role in shaping regional-scale processes, including orographic precipitation, land-sea breezes and valley circulations. Additionally, local topography introduces large spatial gradients in surface and near-surface air temperature, which influence PET. Such regional-scale processes have been shown to be critical in understanding climate variability in California (Cayan, 1996; Conil and Hall, 2006; Hughes et al. 2007). Thus, current GCM resolution is far too low to understand surface hydrology and climate at scales relevant for adaptation and water resources planning.

Dynamical-downscaling has been used to develop high-resolution regional climate data from relatively coarse-resolution GCM output, including in California (Leung et al. 2003; Leung et al. 2004; Kanamitsu and Kanamaru 2007; Caldwell et al. 2009; Qian et al. 2010; Pan et al. 2011; Pierce et al. 2012) and other Mediterranean-type climate regions (Flaounas et al. 2012; Barrera-Escoda et al. 2013; Ratnam et al. 2013). The dynamical downscaling studies over

California, along with a number of regional studies using hydrological models (Dettinger et al. 2004; Vicuna et al. 2007; Young et al. 2009; Huang et al. 2012), have focused primarily on future climate change impacts to hydrology in Central and Northern California, rather than the Los Angeles region.

In this study, dynamical-downscaling simulations are performed to obtain high-resolution (2-km) climate information for the Los Angeles region. These consist of a validated baseline (1981–2000) climate simulation, and downscaling of output from five CMIP5 GCMs under Representative Concentration Pathway 8.5 (RCP8.5) for the mid-21st century period (2041–2060). Idealized temperature sensitivity experiments are also performed, in which the baseline climate simulation is perturbed by uniform air temperature increases of 2°, 4° and 6° C. These experiments reveal the hydrologic sensitivity to warming in the absence of precipitation change. This is a relevant simplification because the projected annual precipitation changes turn out to be quite small in this region (Berg et al. 2015).

This study aims to assess future changes to runoff and AET that result from precipitation and temperature changes in the Los Angeles region; the results from this assessment strongly suggest that other Mediterranean-type climate regions will respond similarly to precipitation and temperature changes. In the process, we will determine the degree to which sensitivity of AET and runoff to warming is indeed suppressed by the unique seasonality of Mediterranean-type climate.

This study is part of a larger project that includes separate downscaling studies of the CMIP5 ensemble's mid-21st century and end-of-21st century projections over the Los Angeles region for temperature (Walton et al. 2015; Sun et al. 2015a), precipitation (Berg et al. 2015), and snowfall and snowpack (Sun et al. 2015b). Together, these studies provide high-resolution information regarding future regional climate trends crucial for developing adaptation strategies.

This paper is organized as follows: Section 2.2 describes the model configuration and observational evaluation for the baseline simulation. Section 2.3 describes the future and idealized climate simulations. Section 2.4 presents the results of both the dynamical-downscaling simulations and the idealized temperature sensitivity experiments. This section is focused on the sensitivity of annual mean AET and runoff to both precipitation and temperature changes, while also placing changes within the context of internal interannual variability. Finally, section 2.5 presents a discussion of the results, as well as a summary of findings.

2.2 Baseline simulation

2.2.1 Dynamical downscaling framework

A dynamical downscaling simulation over the Los Angeles region is performed using the Weather Research and Forecasting Model version 3.2 (WRF; Skamarock et al. 2008). We nest higher resolution domains within one another (18-km, 6-km and 2-km) to reach a high enough resolution to represent the most important features of the region's complex topography and coastlines. Fig. 2.1a shows the three nested domains, as well as the topography at the resolution of the outermost domain. The outermost domain spans the entire state of California and the adjacent Pacific Ocean at 18-km resolution. The middle domain, at 6-km resolution, covers roughly the southern half of the state of California. Finally, the innermost domain, at 2-km resolution, focuses on the Los Angeles region (Fig. 2.1b). In the downscaling simulations, the

Noah Land Surface Model (Chen and Dudhia 2001) is coupled to WRF to simulate land surface processes. For additional information on parameterization options and WRF configuration settings used in the baseline simulation, the reader is directed to Walton et al. (2015).

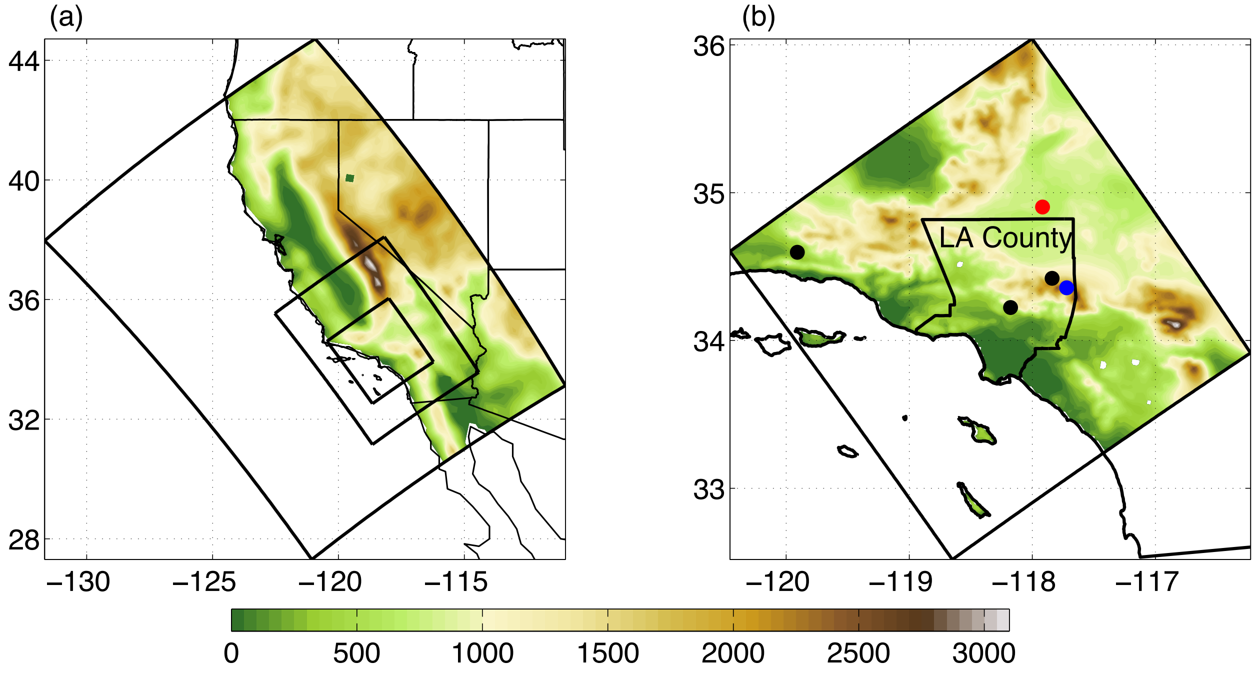

Fig. 2.1: a) Model setup, with three nested WRF domains at resolutions of 18, 6, and 2 km. Topography (m) is shown at the resolution of the 18km domain in color and black lines show boundaries for US states. (b) Topography of the innermost domain (2- km resolution) of the regional simulation, with the border of Los Angeles County in black. In (b), black circles indicate locations of the 3 gauges used for streamflow validation. The blue and red circles in (b) indicate the mountain location and desert location, respectively, referenced in Fig. 2.3 and section 2.2.2.

Using this model configuration, we perform a twenty-year reanalysis-driven “baseline” simulation, which runs from September 1981 to August 2001. The baseline climate simulation is a dynamical downscaling of the National Centers for Environmental Prediction’s North America Regional Reanalysis (NARR; Mesinger et al. 2006). NARR is a coarse-resolution (32-km) reanalysis dataset that provides the lateral boundary conditions for the outermost nested WRF domain seen in Fig. 2.1a. This simulation reconstructs weather and climate and serves two purposes. First, it allows us to evaluate the model's ability to simulate regional climate based on a comparison to observational data. Second, it serves as a climate state against which we can compare future climate simulations to measure climate change.

WRF is reinitialized each year in August, allowing us to run twenty one-year runs from September to August in parallel. This parallelization significantly reduces computational time. However, the annual model re-initialization prevents perfect water budget closure. To ensure the water budget is precisely closed, WRF data from the innermost (2-km) domain of the twenty one-year baseline simulations is used as forcing for a continuous twenty-year simulation using the offline 1-dimensional Noah Land Surface Model version 3.3 (Noah-LSM; Ek et al. 2003). The baseline Noah-LSM simulation is forced by WRF meteorological data, including near-surface air temperature, surface pressure, near-surface wind speed and direction, near-surface relative humidity, precipitation, and downward longwave and shortwave radiative fluxes at the surface. WRF output includes snapshots of 2-dimensional variables every 3 hours and 3-dimensional variables every 6 hours for each grid point.

Potential evapotranspiration in Noah-LSM is calculated using a modified version of the Penman-Monteith equation that accounts for the influence of atmospheric stability on turbulent transport of water vapor (Mahrt and Ek 1984). Surface runoff and infiltration in Noah-LSM are parameterized following Schaake et al. (1996), and actual evapotranspiration is estimated through a Jarvis (1976)-type parameterization similar to Jacquemin and Noilhan (1990). Output from the offline Noah-LSM simulation forced by WRF output (hereinafter called Noah-LSM/WRF) precisely satisfies the surface water balance equation, solving the water budget closure issue presented by model re-initialization. As the focus of our study is terrestrial surface hydrology, we exclude ocean, lake, reservoir and urban grid points in our analysis.

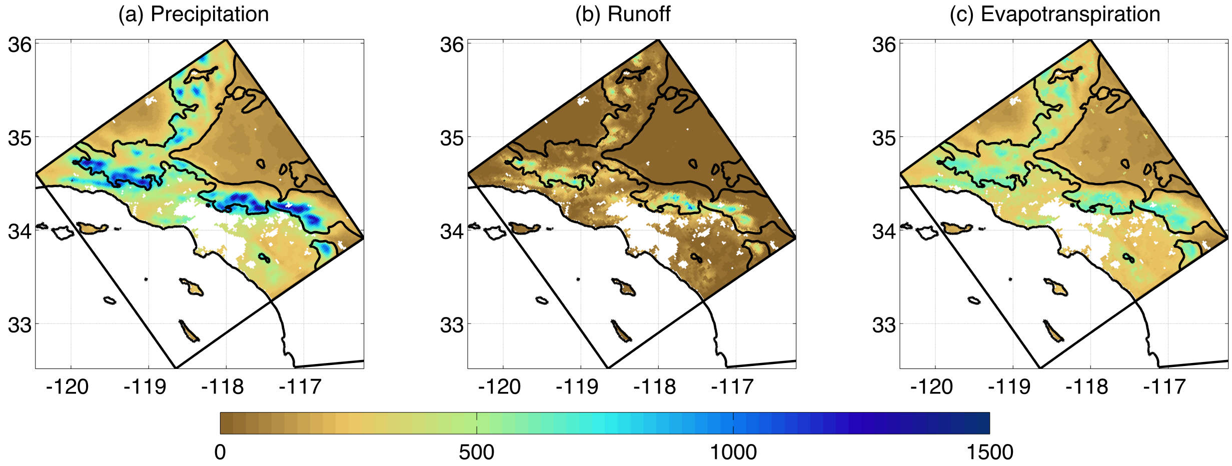

Fig. 2.2: WRF simulation of a) annual accumulated precipitation, and Noah-LSM/WRF simulation of annual b) runoff and c) actual evapotranspiration for the baseline period (September 1981–August 2001). Unit is mm/yr. The 1000m topography contour is highlighted in black. Grid cells with missing values are urban or over water surfaces.

2.2.2 Baseline surface hydroclimate

Fig. 2.2 shows spatial patterns of climatological precipitation, runoff and AET for the baseline period as simulated by Noah-LSM/WRF. The average annual precipitation received at non-urban land points during the baseline period (Fig. 2.2a) is 341 mm/yr, with 91% of the study domain's annual precipitation falling between the months of October and April. The coastal side of mountain areas above 1000m receive nearly 3 times the annual precipitation of low-elevation coastal areas due to orographic precipitation effects. The coastal areas experience greater than 200mm more precipitation than the inland desert region, as moisture is wrung out of air passing over the mountain ranges toward the inland desert.

Figs. 2.2b and 2.2c present the partitioning of precipitation for the baseline Noah-LSM/WRF simulation into runoff and AET, respectively. In this semi-arid domain, 81% of annual precipitation falling on non-urban land surfaces is returned to the atmosphere through

AET, on average. The ratio of runoff to precipitation is highest in coastal areas above 1000m, where runoff accounts for 41% of average incoming annual precipitation.

The annual cycle of the water balance for the 20-year baseline period is shown in Fig. 2.3 for two representative points in our study domain: a high-elevation mountain location (Fig. 2.3a) and an inland desert location (Fig. 2.3b). These two locations are shown in Fig. 2.1b by blue and red circles. The region's climate is characterized by drastic seasonal precipitation variations (especially at the high elevations) and modest seasonal transitions in temperature.

In the case of the mountain location, monthly precipitation (dark blue) is highest in February, and snow water equivalent (pink) peaks in March. Early spring snowmelt then leads to maxima in both soil moisture (brown) and runoff (light blue) in March. Increasing PET (gray) in the late spring and early summer coincides with moist springtime soils (brown), so AET (green) increases in the summer months until the soil moisture is depleted around August. This creates a July peak in AET. The ratio of monthly precipitation to potential evapotranspiration (P/PET) is also presented (Fig. 2.3a, inlay). P/PET is a simple measure of aridity that suggests whether AET should be energy-limited (P>PET) or moisture-limited (P<PET) (Budyko and Miller 1974; Feng and Fu 2013; Scheff and Frierson 2015). At the mountain location, AET is limited by available energy December through March, but water-limited the remaining months (especially July and August, when P/PET is nearly zero). At the desert location (Fig. 2.3b), annual precipitation is low, and AET is roughly equal to precipitation, accounting for over 98% of annual mean precipitation. The ratio of monthly precipitation to potential evapotranspiration at the desert location (Fig. 2.3b, inlay) suggests AET is strongly water-limited throughout the year. The out-of-phase relationship in the annual cycles of precipitation and PET sets up a unique response to temperature changes that will be explored later in this paper.

(a) Mountain Location

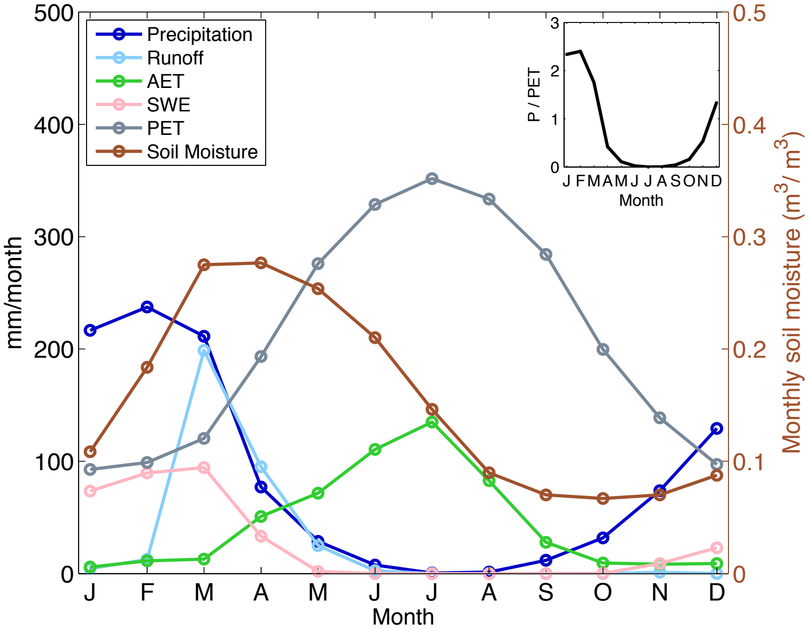

(b) Desert Location

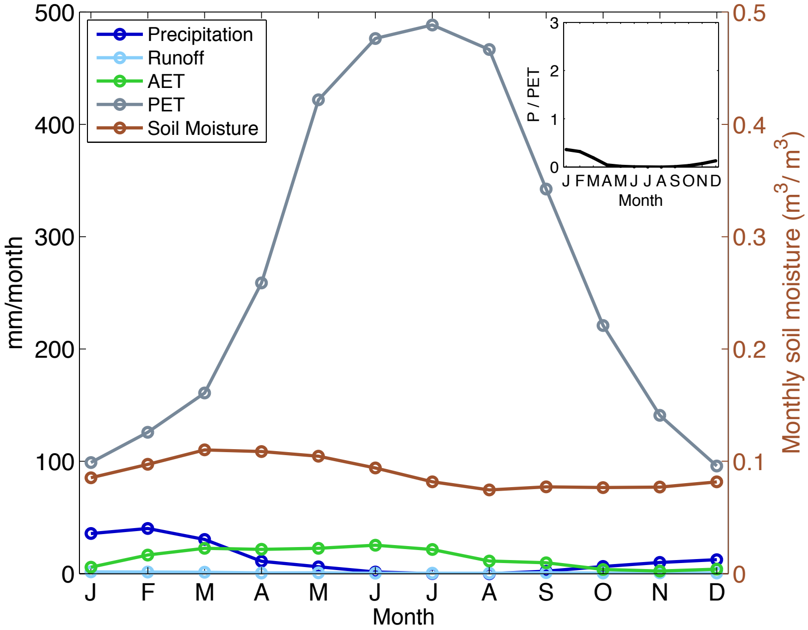

Fig. 2.3: Noah-LSM/WRF simulation of the baseline mean annual cycle of the water balance at a point representative of (a) mountain locations and (b) the inland desert. Monthly accumulated values (unit: mm/month) of precipitation (dark blue), runoff (light blue), actual evapotranspiration (green) and potential evapotranspiration (gray) are shown with respect to the left y-axis. The climatological monthly soil moisture (unit: m^3/m^3) of the top 2m of the soil column is also shown (brown) with respect to the right y-axis. Inlays show baseline mean monthly ratio of precipitation to potential evapotranspiration. For the mountain location (a), mean monthly snow water equivalent is presented (pink).

2.2.3 Model evaluation

Prior to analyzing surface hydrology changes, we evaluate the skill of the 2-km resolution baseline (1981-2000) simulation by comparing Noah-LSM/WRF model output to available observations.

We first briefly recapitulate an evaluation of WRF's precipitation by Berg et al. (2015). This downscaling study of precipitation changes over the Los Angeles region uses the same baseline dynamical downscaling framework as this study. Berg et al. (2015) demonstrate that this modeling framework realistically simulates wet-season (December–March, DJFM) precipitation in the study domain using precipitation gauges from the California Department of Water Resources' California Irrigation Management Information System (CIMIS, http://www.cimis.water.ca.gov/), and two gridded observational products, NOAA Climate Prediction Center Daily US UNIFIED Precipitation (CPC, http://www.esrl.noaa.gov/psd/data/-gridded/data.unified.html) and the University of Delaware Precipitation product (Udel, http://www.esrl.noaa.gov/psd/data/gridded/data.UDel_AirT_Precip.html). They find a high domain-average correlation coefficient (r =0.82) between mean DJFM precipitation observed at CPC grid cells and that simulated at the nearest corresponding WRF grid cell. Moreover, they find that WRF successfully reproduces the CIMIS station-averaged DJFM total precipitation over the 12 wet seasons from 1989–2000 (note: CIMIS observations start in 1989), with an average bias of +15 mm per year. This bias is not systematic and is quite small in relative terms. (CIMIS station-averaged DJFM total precipitation ranges from approximately 120 to 550 mm/year over 1989–2000.) Overall, they find that WRF simulates monthly precipitation variations at thirteen CIMIS gauges in the study domain reasonably well, and that the WRF framework realistically simulates interannual variability in wet-season precipitation.

Next, we evaluate Noah-LSM/WRF's simulation of streamflow, relying on the United States Geological Survey Hydro-Climatic Data Network-2009 (USGS HCDN-2009, http://waterdata/usgs.gov/nwis/) observational dataset. The USGS HCDN-2009 is a network of streamflow gauges across the United States identified as having: (1) natural streamflow least affected by direct human activities, (2) accurate measurement records, and (3) at least 20 years of complete and continuous discharge record through water year 2009 (Slack et al. 1993; Lins 2012).

We obtained daily, quality-controlled streamflow data from 3 stations for which data was available within our study domain for the baseline period. The locations of these streamflow gauges are shown in Fig. 2.1b by black circles. There is no runoff routing scheme in the Noah-LSM/WRF framework. To account for this, we compare the observed streamflow measurement at a USGS gauge to the sum of simulated surface runoff from all grid points within a watershed upstream of the gauge. This rather primitive form of runoff routing does not account for groundwater dynamics or interactions between groundwater and surface runoff.

Fig. 2.4a compares monthly climatological average streamflow for USGS gauges (solid lines) with that simulated by Noah-LSM/WRF (dashed lines). Noah-LSM/WRF's simulation of the annual streamflow cycle is consistent with observations for each of the three gauges, with a correlation averaged across the gauges of r = 0.88. Noah-LSM/WRF correctly simulates the magnitude and phasing of heightened streamflows in the months of February through May (late in the wet season), with relatively low flows the rest of the year. The root mean squared error of all data points in Fig. 2.4a is 0.28 cubic meters per second. These minor differences may be due to observational error or a lack of groundwater dynamics in Noah-LSM/WRF.

(a) Monthly Streamflow Climatology, Observed and Simulated

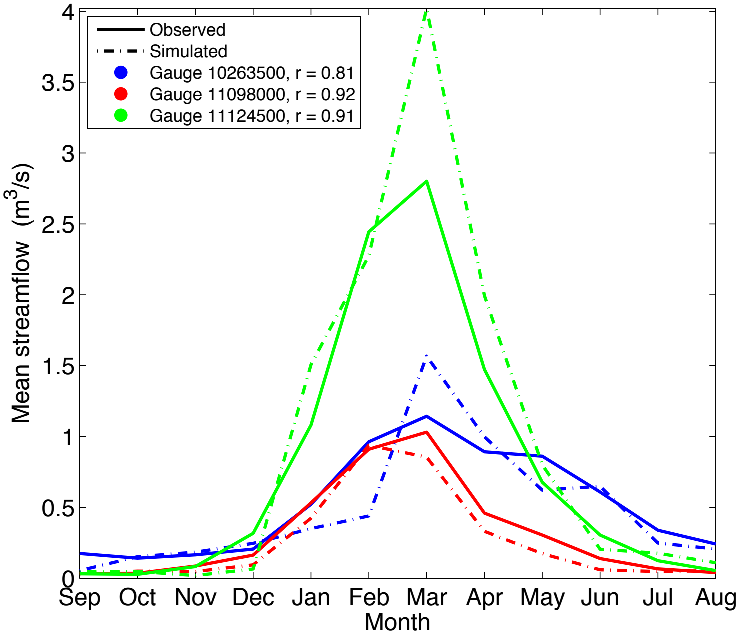

(b) Annual Average Streamflow, Observed vs. Simulated

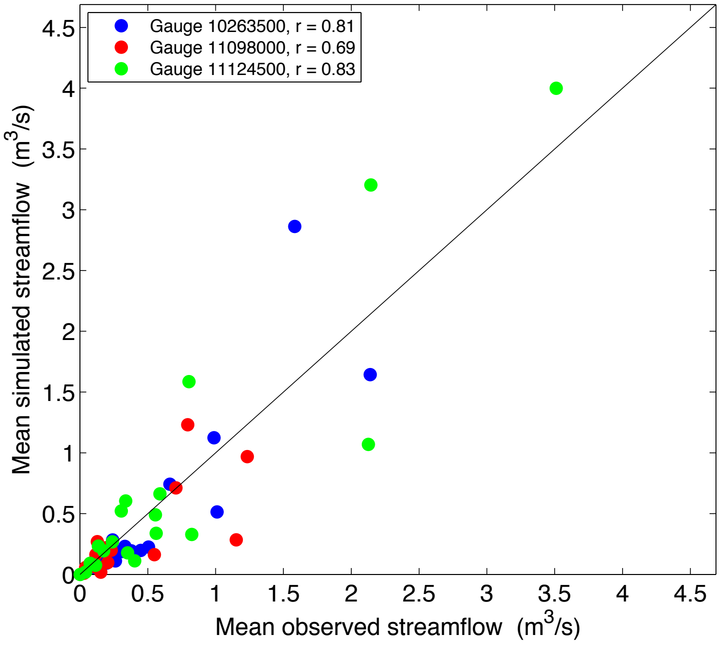

Fig. 2.4: Evaluation of Noah-LSM/WRF dynamical downscaling of runoff during the baseline period for three streamflow gauges. a) Observed (solid) and simulated (dashed) monthly mean streamflow over the water year (September to August). b) Observed vs. simulated annual mean streamflow, with the line y = x shown in black. Observed streamflow data is compared to simulated surface runoff aggregated upstream of the gauge within a watershed. Correlation coefficients for each gauge are also presented.

Fig. 2.4b compares the annual average streamflow between each USGS gauge and the Noah-LSM/WRF simulation of runoff within the watershed for all twenty water years (September – August) of the baseline period. Correlations above r = 0.69 are found at all gauges, and the gauge-average correlation is r = 0.77. Again, the points fall approximately on the one-to-one line. Overall, Figs. 2.4a and 2.4b demonstrate Noah-LSM/WRF reproduces the spatial, seasonal and interannual variations in surface runoff reasonably well.

Unfortunately, observational data networks, including FLUXNET (Balhocchi et al. 2001) and CIMIS stations, do not provide observations of AET (e.g. through measurement methods such as eddy covariance techniques, a scintillometer or lysimeter) in the study domain during the baseline period. This prevents us from comparing simulated AET to observations directly. However, assuming no mean change in terrestrial water storage on annual time scales, annual mean AET must equal annual mean precipitation minus mean runoff. Because of the skill of Noah-LSM/WRF in realistically simulating interannual variability in both precipitation (Berg et al. 2015) and runoff (Fig. 2.4b), we can infer the model probably also realistically simulates the interannual variability in AET.

Overall, Fig. 2.4 and Berg et al. (2015) show that the Noah-LSM/WRF framework simulates the temporal and spatial variations of surface hydrology during the baseline period with reasonable accuracy where reliable observational data are available. Previous research also demonstrates that the WRF framework used in this study provides realistic simulations of both spatial and temporal patterns of temperature (Walton et al. 2015) and snowfall (Sun et al. 2015b). Based on this evidence, it seems likely that the model is able to realistically reproduce the temporal and spatial variations in AET and runoff across the domain, at locations where observations are not available.

2.3 Future simulation

Using the same WRF configuration as the baseline climate simulation, we perform a second group of climate simulations designed to simulate a range of future regional climate states corresponding to the mid-21st century. By looking at differences between the future and baseline periods, mid-century changes to surface hydrology relative to the late 20th century can be quantified and evaluated. To produce boundary conditions for future simulations, we employ a previously used method (Schar et al. 1996; Hara et al. 2008; Kawase et al. 2009; Rasmussen et al. 2011), in which future climate is estimated by adding a perturbation reflective of the mean climate change to reanalysis data. We apply this technique to output from five CMIP5 global climate models (CCSM4, CNRM-CM5, GFDL-CM3, MIROC-ESM-CHEM and MPI-ESM-LR) under the RCP8.5 emissions scenario for the mid-21st century period. More specifically, we perturb the NARR baseline boundary conditions (September 1981 - August 2001) by monthly-averaged differences between the future and baseline (2041-2060 minus 1981-2000) climate for each GCM. This perturbation method assumes no change in synoptic and interannual variability at the lateral boundaries. As a result, the frequency of future weather events is very similar to that of the baseline simulation (though we cannot exclude the possibility that regional climate dynamics might alter local weather events). Thus our analysis focuses on time scales of months to years.

Because it would be prohibitively expensive to perform full twenty-year future dynamical-downscaling simulations for each of the five GCMs, we first perform a future twenty-year simulation (September 2041 to August 2061) using climate change signals in CCSM4. Then we examine this experiment to assess whether short simulations can provide statistics robust enough to characterize the regional climate change signal of the full twenty-year simulation.

Similar to the baseline simulation, this future simulation is reinitialized every August and run in parallel as twenty one-year simulations. Using Noah-LSM, we also perform a separate continuous twenty-year simulation of the dynamically downscaled output associated with CCSM4.

We find that we are able to capture to a high degree of accuracy the full 20-year runoff and AET signals by simulating only three future years of CCSM4. (We select the three water-year period of September 2058 to August 2061, as its corresponding baseline period, September 1998 to August 2001, is roughly representative of interannual variations in precipitation and temperature during the full 20-year baseline period. Other consecutive three-year periods are also likely to be representative of the full 20-year baseline period.) For example, averaged over non-urban land points, the 20-year and 3-year runoff signals associated with CCSM4 are -17.6 and -16.3 mm/yr, respectively. Previous analyses of this output found that the 20-year precipitation and temperature signals could also be captured with a high degree of precision by only dynamically-downscaling three future years (Berg et al. 2015; Walton et al. 2015). Thus, to conserve computational resources, we only dynamically downscale the remaining four GCMs (CNRM-CM5, GFDL-CM3, MIROC-ESM-CHEM and MPI-ESM-LR) for three years. For each of these four future simulations, WRF boundary conditions are created by adding the 20-year GCM climate change signal (2041–2060 minus 1981–2000) to NARR data corresponding to September 1998 to August 2001. Though the future simulations of CNRM-CM5, GFDL-CM3, MIROC-ESM-CHEM and MPI-ESM-LR are only three years long, the climate change forcings therefore reflect that of a 20-year averaging period.

Similar to the twenty-year baseline and twenty-year CCSM4 simulations, the three-year mid-21st century simulations associated with CNRM-CM5, GFDL-CM3, MIROC-ESM-CHEM and MPI-ESM-LR are run as three one-year simulations re-initialized every August. The WRF output is then used to force a continuous three-year future climate simulation using Noah-LSM.

Given projections for little to no ensemble-mean precipitation change in our study domain (discussed in section 2.4.1 and Berg et al. 2015), it is useful and relevant to study the hydrologic response to warming in isolation from precipitation changes. Thus, we perform three idealized twenty-year simulations with Noah-LSM designed to isolate the imprint of warming on runoff and AET. The idealized simulations are identical to the twenty-year Noah-LSM baseline (1981-2000) simulation forced by WRF data, except with a spatially uniform 2-meter air temperature increase of 2 °C, 4 °C and 6 °C at every time step. All other climatic variables are unchanged from baseline values. It should be noted that because relative humidity is unchanged from baseline values, specific humidity is implicitly allowed to increase with near-surface warming.

The idealized simulations allow us to examine the sensitivity of surface hydrology in the Los Angeles region to a range of likely temperature changes (Walton et al. 2015). Increases in near-surface air temperature can affect runoff characteristics by altering the form of precipitation, AET rate and snowmelt timing. We label the results from the idealized simulations as baseline, T2, T4 and T6.

2.4 Results

In this section, we present results from both Noah-LSM/WRF dynamical-downscaling of GCM output and the idealized simulations.

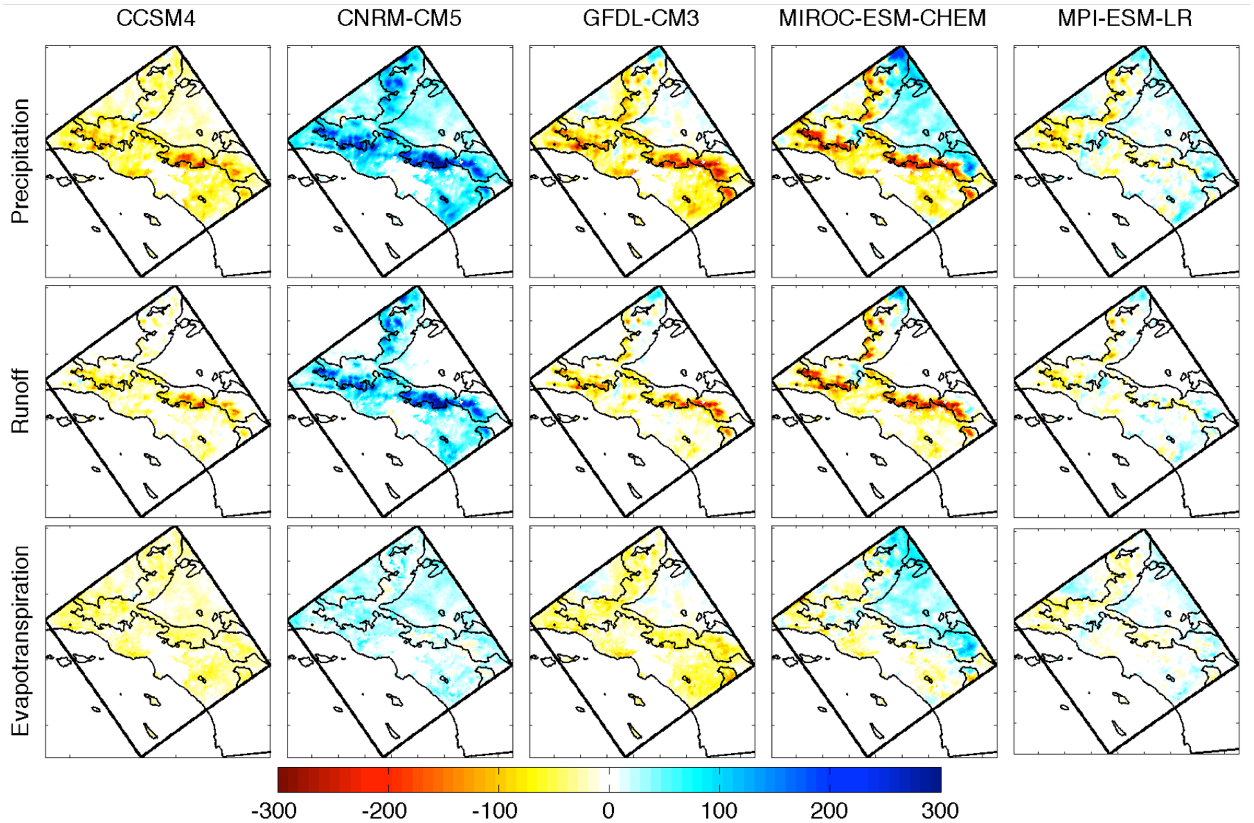

Fig. 2.5: Noah-LSM/WRF simulation of the mid-21st century change (mm/yr) in precipitation (row 1), runoff (row 2) and actual evapotranspiration (row 3) relative to the baseline period for five GCMs under RCP8.5: CCSM4, CNRM-CM3, GFDL-CM3, MIROC-ESM-CHEM and MPI-ESM-LR. Blue shading indicates moistening, while yellow/red shading indicates drying. The 1000m topography contour is highlighted.

2.4.1 Small precipitation changes

Fig. 2.5 (first row) shows annual mean precipitation changes for five GCMs as simulated by WRF. The precipitation projections show some intermodel spread, particularly with regard to the sign of the change. The ensemble-mean precipitation change for non-urban land surfaces across the five GCMs is -6.6 mm/yr, a minute change reflective of a cancellation between moistening (CNRM-CM5 and MPI-ESM-LR) and drying (CCSM4, GFDL-CM3 and MIROC-ESM-CHEM) models. CNRM-CM5 and GFDL-CM3 project the largest precipitation changes, with changes of +51 and –39 mm/yr averaged over non-urban land surfaces, respectively.

These signals in precipitation changes are modest compared to the region's interannual variability. The standard deviation of baseline (1981-2000) precipitation averaged over non-urban land surfaces as simulated by WRF is 153 mm/yr, roughly 40% of the climatological mean and reflective of the region's significant interannual hydroclimate variability. Thus the downscaled change in average precipitation over non-urban land surfaces as projected by even the most extreme model (CNRM-CM5) is only about a third of the baseline interannual variability. Berg et al. (2015) further explore the region's precipitation changes, and conclude that the most likely result is a small change in mean precipitation compared to natural variability, with the sign of the change being uncertain. Berg et al. (2015) also extend the analysis to include the full CMIP5 GCM ensemble through statistical techniques. However, their results are very similar to those obtained from dynamically downscaling only these five GCMs.

2.4.2 Runoff, AET and PET changes

Annual mean runoff changes for the five GCMs are shown in Fig. 2.5 (second row). For each GCM, the runoff change mirrors the precipitation change in both sign and magnitude. Fig. 2.6 corroborates this. The spatial patterns of precipitation change and runoff change are tightly correlated for all models, with a model-average spatial correlation coefficient of $r = 0.88$. For all five future simulations, the sign of the change in annual runoff is the same as the sign of the change in annual precipitation for over 98% of non-urban land grid points in the study domain. Discrepancies are greatest over the desert, where a positive precipitation change may lead to a slightly negative runoff change due to enhanced AET (e.g. MIROC-ESM-CHEM). Overall, any precipitation change appears to control the runoff change. Because the precipitation changes are modest, so are the runoff change signals. For CNRM-CM5, the model with the strongest moistening, the average runoff signal over non-urban land surfaces is 34 mm/yr. The average runoff signal over non-urban land surfaces for the driest model, GFDL-CM3, is -21 mm/yr. Both values are small compared to the standard deviation of runoff in the baseline period (103 mm/yr).

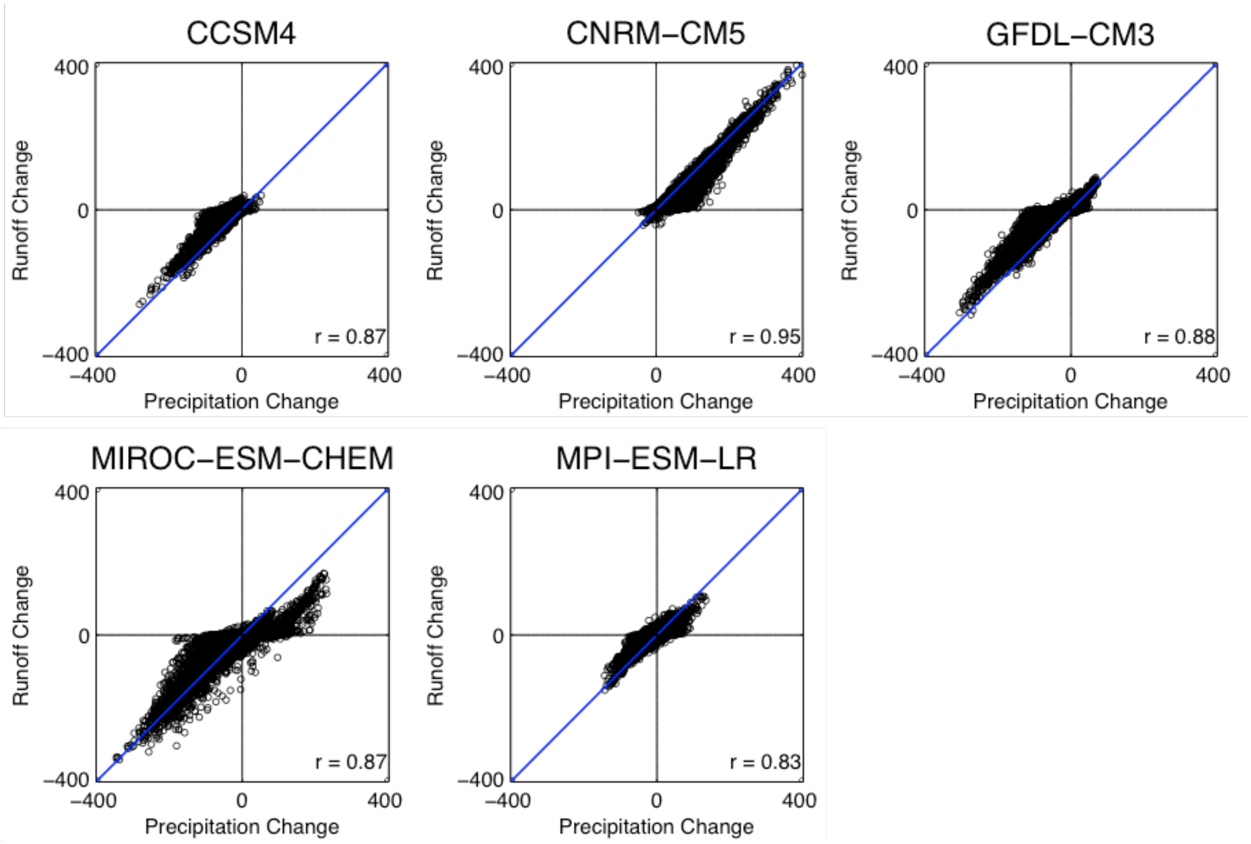

Fig. 2.6: Scatter plot of mid-21st century change in annual precipitation (mm/yr) vs. annual runoff (mm/yr) at all non-urban land surface in the study domain when five GCMs under RCP8.5 are downscaled: CCSM4, CNRM-CM3, GFDL-CM3, MIROC-ESM-CHEM and MPI-ESM-LR. Correlation coefficients are shown in the bottom corner for each plot. The line y = x is shown in blue.

We now turn to changes in PET and AET. As expected from the relationship between temperature and saturation vapor pressure, each future simulation projects a domain-wide increase in PET for all non-urban land surfaces (not shown), with an ensemble-mean change of 186 mm/yr averaged over non-urban land areas. PET increases are highest above 1000m, where decreases in future snow cover and albedo during winter lead to increased absorption of downward radiation, providing more energy for PET. Annual mean AET changes are shown in Fig. 2.5 (third row). Despite domain-wide PET increases, AET rates are severely limited by surface water availability. In fact, for the 5 dynamically downscaled GCMs, the sign of model's precipitation change is the main determinant of the model's AET change. The partitioning of the precipitation change into a runoff change or AET change is largely determined by baseline partitioning of precipitation into runoff and AET (Fig. 2.2). However, the relationship between the precipitation change and AET change is not as strong as the relationship between the precipitation change and runoff change (model-average spatial correlation coefficient of r = 0.61 vs. r = 0.88).

2.4.3 Idealized simulations: Limited influence of warming on AET

It is noteworthy that the annual mean change in AET for each of the five dynamically-downscaled GCMs is small and precipitation-determined, even though there is significant near-surface warming. One would expect warmer surface air temperatures and increased downward longwave radiation to enhance AET throughout the domain at least somewhat. We turn to the idealized simulations to quantify the sensitivity of runoff and AET to warming in the absence of a precipitation change. By looking at differences between the idealized simulations and the baseline (1981-2000) simulation, we examine the direct influence of changing temperatures on annual mean AET and runoff.

Fig. 2.7 shows the change in annual 2-meter air temperature (first row) and annual AET (second row) for each of the idealized simulations: T2, T4 and T6. Due to a nearly negligible change in infiltration, the surface water balance equation constrains the annual mean runoff change for each simulation to be almost identical in magnitude to the annual mean AET change, with an opposite sign.

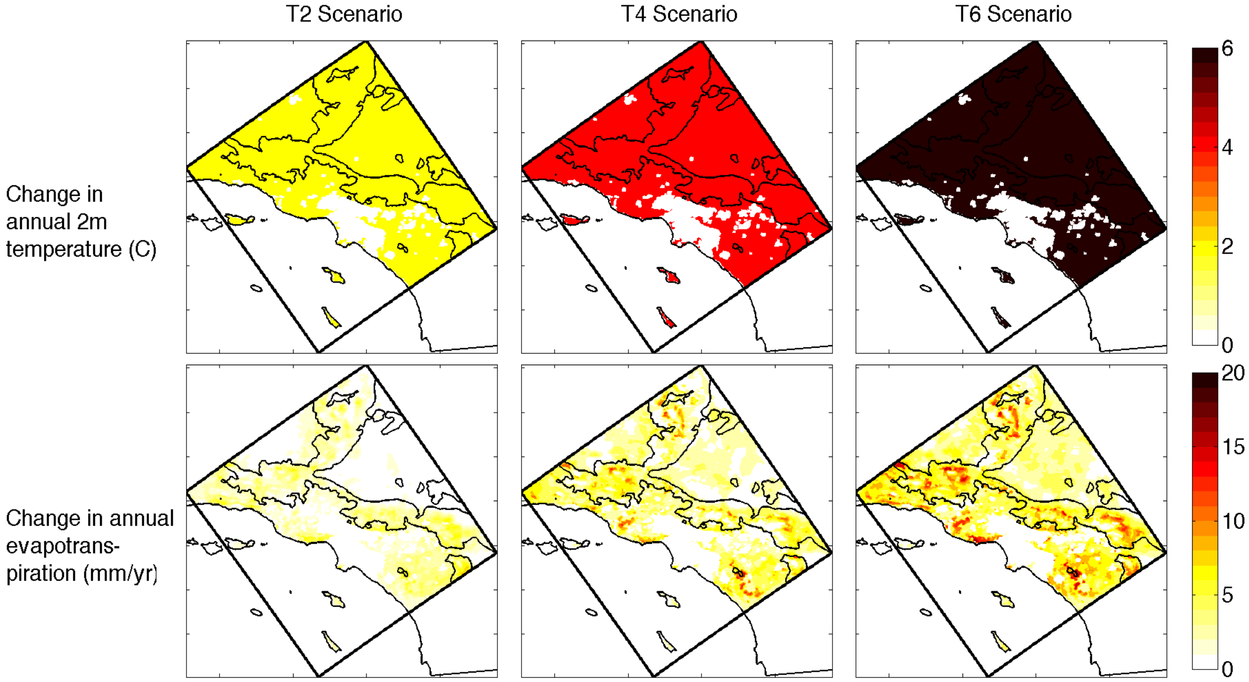

Fig. 2.7: Results from three idealized simulations in which Noah-LSM/WRF dynamically-downscaled output for the baseline (1981-2000) period is perturbed by a uniform increase in near-surface air temperature of 2° C (left column, T2 scenario), 4° C (center column, T4 scenario), and 6° C (right column, T6 scenario). Changes in annual near-surface air temperature (first row, unit: °C) and actual evapotranspiration (second row, unit: mm/yr) are shown for each idealized scenario. Precipitation is not perturbed. The 1000m topography contour is shown.

For even the most extreme warming case (T6), the domain-average AET change over non-urban land surfaces (7.56 mm/yr) pales in comparison to both the baseline mean (276 mm/yr) and interannual variability (56 mm/yr). Runoff changes are similarly small. From the baseline simulation to T6 scenario, the absolute increase in the ratio of domain-average evaporation to precipitation (E/P) is 2%, a tiny amount. The AET changes (second row) appear to have some spatial structure, in that the strongest AET increases are at high elevations (see topography in Fig. 2.1b) as well as at locations with high AET in the baseline (Fig. 2.2c).

However, even for a mountain location where the AET signal is stronger (like the location referenced in Fig. 2.3a), annual AET in the T6 scenario increases by 11 mm/yr, a mere 2% relative increase. Without a precipitation change, surface air temperatures would have to increase significantly more than 6º C to have a substantial impact on annual AET and runoff.

(a) Annual PET cycle for baseline and idealized scenarios

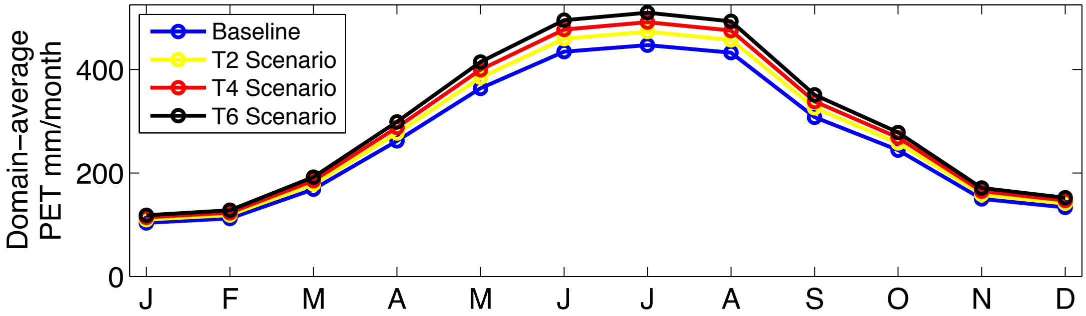

(b) Annual AET cycle for baseline and idealized scenarios

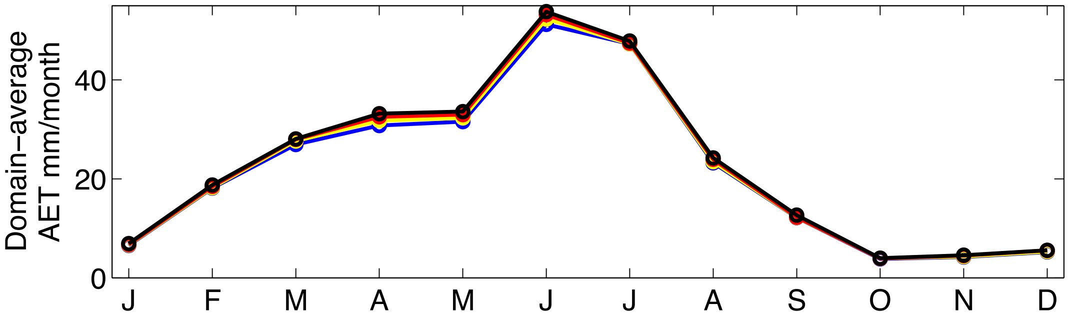

(c) Annual runoff cycle for baseline and idealized scenarios

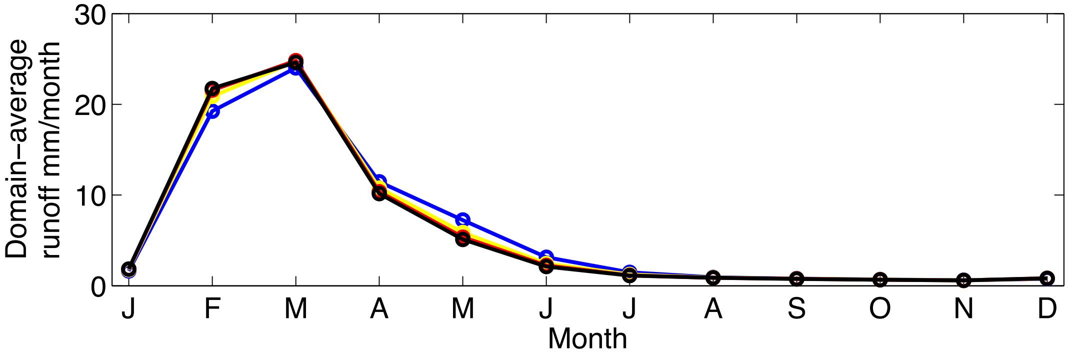

Fig. 2.8: Noah-LSM simulation of the domain-average annual cycle of (a) potential evapotranspiration, (b) actual evapotranspiration and (c) runoff over non-urban land surfaces for the baseline (1981-2000) simulation (blue) and three idealized simulations in which the baseline simulation is perturbed by a uniform increase in near-surface air temperature of 2° C (yellow, T2 scenario), 4° C (red, T4 scenario), and 6° C (black, T6 scenario). Unit: mm/month.

The insensitivity of surface hydrology to warming is explored further in Fig. 2.8, which shows the average annual cycles of (a) PET, (b) AET and (c) runoff over non-urban land surfaces for the baseline (1981-2000) simulation (blue), T2 (yellow), T4 (red) and T6 (black). PET (Fig. 2.8a) increases significantly in all idealized simulations following the monthly temperature distribution. Domain-average annual PET increases by 5%, 10% and 15% for T2, T4 and T6, respectively.

In contrast, annual mean AET (Fig. 2.8b) and runoff (Fig. 2.8c) remain largely unchanged in all three idealized cases. We argue this is an artifact of Southern California's Mediterranean climate (discussed in section 2.1), in which the annual cycles of precipitation and soil moisture are out of phase with that of PET (Fig. 2.3). For each idealized warming scenario, AET increases slightly in all months, but the effect is largest from April to June, and diminished in the cool season (December to March). In the case of T2, T4 and T6, PET increases are strongest during the months of April to October (Fig. 2.8a), yet soil moisture is relatively low from July to January (in both the baseline and idealized simulations) due to the seasonality of precipitation (Fig. 2.3). In the idealized scenarios, only the months of April through June have both enhanced PET and moist enough soils to allow for an AET increase; the remaining months of July through March have either too limited soil moisture or relatively low PET, which prevents increased PET from having a significant effect on AET.

For the most extreme warming scenario (T6), the overlap of enhanced PET and soil moisture availability in April, May, and June leads to monthly AET increases of 7.8%, 6.5% and 5%, respectively (Fig. 2.8b). By July and August, AET is severely moisture-limited (based on monthly ratios of P/PET), more so than all other months (Fig 2.3); this suggests that even under future warming, July-August soil moisture is depleted to the extent that it limits an AET increase.

The April to June AET change also accelerates the soil moisture decrease that occurs in the baseline simulation from May to July. This exhausts nearly the same amount of soil moisture as in the baseline, but earlier in the season, so that future July AET becomes even more moisture-limited than in the baseline. Given that nearly all annual runoff has occurred by May, increases in AET in May and June do almost nothing to reduce annual mean runoff (Fig. 2.8c).

The particularly small cool-season AET increase can largely be explained by baseline annual mean cycles of soil moisture and PET (Fig. 2.3). Baseline soil moisture is very low in December and January (Fig. 2.3), consistent with a moisture-limitation on AET. However, March AET remains small even though soils are very wet. This is likely due to cool temperatures and low PET. At the mountain location (Fig. 2.3a), for example, monthly P/PET indicates that AET is in fact energy-limited in December- March due to cool temperatures. In the idealized warming scenarios, despite warming-driven PET increases in the cool-season, ratios of monthly P/PET still indicate AET is energy-limited from December through March.

In summary, AET increases are slight in all months for each idealized warming scenario, although they are noticeable from April-June. Domain-average annual AET increases also pale in comparison to both baseline mean AET and its interannual variability. Thus annual mean runoff and AET are largely insensitive to warming. One could imagine a very different situation if the study domain received significant summer rainfall, which would cause elevated soil moisture values at the same time as the peak in the annual PET cycle. In this case, warming could lead to enhanced AET and decreased annual mean runoff.

This insensitivity of annual mean runoff and AET to future temperature changes in Southern California is consistent with other studies over Northern California. Risbey and Entekhabi (1996) found annual mean streamflow in the Sacramento River to be nearly insensitive to temperature changes, but very sensitive to precipitation changes. Dettinger et al. (2004) found similar results in the Merced, Carson and American river basins of California. Together, the dynamically-downscaled GCMs and idealized simulations suggest both annual mean runoff and AET in the Los Angeles region are almost insensitive to warming, but highly sensitive to changes in annual mean precipitation.

Lastly, Fig. 2.8c allows us to assess possible warming-driven advances in the timing of seasonal runoff due to shifts toward more liquid precipitation and earlier snowmelt. In each idealized warming scenario, domain-average runoff increases in both February and March, which is compensated by decreased runoff in April and May. Under T6, domain-average February runoff increases by 12%, while April runoff decreases by 11%. Changes to runoff volume are negligible during the months when baseline runoff is small (July though January). Despite these changes, the annual runoff cycle under T6 is generally the same as that of the baseline, with heightened runoff in February through May and same peak flow in March.

To quantify the advance in runoff timing, we consider the date in the water year by which 50% of the cumulative water year runoff has occurred. This is often called the center of runoff volume and widely used within climate science as a metric of snowmelt timing (Stewart et al. 2004, Stewart et al. 2005, McCabe and Clark 2005). For the most extreme warming scenario (T6), the domain-average center of runoff volume advances by a mere 5 days, a rather small change given 6 °C warming . This suggests that warming-driven advances in runoff timing in this relatively warm region are not significant, likely due to a predominance of liquid rather than frozen precipitation.

2.5 Summary, discussion and conclusions

Although it has been well documented that climate change is likely to have profound impacts on the hydrology of the Western United States, few studies have examined the sensitivity of surface hydrology in the Los Angeles region to climate change. Without such analysis, the scientific foundation for informed adaptation strategies at the local and regional scale is missing. This study aims to close this knowledge gap by exploring sensitivities of both annual runoff and AET to regional precipitation and temperature changes.

This study uses dynamical-downscaling techniques to examine mid-21st century changes to surface hydrology over the Los Angeles region under RCP8.5 for five CMIP5 GCMs: CCSM4, CNRM-CM5, GFDL-CM3, MIROC-ESM-CHEM and MPI-ESM-LR. Any change in annual precipitation is mirrored by a similar, though weaker, change in runoff. However, the average annual precipitation change over non-urban land surfaces for each GCM is small compared to their range of baseline interannual variability. Despite warming projected by dynamically-downscaled GCMs in this study, annual mean runoff and AET signals are also found to be well within their range of baseline interannual variability.

Given the small precipitation change, this study includes a series of temperature sensitivity experiments to shed light on the hydrologic insensitivity to warming. Three idealized simulations are performed in which the baseline climate is perturbed by uniform near-surface air temperature increases of 2°, 4° and 6° C. Significant increases in annual mean PET occur with increasing temperatures, with strongest increases in the warm months. Despite significantly enhanced April to October PET in the idealized warming scenarios, available soil moisture confines AET increases to the months of April through June. Small springtime AET increases accelerate soil moisture drying, but exhaust nearly the same amount of moisture, leading to miniscule changes in annual mean runoff and AET for all idealized scenarios. This is an artifact of the out-of-phase relationship between the annual precipitation and soil moisture cycles and annual PET cycle in Mediterranean-type climate zones like the Los Angeles region.

The finding that annual mean runoff is nearly insensitive to temperature increases in the Los Angeles region may have implications for other Mediterranean climate regions. Surface hydrology in other Mediterranean climate zones, including most lands around the Mediterranean Sea, Western and Southern Australia, and Chile, is similar to that of the Los Angeles region, and would likely respond in a similar manner to warming. Previous studies of warming impacts to surface hydrology in Mediterranean-type climates outside California have indeed shown similar results. Chiew et al. (1995) applied a range of plausible temperature and precipitation changes to a rainfall-runoff model to study the sensitivity of runoff and soil moisture in Australian catchments to potential changes in climate. They found that compared to precipitation, temperature increases alone have negligible impacts on runoff and soil moisture. New (2002) examined the sensitivity of runoff in four mountainous catchments in the southwestern Cape of South Africa to a range of possible future climate changes, and found that streamflow in all catchments is more responsive to precipitation changes than PET changes.

This study demonstrates that the insensitivity of annual mean runoff to warming in the Los Angeles region is an artifact of the region's Mediterranean climate, but weak changes in runoff magnitude associated with climate change may not be unique to the Los Angeles region. Previous studies of future runoff changes at the global-scale find that robust changes are generally positive or weakly negative, but not strongly negative. In an analysis of coarse-resolution CMIP5 ensemble-mean projections for annual mean runoff at end-of-21st-century under RCP8.5 compared to end-of-20th-century, Collins et al. (2013) found runoff changes are not strongly negative in most regions, including in California, where the ensemble-mean projected runoff change is within one standard deviation of internal variability (Collins et al. 2013). Similarly, in an analysis of output from 14 coupled CMIP5 GCMs under a low-moderate emissions scenario (RCP4.5), Zhao and Dai (2015) found that robust projected end-of-21st-century changes in runoff are generally positive, despite PET increases. Zhao and Dai (2015) also found that runoff change patterns are primarily controlled by precipitation changes. Although it is difficult to extrapolate from such general global-scale conclusions to individual regions, these findings are not inconsistent with ours.

One potential limitation of this study is that the modeling framework does not take into consideration the physiological effects of increased atmospheric carbon dioxide concentrations on plant stomatal resistance (i.e. CO_2 fertilization). Increases in atmospheric carbon dioxide concentrations enhance the leaf's internal carbon dioxide absorption rate. This gives plants the flexibility to increase their stomatal resistance to conserve water. CO_2 fertilization generally results in a decrease of canopy transpiration and therefore affects the water balance (Betts et al. 2007). In our simulations, the CO_2 fertilization effect would reduce AET sensitivity to temperature increases still further by reducing AET. Therefore, if this study had included CO_2 fertilization effects, the result that annual mean AET and runoff are nearly insensitive to temperature increases would hardly change.

As the focus of this study is future changes to mean surface runoff in the Los Angeles region, it has relevance to future changes to local water supply. Small changes to annual mean surface runoff suggest that a regional climate change adaptation strategy involving greater reliance on local water resources is feasible. However, we did not examine the water demand component of water resource management. In our dynamically-downscaled GCM simulations, 2-meter relative humidity is projected to decrease by mid-21st-century (not shown). This, coupled with large temperature increases and population increases, could greatly increase water demand for crops and lawns. Unfortunately, our modeling framework does not take into account water management practices, including irrigation. This prevents development of a comprehensive set of recommendations regarding future water management, and highlights the need for future regional climate modeling that considers climate, hydrology, and water resource management.

This study diagnoses the sensitivity of the Los Angeles region's surface hydrology to both precipitation and temperature changes. Together, the dynamically-downscaled GCMs and idealized simulations suggest both annual mean runoff and actual evapotranspiration in the Los Angeles region are almost insensitive to warming, but are instead controlled by possible changes in annual mean precipitation. Surface hydrology in other Mediterranean climate regions will likely behave similarly. This result greatly mitigates a potential vulnerability of water resources to a changing climate in an important semi-arid region of the world. It also reveals that a regional climate change adaptation strategy relying on local water resources is a viable one.

3 Significant and inevitable end-of-21st-century advances in surface runoff timing in California's Sierra Nevada

3.1 Introduction

Over half of California's developed water comes from small streams in the ecologically-sensitive Sierra Nevada (USDA Forest Service 2009). Understanding future changes to streamflow in this region is therefore critical to ensuring enough freshwater resources for municipal, economic, and ecological purposes in the coming decades. Recent warming has already produced detectable changes in the timing, magnitude, and variability of Sierra Nevada streamflow (Aguado et al. 1992, Dettinger and Cayan 1995, Cayan et al. 2001, Regonda et al. 2005, Stewart et al. 2005, McCabe et al. 2005, Maurer et al. 2007, Hidalgo et al. 2009, Kim and Jain 2011). In an observation-based study, Stewart et al. (2005) found that from 1948 to 2000, a majority of rivers in the Sierra Nevada exhibited earlier timing during the snowmelt season of roughly 10-30 days. McCabe et al. (2005) found a similar result for 84 streamflow gauges in the Western U.S., with increased April through July temperatures largely accounting for the advancement of runoff timing at most sites. Moreover, Cayan et al. (2001) found that the first major pulse of snowmelt at high-elevation stream gauges in the Western U.S. advanced by about 10 days between 1948 and 1995.

While observed shifts in Sierra Nevada runoff timing have been well documented, few studies have produced quantitative estimates of its future changes and the associated uncertainty. First, runoff timing in this region is influenced by a complex interplay of climatic and geographic factors that are poorly resolved in coarse-resolution global climate models (GCMs). GCM simulations lack important spatial structure in local climatic factors, such as temperature and snowpack, which exert dominant controls on runoff timing and its spatial distribution. Additionally, GCM resolution is too low to adequately represent physical watershed characteristics (e.g. elevation, slope, and vegetation type and coverage) that can also profoundly influence runoff timing and its spatial distribution.

These limitations have motivated efforts to regionalize GCM climate change signals through a variety of downscaling methods (Giorgi et al. 1994, Snyder et al. 2002, Timbal et al. 2003, Hayhoe et al. 2004, Leung et al. 2004, Tebaldi et al. 2005, Duffy et al. 2006, Cabré et al. 2010, Salathé et al. 2010, Pierce et al. 2013a). In this study, we rely on dynamical downscaling to simulate Sierra Nevada hydroclimate. We use a high-resolution regional climate model (RCM) to explicitly simulate complex fine-scale physical processes (Caldwell et al. 2009, Salathé et al. 2008, Salathé et al. 2010, Arritt and Rummukainen 2011, Pierce et al. 2013a). Our RCM framework adequately resolves the Sierra Nevada's fine-scale topography, the associated orographic precipitation and demarcations between solid and liquid forms of precipitation. These processes are crucial for accurate representations of accumulated wintertime snowpack and spring and summertime runoff. Moreover, it more credibly simulates the strength of the snow albedo feedback over high elevations, which has an intricate spatial structure and is also a critical influence on runoff timing.

Previous studies have used RCMs to project future runoff timing changes in the Sierra Nevada. Rauscher et al. (2008) used the ICTP Regional Climate Model RegCM3 (Pal et al. 2007) to investigate future changes in snowmelt-driven runoff over the Western U.S. under the A2 emissions scenario (as described in the Special Report on Emissions Scenarios; Nakicenovic et al. 2000). They found that increases in January through March temperature of approximately

3-5° C could cause runoff to occur as much as two months earlier in the late 21st-century compared to a baseline period (1961–1989).

Future runoff timing projections in Rauscher et al. (2008) are only for one forcing scenario and for a small number of GCMs, yielding limited information about most-likely outcomes and the associated model spread. Regionalizing a large number of GCMs is necessary to quantify ensemble-mean and uncertainty statistics, but is impractical due to the high computational cost of RCMs. This shortcoming of RCMs and dynamical downscaling highlights the need to develop a technique to project high-resolution future runoff timing in a way that fully samples the GCMs without a heavy computational burden. Stewart et al. (2004) provide an example of a more computationally feasible method using a statistically-based technique, i.e. regression equations between historical precipitation, temperature and runoff timing to project future runoff timing. However, they present results for only one climate model under one forcing scenario. Moreover, as with nearly all existing statistical techniques, their methodology relies on statistical relationships based on historical variability. It is possible those relationships may no longer hold in the future, especially for changes in temperature that may far exceed those observed during the historical observation period.

The lack of a high-resolution multi-model analysis of end-of-21st-century runoff timing changes over California's Sierra Nevada serves as the primary motivation for this study. Here is a brief overview of our technique. First, five GCMs from the Coupled Model Intercomparison Project phase 5 (CMIP5, Taylor et al. 2012) are dynamically downscaled. Then, output from the dynamical simulations is used to build a simple statistical model of runoff timing; this model takes advantage of dynamical downscaling's physical credibility but is computationally efficient, allowing us to produce a large ensemble of runoff timing projections. Using the statistical model, we project runoff timing changes for all available CMIP5 models and future emissions scenarios examined in the IPCC Fifth Assessment Report (Van Vuuren et al. 2011). This allows for the quantification of ensemble-mean future runoff timing changes in the Sierra Nevada and its associated uncertainty due to inter-model GCM spread, as well as the consequences associated with choice of emissions scenarios.

This chapter is organized as follows: Section 3.2 describes the dynamical downscaling model configuration, and provides an observational evaluation of its performance. Section 3.2 also presents dynamically-downscaled end-of-21st-century changes to runoff timing. Section 3.3 describes the statistical runoff timing model and its evaluation, as well as statistically-based runoff timing projections for the full CMIP5 GCM ensemble under for all forcing scenarios. This section quantifies ensemble-mean runoff timing changes, ranges due to intermodel variability, and consequences stemming from choice of forcing scenario. Section 3.4 presents a discussion of the results. Finally, section 3.5 summarizes the major findings of this study and their implications.

3.2 Dynamical model set-up, evaluation and results

3.2.1 Dynamical model set-up

Dynamical downscaling is performed using the Weather Research and Forecasting (WRF) model version 3.5 (Skamarock et al. 2008). WRF is coupled to the community Noah land surface model with multi-parameterization options (Noah-MP, Niu et al. 2011). Three one-way nested domains are used to represent the complex topography of California and the Sierra

Nevada as accurately as possible (Fig. 3.1a). The outermost domain spans the entire U.S. West Coast and adjacent Pacific Ocean at 27 km horizontal resolution. The middle domain, at 9 km resolution, covers all of California. Finally, the innermost domain, at 3 km resolution, spans the eastern edge of the Central Valley to the leeside of the California Sierra Nevada Mountains (Fig. 3.1b); this domain is the focus of this study.

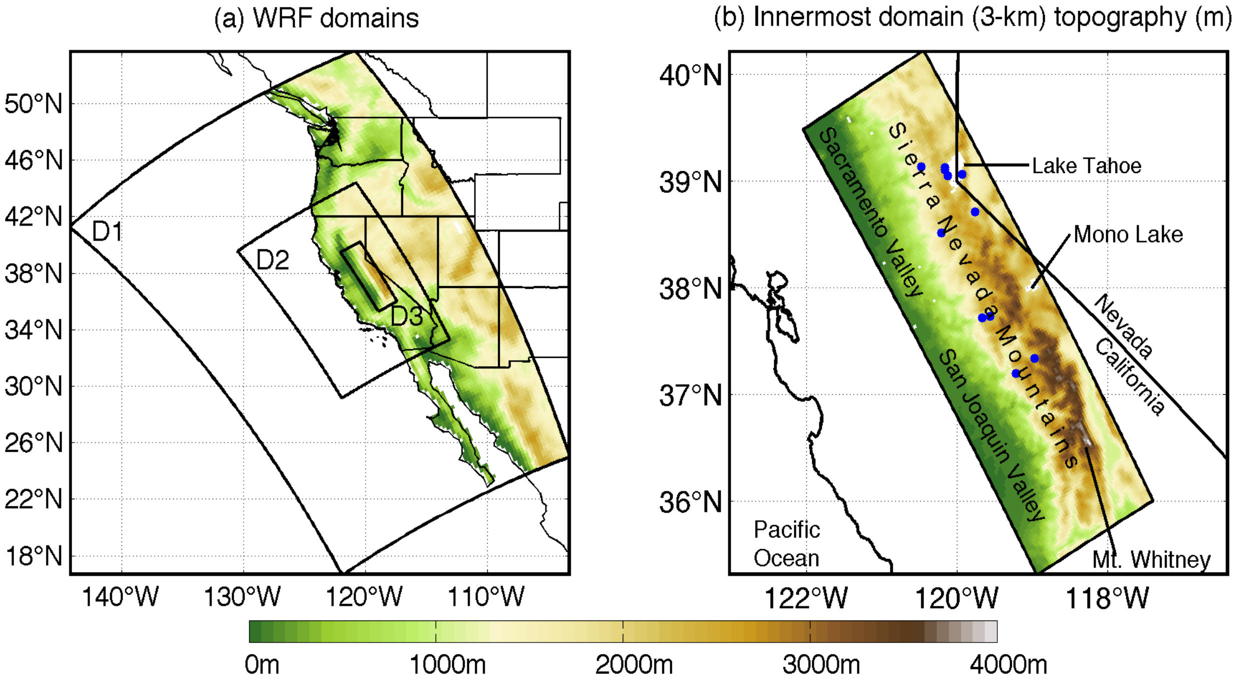

Fig. 3.1: (a) Model setup, with three nested WRF domains at resolutions of 27, 9, and 3 km (from the outermost to innermost domain). Topography (m) is shown at the resolution of the 27km domain in color and black lines show boundaries for US states. (b) Topography (m) of the innermost domain (3-km resolution) of the regional simulation, with the state borders of California and Nevada in black. Blue circles show the locations of 11 USGS-HCDN 2009 streamflow gauges used for model evaluation.

In each domain, all variables within five grid cells from the horizontal lateral boundary are relaxed toward the corresponding values at the boundaries. To provide a better representation of surface and boundary layer processes, the model's vertical resolution is enhanced near the surface, with 30 out of 43 total sigma-levels below 3 km. WRF parameterization testing has been done to optimize the model's performance in hydroclimate simulations, with the aim of improving the realism of simulated snowpack and streamflow processes in the Sierra Nevada. The package of physical parameterizations consists of the New Thompson microphysics scheme (Thompson et al. 2008), Dudhia shortwave radiation scheme (Dudhia 1989), Rapid Radiative Transfer Model longwave (RRTM) longwave radiation scheme (Mlawer et al. 1997), MYNN Level 2.5 surface/boundary layer scheme (Nakanishi and Niino 2006), and Old Kain-Fritsch cumulus convection scheme (Kain and Fritsch 1990). Spectral nudging of temperature, zonal and meridional winds, and geopotential height is employed above the boundary layer (roughly 850 hPa) over the outermost 27 km resolution domain.

Climate changes signals are produced from a single baseline simulation and five future simulations. The baseline simulation spans October 1991 to September 2001 (water years 1992–2001; hereinafter “WY 1992–2001”) and is a dynamical downscaling of the National Centers for Environmental Prediction’s 6-hourly North America Regional Reanalysis (NARR; Mesinger et al. 2006). NARR is a relatively coarse-resolution (32 km) reanalysis dataset that provides the lateral boundary forcings and initial conditions for the outermost WRF domain in Fig. 3.1a. The baseline simulation allows us to evaluate the model’s ability to simulate regional runoff timing based on a comparison to observational data (Section 3.2.2) and serves as a climate state against which we can compare future climate simulations to measure change.

Using the same model configuration as the baseline, we perform a five-member ensemble of dynamical downscaling experiments to simulate a future end-of-21st-century climate. The simulations go from October 2091 to September 2101 (water years 2092–2101, hereinafter “WY 2092–2101”). We dynamically downscale GCM experiments forced by the Representative Concentration Pathway 8.5 (RCP8.5) forcing scenario (Riahi et al. 2011). Out of all available CMIP5 GCMs forced by RCP8.5, we select five (CNRM-CM5, GFDL-CM3, INM-CM4, IPSL-

CM5A-LR, and MPI-ESM-LR). These GCMs approximately sample the range of end-of-21st century near-surface temperature and precipitation changes over California (Walton et al. 2016).

To produce boundary conditions for the future WRF simulations, we add a perturbation reflecting the mean change in GCM climatology to NARR data for WY 1992–2001, following Schar et al. (1996), Hara et al. (2008), Kawase et al. (2009) and Rasmussen et al. (2011). To calculate these GCM climate changes, we first quantify the differences in GCM monthly climatology between the historical and RCP8.5 experiments (2081–2100 average minus 1981–2000 average). Differences are calculated for temperature, humidity, zonal and meridional winds, and geopotential height. Then, for each of the five dynamically-downscaled GCMs, we perturb the baseline 6-hourly NARR reanalysis data for each month by the corresponding monthly mean climatological change. The perturbed NARR fields then serve as WRF boundary conditions for five future climate simulations. This method allows us to assess how WY 1992–2001 would transpire if the mean climate were altered to reflect the climate changes projected by each of five GCMs. It allows us to quantify how the climate change signals simulated in the GCMs are expressed at the regional scale, without the future simulations being subject to significant biases in mean state often found in GCMs. For additional information on model setup, parameterizations and design of future simulations, the reader is referred to Walton et al. (2016).

3.2.2 Baseline runoff timing climatology and model evaluation

We first evaluate WRF's ability to simulate surface runoff timing during the baseline period. As a measure of runoff timing, we consider the date in the water year (October 1 – September 30; hereinafter WY) by which 50% of the cumulative WY surface runoff has occurred (R50). R50 (often called the center of runoff volume) is widely used as a metric of snowmelt timing (Stewart et al. 2004, Stewart et al. 2005, McCabe and Clark 2005, Hayhoe et al. 2007, Kim and Jain 2011, Khattak et al. 2011). Regonda et al. (2005) suggest that R50 is a more robust indicator of snowmelt timing (in its relation to climatic variability and change) than the day of peak flow. In this paper, we use R50 both for model evaluation and as a metric to diagnose future changes to runoff timing.

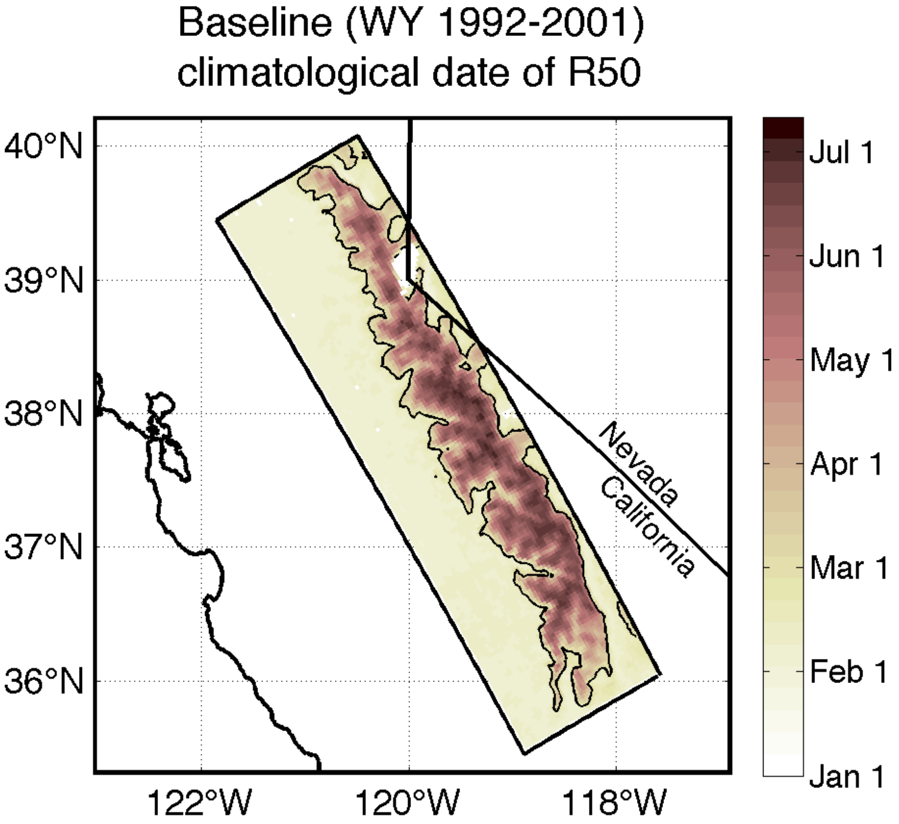

Fig. 3.2: Baseline (October 1991–September 2001) climatological date of R50, which represents the date in the water year (October 1–September 30) by which 50% of the cumulative surface runoff has occurred. The black contour outlines grid points with climatological R50 occurring on or after March 1st.

Fig. 3.2 presents the baseline (WY 1992–2001) climatological date of R50 in the 3 km domain (seen in Fig. 3.1b). Climatological R50 generally occurs after March 1st throughout the Sierra Nevada and shifts to even later in the water year as both elevation and the fraction of precipitation as snow (S/P) increase. At lower elevations in the Northern Sierras where the annual S/P (not shown) ranges from 0.6 to 0.8, climatological R50 generally occurs before the start of summer. However, mid to high elevations over the Central and Southern Sierras have a higher S/P ratio (0.8 to 0.95), which leads to snowmelt-driven surface runoff throughout the summer months, pushing back climatological R50. For example, R50 in the mountains just southwest of Mono Lake occurs as late as the beginning of July. Throughout the Central Valley, Owens Valley and western Great Basin Desert (along the California-Nevada border), annual precipitation is low, and any precipitation typically falls as rain (S/P < 0.2), so surface runoff timing matches precipitation timing.

For this study, we consider surface runoff timing changes at locations where surface runoff is mostly generated by snowmelt. The March 1st R50 cutoff date segregates snowfall-dominated grid points from rain-dominated regions or locations with minute climatological precipitation. The black contour in Fig. 3.2 denotes locations with climatological baseline R50 occurring on or after March 1st, indicating snowmelt-dominated runoff. The average baseline climatological S/P within the contoured region is 0.86, also indicative of a heavily snowfall-dominated regime whose accumulated wet-season snowpack generates spring and summer snowmelt-dominated runoff. Within the contoured region in Fig. 3.2, the median and mean climatological percentage of total water-year runoff that occurs from April through July are 78% and 69%, respectively, consistent with other snowmelt-dominated watershed in western North America examined by Stewart et al. (2005). We consider only grid points with climatological baseline R50 on or after March 1st for the rest of the study. We also exclude inland water locations in our analyses.

USGS HCDN-2009 ID	Station Name	Hydrologic Unit	Latitude	Longitude	Drainage area (sq. km)
10308200	East Fork Carson River below Markleeville Creek	16050201	38.714	-119.764	716.4
10336645	General Creek near Meeks Bay, CA	16050101	39.051	-120.118	19.6
10336660	Blackwood Creek near Tahoe City, CA	16050101	39.107	-120.162	29.8
10336676	Ward Creek at State Highway 89, near Tahoe Pines, CA	16050101	39.132	-120.157	24.7
10336740	Logan House Creek near Glenbrook, NV	16050101	39.066	-119.935	5.5
11230500	Bear Creek near Lake Thomas A. Edison, CA	18040006	37.339	-118.973	135.5
11237500	Pitman Creek below Tamarack Creek, CA	18040006	37.198	-119.213	59.8
11264500	Merced River at Happy Isles Bridge, near Yosemite, CA	18040008	37.731	-119.558	468.0
11266500	Merced River at Pohono Bridge, near Yosemite, CA	18040008	37.716	-119.666	833.1
11315000	Cole Creek near Salt Springs Dam, CA	18040012	38.519	-120.212	54.0
11427700	Duncan Canyon Creek near French Meadows, CA	18020128	39.135	-120.478	25.5

Table. 3.1: Summary of information associated with observational streamflow gauges from the United States Geological Survey Hydro-Climatic Data Network-2009 used to evaluate the baseline simulation.

The model's ability to reproduce runoff timing variations during the baseline period is assessed by comparing simulated R50 to observations obtained from the United States Geological Survey Hydro-Climatic Data Network-2009 (USGS HCDN-2009, http://waterdata/usgs.gov/nwis/). The USGS HCDN-2009 is a network of streamflow gauges across the United States having the following characteristics: (1) natural streamflow least affected by direct human activities, (2) accurate measurement records, and (3) at least 20 years of complete and continuous records through WY 2009 (Slack et al. 1993; Lins 2012). We obtained daily, quality-controlled streamflow data from 11 stations for which data was available within our study domain for the baseline period. The locations of the stations are indicated in Fig. 3.1b with blue circles, and information associated with each station is summarized in Table 3.1. The 11 stations represent a variety of elevations, drainage areas and USGS eight-digit Hydrologic Unit Codes across Sierra Nevada creeks and rivers.

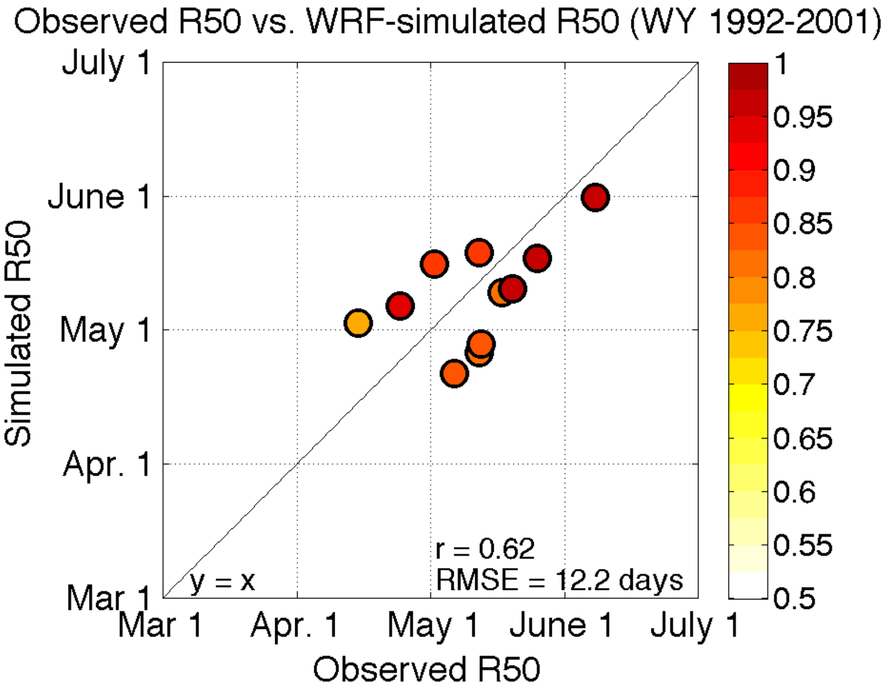

Fig. 3.3: Observed versus WRF-simulated climatological R50 at 11 USGS streamflow gauges (water years 1992–2001). Simulated R50 is estimated as the average R50 of grid points upstream of a gauge within its watershed. Colors indicate the correlation coefficient between the time series or WRF-simulated and observed values of R50. The line y = x is shown in black.

The scatter plot in Fig. 3.3 presents observed climatological R50 versus simulated climatological R50 for each of the 11 stations. Simulated climatological R50 is taken to be the average R50 of the grid points upstream of a gauge within the USGS Hydrologic Unit to which the gauge belongs. This is equivalent to assuming instantaneous transport of water from the grid cell to the stream gauge location. A portion of the biases in our model evaluation are very likely due to this primitive river routing scheme. Gauges are colored by the corresponding interannual correlation coefficient. For each gauge, simulated R50 is very well correlated with the observed R50, with temporal r ranging from 0.75 to 0.96, and the gauge-average $r = 0.87$. Fig. 3.3 also demonstrates that observed and simulated R50 dates are well-correlated spatially ($r = 0.62$) across all gauges. The root-mean-square error between observed and simulated climatological R50 is 12 days. While observed dates of climatological R50 range from early-April to early-June across all gauges, WRF spans only mid-April to late-May, slightly underestimating the observed range. Overall, the agreement between simulated and observed R50 dates indicates that the dynamical model is able to capture the main features of spatial and temporal R50 variability across the Sierra Nevada.

3.2.3 Dynamically-downscaled end-of-21st-century changes in runoff timing under RCP8.5

Fig. 3.4 (row 1) presents the dynamically-downscaled WRF end-of-21st-century change (WY 2092–2101 minus WY 1992–2001) in R50 (ΔR50, unit: days) under the RCP8.5 emissions scenario for five GCMs (CNRM-CM5, GFDL-CM3, INM-CM4, IPSL-CM5A-LR, and MPI-ESM-LR). For all simulations, advances in R50 are projected at all locations with substantial climatological baseline snowmelt-driven surface runoff. GFDL-CM3 (Fig. 3.4b) and IPSL-CM5A-LR (Fig. 3.4d) project the largest advances, with domain-average advances greater than 60 days. Advances in domain-average mean R50 for CNRM-CM5 (Fig. 3.4a) and INM-CM4 (Fig. 3.4c) are smaller, but are still nearly 6 weeks earlier.

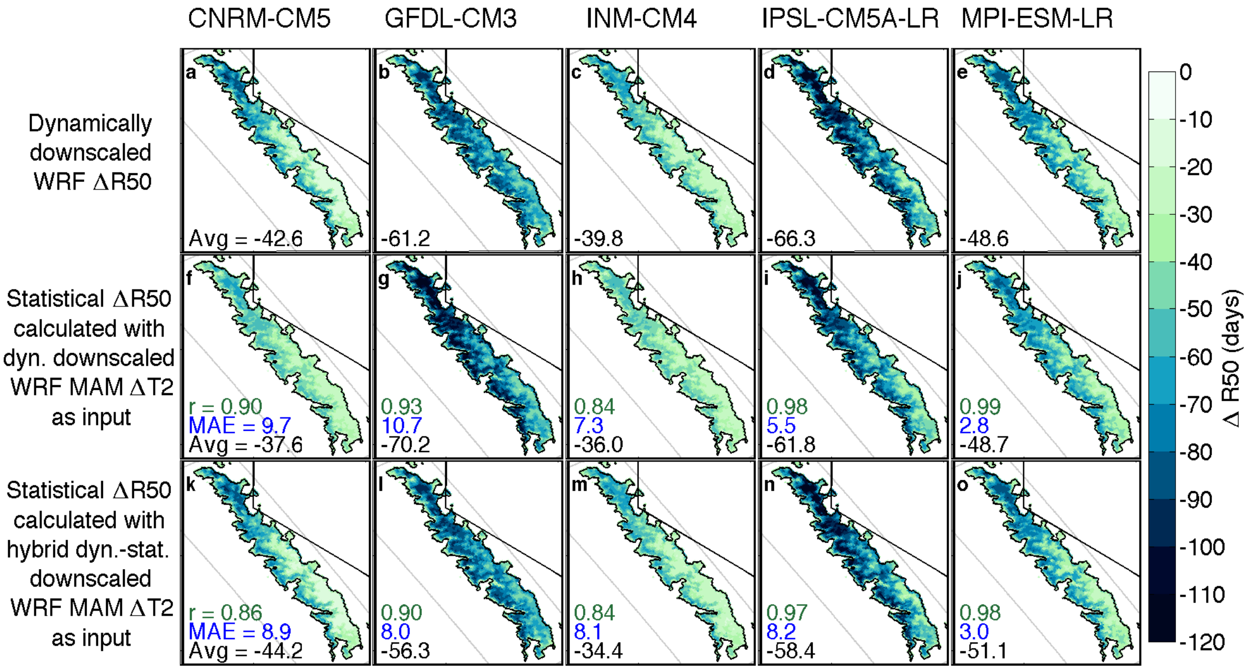

Fig. 3.4: End-of-21st-century change (water years 2092-2101 average minus 1992-2001 average, unit: days) in R50 under the RCP8.5 emissions scenario for CNRM-CM5, GFDL-CM3, inmcm4, IPSL-CM5A-LR, and MPI-ESM-LR produced from three methods. Row 1: Dynamically-downscaled WRF output. Row 2: Statistical projection using dynamically-downscaled WRF spring near-surface warming (MAM ΔT2) as input. Row 3: Statistical projection using Walton et al. (2016)'s hybrid dynamical-statistical downscaled MAM ΔT2 as input. Results are shown for locations with climatological baseline R50 on or after March 1st, and green through blue shades represent advances in R50. Black text shows domain-average in R50. Blue text in rows 2-3 denotes the mean absolute error compared to row 1. Green text in rows 2-3 denotes the spatial correlation with row 1 for each GCM.

Advances in mean R50 for all dynamically-downscaled GCMs are greatest in the Northern Sierras and the western-facing mountain slopes, and smaller at the highest elevations in the Southern Sierras. These spatial patterns can be explained primarily by dynamically-downscaled 10-year mean near-surface (2-meter) springtime (March-May) warming projections (MAM ΔT2). Fig 3.5 (row 1) presents the WRF dynamically-downscaled end-of-21st-century change in MAM ΔT2 under the RCP8.5 emissions scenario. For each of the five downscaled models, stronger warming is projected in the Northern Sierras and the western-facing mountain slopes. These regions have the greatest snow albedo feedback (Walton et al. 2016) and greatest

April 1st snow water equivalent (SWE) loss (Sun et al. 2016). This warming leads both decreases in annual mean S/P and earlier snowmelt, which together result in large advances in mean R50 in those areas. Despite significant future warming (Walton et al. 2016), the highest elevations in the Southern Sierras remain well above the freezing line. As a result, changes to S/P and snow accumulation are small at the highest elevations, and the weak advances in R50 (10-20 days) at those locations are primarily due to earlier snowmelt.

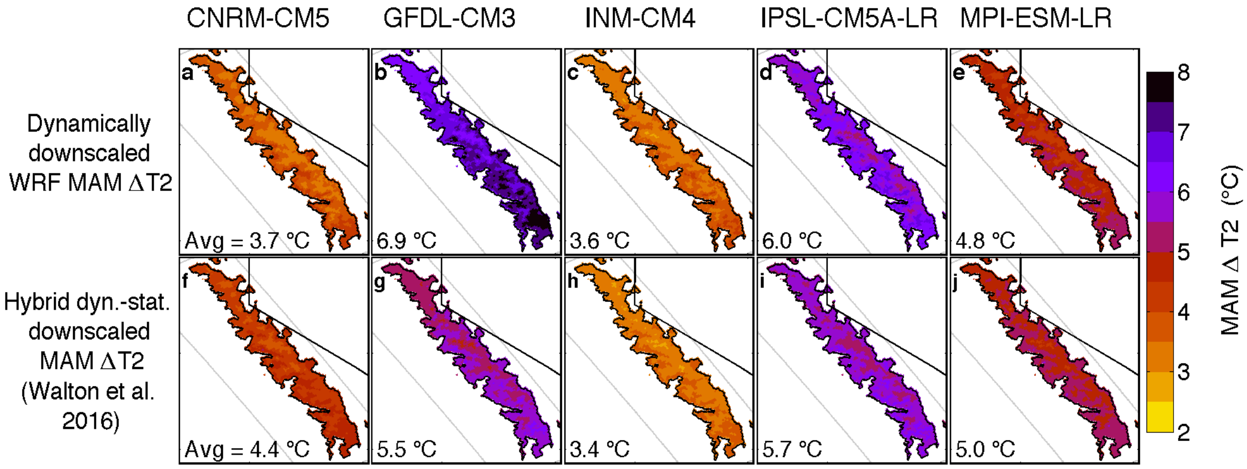

Fig. 3.5: End-of-21st-century change (water years 2092-2101 average minus 1992-2001 average) in near-surface temperature (unit: °C) averaged over March – May under the RCP8.5 forcing scenario for CNRM-CM5, GFDL-CM3, INM-CM4, IPSL-CM5A-LR, and MPI-ESM-LR. Row 1: WRF dynamically-downscaled output. Row 2: Hybrid dynamical-statistical downscaled output from Walton et al. (2016). Black text shows domain-average MAM warming.

Inter-model differences in ΔR50 can also largely be explained by differences in MAM ΔT2, as ΔR50 appears to be strongly negatively related to MAM ΔT2. GFDL-CM3 and IPSL-CM5A-LR project large MAM ΔT2, with domain-average warming of 6.0 °C and 6.9 °C, respectively. Some locations warm more than 7 °C. This strong warming explains the sizable advances in mean R50 for GFDL-CM3 and IPSL-CM5A-LR. Weaker MAM warming in INM-CM4 and CNRM-CM5 (domain-average 3.6 °C and 3.7 °C, respectively) corresponds to smaller mean R50 advances. (MPI-ESM-LR is moderate in both MAM ΔT2 and change in R50.) This link suggests MAM ΔT2 might be a reasonable predictor for ΔR50, a hypothesis that will be explored in the statistical ΔR50 model described in Section 3.3.1. In section 3.4, we also consider mean precipitation changes as a predictor for ΔR50; however, precipitation timing hardly changes in the downscaled WRF simulations, so inter-model differences in runoff timing are likely not attributed to precipitation changes.

3.3 ΔR50 Statistical model description, evaluation and results

Results in the previous section focused only on projections of end-of-21st-century changes to mean R50 under the RCP8.5 emissions scenario for five selected GCMs, and have shed light on ΔR50 spatial patterns and the relationship between ΔR50 and MAM ΔT2. They do not provide enough information to fully assess uncertainty in runoff timing changes due to intermodel spread and choice of forcing scenario. To project ΔR50 for all available CMIP5 GCMs and all forcing scenarios, we develop a computationally efficient yet physically credible statistical model. In section 3.3.1, we describe the statistical ΔR50 model and evaluate its ability to mimic dynamical results. In section 3.3.2, we use the model to project end-of-21st-century ΔR50 under RCPs 2.6, 4.5, 6.0 and 8.5 for all available CMIP5 GCMs.

3.3.1 Statistical ΔR50 model description and evaluation

As noted before, there is a negative relationship between WRF ΔR50 (Fig. 3.4, row 1) and MAM ΔT2 (Fig. 3.5, row 1). Fig. 3.6a shows the correlation coefficient for each grid point between dynamical ΔR50 and MAM ΔT2. The correlation values reflect a blend of intermodel and interannual variability, as they are calculated from annually-averaged ΔR50 and MAM ΔT2 values. This produces a sample size of 50 for each grid point (5 models × 10 water years). There is a very strong anti-correlation between ΔR50 and MAM ΔT2, with a mean spatial correlation coefficient of $r = -0.82$. That MAM ΔT2 would be a predictor for ΔR50 is physically sensible, as climatological baseline R50 for many mountainous locations falls in MAM (Fig. 3.2), and MAM runoff accounts for a significant portion of annual runoff throughout much of the Sierras. Thus we aim to build a statistical modeling framework that projects ΔR50 given MAM ΔT2 (from raw or downscaled GCM output). Section 3.4.1 discusses our choice of MAM ΔT2 as a predictor and other predictors we considered.

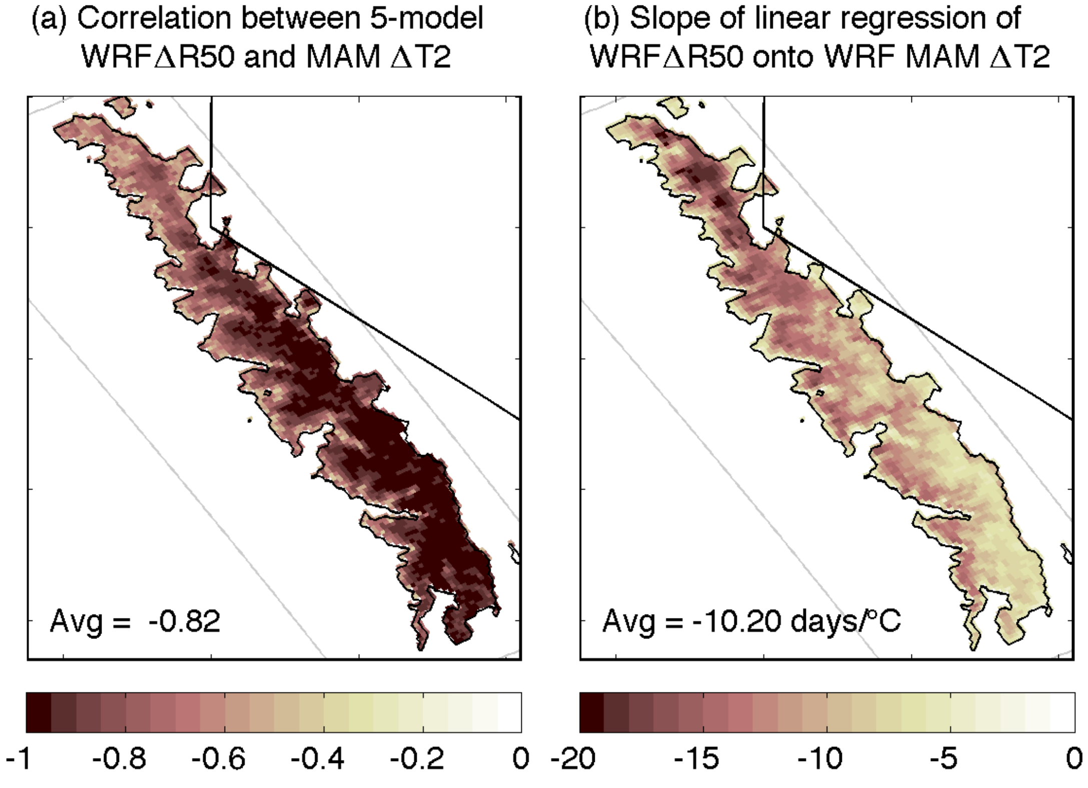

Fig. 3.6: (a) Correlation coefficient between the 5-model dynamically-downscaled change in R50 timing (ΔR50) and near-surface March-May warming (MAM ΔT2). (b) Slope of the linear regression of the 5-model dynamically-downscaled ΔR50 onto the 5-model dynamically-downscaled MAM ΔT2. This represents the linear sensitivity of ΔR50 to MAM ΔT2, or the average expected advance in R50 per degree MAM ΔT2 (unit: days/°C). Black text denotes the domain average value.

First, we linearly regress the five dynamically-downscaled ΔR50 onto the five dynamically-downscaled MAM ΔT2 for each pair of coordinates (*i,j*) in the 3 km resolution domain with climatological baseline R50 on or after March 1st. The slope (α) of this linear regression is determined by intermodel and interannual variability, i.e. 50 data points (10 water years × 5 models) for each (*i,j*) pair. Fig. 3.6b presents the spatial pattern of α, the average expected advance in mean R50 timing per degree near-surface MAM warming. In calculating α, we force the linear relationship to go through (0,0), therefore having no intercept. This is an expression of the physical constraint that one would not expect a change in the timing of R50 without a change in MAM T2. Though the domain average α is -10.2 days/°C, Northern Sierra and mid-elevation western slopes are much more sensitive, with projected changes to R50 of more than -19 days/°C. The strong sensitivity of R50 to warming at these mid-elevation locations is due to the warming-driven S/P decreases and earlier snowmelt, which conspire to advance runoff timing. Moreover, these more sensitive regions correspond well to regions of greatest projected April 1st SWE decreases (Sun et al. 2016) and greatest snow-albedo-feedback enhanced warming and snow cover loss (Walton et al. 2016). After determining α, we then predict ΔR50 with following equation:

$$\Delta R50_{GCM,i,j\ j} \cong \alpha_{i,j} * \text{MAM } \Delta T2_{\ GCM,i,j} \qquad (1)$$

The relationship between purely interannual R50 and MAM T2 anomalies is linear to a very good approximation both in the WRF simulation and observations. In WRF, the domain-average slope of the linear regression of WY 1992–2001 R50 onto MAM T2 is -11.4 days/°C (which is similar to that of the domain-average α of -10.2 days/°C). Observations show a very similar sensitivity. Fig. 3.7 presents a scatter plot of observed annual MAM T2 anomalies vs. R50 anomalies over WY 1916–2014. Observed interannual R50 and MAM T2 variations in

California are well anti-correlated (*r* = -0.67). Moreover, the observed linear sensitivity of WY 1916–2014 R50 to MAM T2 is -9.46 days/°C, which closely matches that of the simulated linear sensitivity of WY 1992–2001 R50 to MAM T2 (-11.4 days/°C). This agreement provides crucial support to the realism of both the WRF simulation and a statistical model based on the linear relationships between ΔR50 and MAM ΔT2.

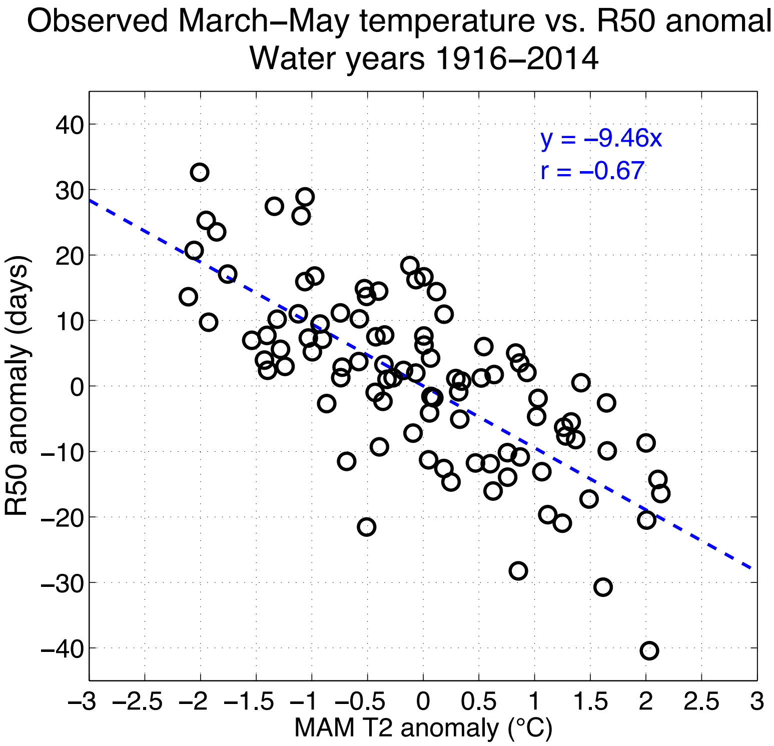

Fig. 3.7: Scatter plot of observed near-surface temperature anomalies (unit: °C) averaged over March – May (MAM T2) and observed R50 anomalies (unit: days) over water years 1916–2014. The blue line is the linear regression of WY 1916–2014 R50 onto MAM T2. Blue text denotes the slope of this linear regression as well as the correlation coefficient. MAM 2-m temperature anomalies are calculated from the National Oceanic and Atmospheric Administration's National Climatic Data Center's nClimDiv statewide temperature database (ftp://ftp.ncdc.noaa.gov/pub/data/cirs/climdiv/state-readme.txt), which includes monthly-mean maximum and minimum temperature aggregated at statewide levels for the United States for January 1895 to the present. Monthly maximum and minimum temperatures are averaged together to calculate monthly mean temperature. MAM T2 anomalies presented here are calculated from the detrended MAM time series for California. R50 anomalies are calculated from the detrended gauge-averaged R50 time series from available observations at the 11 USGS-HCDN streamflow gauges in Table 3.1 (described in section 3.2.2).

One source of error in the statistical ΔR50 model (Eq. 1) arises from approximating ΔR50 as linear function of MAM ΔT2. This error source is likely to be small because the linear correlation coefficients between the two variables are very high (Fig. 3.6a). However, we can evaluate this error source by projecting ΔR50 using the statistical model with the dynamically-downscaled MAM ΔT2 under RCP8.5 (Fig. 3.5, row 1) as input. Fig. 3.4 (row 2) presents this statistical ΔR50 projection, which can be compared to dynamically-downscaled ΔR50 (Fig. 3.4, row 1). Overall, the approximate values of ΔR50 (Fig. 3.4, row 2) almost perfectly mirror the dynamically-downscaled values (Fig. 3.4, row 1). The approximate spatial patterns are highly correlated with their dynamical counterparts ($r > 0.84$ for all GCMs). Moreover, the mean absolute errors (MAE, calculated by averaging the absolute value of the errors over the region of interest) are less than 11 days for all models, small compared to domain-average advances in R50 that range between 39 and 66 days. This comparison lends credibility to the choice to model ΔR50 as a linear function of MAM ΔT2.

To apply the statistical ΔR50 model to all GCMs and forcing scenarios, we rely on projections of MAM ΔT2 from Walton et al. (2016, hereinafter "W2016"). W2016 produced 3 km horizontal resolution monthly near-surface warming projections (ΔT2) for our study domain for all available CMIP5 GCMs under forcing scenarios RCP8.5, 6.0, 4.5 and 2.6. W2016 used a hybrid dynamical-statistical (hereinafter "hybrid") downscaling technique that relies on two large-scale predictors (regional-mean warming and east-west warming contrast) and a representation of snow albedo feedback's significant contribution to elevational variations in warming. Fig. 3.5 (row 2) presents end-of-21st-century hybrid downscaled MAM ΔT2 under RCP8.5 from W2016. This method captures the spatial pattern and approximate magnitude of

MAM ΔT2 for each of the 5 dynamically-downscaled GCMs (Fig. 3.5, row 1), including the warming enhancement due to snow albedo feedback at mid-elevations and in the northern Sierras.

To assess the error associated with the use of W2016's hybrid downscaled MAM ΔT2 as input to our statistical ΔR50 model, we compare the dynamically-downscaled ΔR50 projections under RCP8.5 (Fig. 3.4, row 1) to those calculated by the statistical ΔR50 model (Eq. 1) with the hybrid downscaled MAM ΔT2 projections of W2016 as input (Fig. 3.4, row 3). Overall, the spatial correlations between these ΔR50 patterns and WRF's dynamically downscaled patterns are very high ($r > 0.84$) and the MAE values are low compared to the magnitude of ΔR50, indicating that the use of hybrid downscaled MAM ΔT2 input reproduces dynamically-downscaled ΔR50 projections reasonably well. Still, we note some minor discrepancies. For GFDL-CM3, INM-CM4 and IPSL-CM5A-LR, hybrid projections of MAM ΔT2 by W2016 (Fig. 3.5, row 2) underestimate the dynamically-downscaled MAM ΔT2 somewhat (Fig. 3.5, row 1). As a result, using hybrid downscaled MAM ΔT2 underestimates the magnitude of the dynamically-downscaled ΔR50 for those models. Similarly, W2016 slightly overestimates MAM ΔT2 for CNRM-CM5 and MPI-ESM-LR, which results in a small overestimation of mean R50 advances for those GCMs.

3.3.2 Statistical results for full GCM ensemble and all forcing scenarios

Using the statistical ΔR50 model (Eq. 1) with the W2016 hybrid dynamical-statistical downscaled MAM ΔT2 as input, we generate projections of mean changes in future runoff timing for all available CMIP5 GCMs under four forcing scenarios: RCPs 2.6, 4.5, 6.0 and 8.5. Fig. 3.8 (row 1) presents ensemble-mean changes in R50 for RCPs 2.6, 4.5, 6.0, and 8.5. The spatial patterns of ΔR50 are qualitatively similar for each forcing scenario, with the magnitudes increasing with forcing scenario. While all locations show some advance, the largest advances are found at elevations between 2000 m and 2750 m and are generally on the western slope of the Sierra Nevada. In some locations, ensemble-mean R50 is projected to advance by more than 80 days under RCP8.5. We also note that for RCP8.5, the ensemble-mean domain-average ΔR50 is -49.2 days, which is very close to that of the five-model dynamically downscaled ensemble (-51.7 days). This supports the idea that the five GCMs we select for dynamical downscaling approximately represent the GCM ensemble, and that hybrid downscaling can be used to capture their behavior.

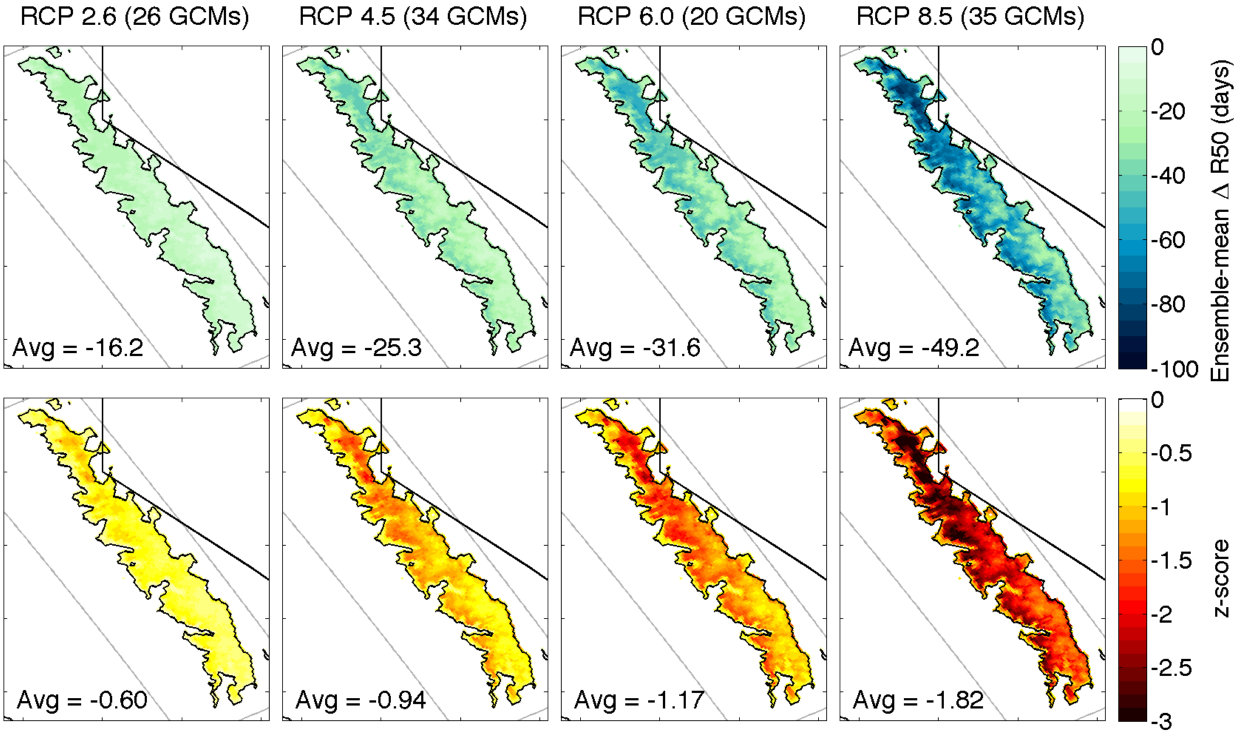

Fig. 3.8: Row 1: Ensemble-mean statistical projections of end-of-21st-century change (water years 2092-2101 average minus 1992-2001 average) in R50 (unit: days) under emissions scenarios RCP4.5, RCP6.0 and RCP8.5. Row 2: The associated z-score for the ensemble-mean change in R50, which is calculated by dividing the mean R50 change by the standard deviation of R50 of a 20-year baseline (water years 1982-2001). Black text denotes the domain average value. The number of GCMs included in the ensemble-mean is denoted in the title.

Ensemble mean R50 changes are substantial when compared with the interannual variability of the baseline period. To better quantify baseline interannual variability, we extend the baseline simulation to span WY 1982–2001. This 20-year simulation uses the same modeling framework described in Section 3.2.1, but allows for better quantification of interannual variability than the 10-year baseline (WY 1992–2001) used for climate change analysis. Fig. 3.8 (row 2) presents z-scores associated with the ensemble-mean changes in R50 in Fig. 3.8 (row 1). The z-score is calculated by dividing the mean R50 change by the standard deviation of R50 for extended baseline period (WY 1982–2001), and therefore represents how far outside the baseline WY 1992–2001 R50 distribution an average future R50 is. Under RCP2.6 and 4.5, the domain-average ensemble-mean z-scores are -0.60 and -0.94, respectively. Under RCP6.0, the domain-average ensemble-mean z-scores is -1.17, which translates to a future mean R50 equivalent to the 12th percentile of baseline R50 distribution. Ensemble-mean R50 changes compared to the baseline's interannual variability are most dramatic for RCP8.5, as the domain-average z-score is -1.82, approximately the 3rd percentile of baseline R50. Moreover, the ensemble-mean domain-average R50 is projected to be earlier than that of any baseline year under RCP8.5, indicating a dramatic change in runoff timing.

Fig. 3.9 shows the elevational profile of ΔR50 for the ensemble-mean (thick solid line) under the four RCPs. Elevations are binned every 100m, and ΔR50 for a given elevation bin is the spatial average across grid cells within the bin. Light gray shading represents the standard deviation of R50 over WY 1982–2001 at each elevation, a measure of interannual variability. Under RCP8.5 (Fig. 3.9d), ensemble-mean ΔR50 has a greater than one standard deviation advance for all elevations above 1400m. Ensemble-mean ΔR50 is outside of one standard deviation in the 2000–3100 m elevation band under RCP6.0 (Fig. 3.9c), but near or less than one standard deviation for RCP4.5 and 2.6 (Fig. 3.9a-b).

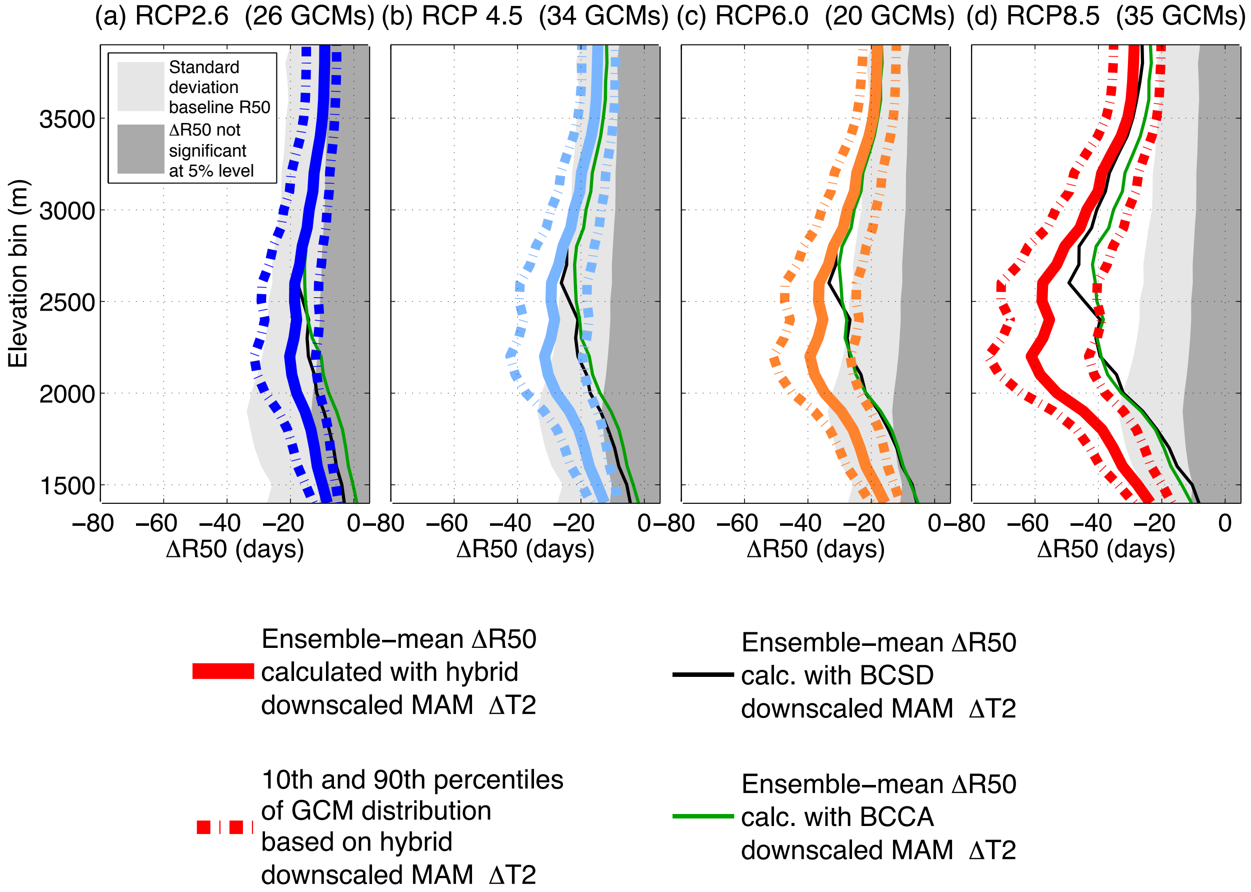

Fig. 3.9: Statistical projections of end-of-21st-century change (water years 2092-2101 average minus 1992-2001 average) in R50 as a function of elevation (binned every 100m) under emissions scenarios RCP2.6, 4.5, RCP6.0 and RCP8.5. Solid colored lines represent the ensemble-mean R50 change calculated with hybrid dynamical-statistical spring warming as input, while dashed colored lines represent the 10th and 90th percentiles of this GCM distribution. Light gray shading denotes the standard deviation of R50 for the extended baseline period (water years 1982-2001). The region outside of the dark gray shading denotes mean changes in R50 that are significant at the 5% level according to a one-tailed t-test. Thin black (green) lines represent the ensemble-mean R50 change calculated with BCSD-downscaled (BCCA-downscaled) spring warming as input. Results are shown for locations with climatological baseline R50 on or after March 1st. The number of GCMs included in the hybrid-downscaled GCM ensemble is denoted in the title.

Ensemble projections also allow for the quantification of uncertainty in R50 projections due to GCM spread, and thick dashed lines in Fig. 3.9 represent the 10th and 90th percentiles of the GCM spread in ΔR50 when calculated with hybrid downscaled MAM ΔT2. For all forcing scenarios, this measure of GCM spread is greatest in the 2000–3000m elevation band, which reflects the spread in MAM ΔT2 projections at those elevations (Walton et al. 2016). Under RCP8.5, despite an intermodel ΔR50 range of more than 30 days at some elevations, the advance in R50 is outside the range of interannual variability for all models in the 2000–3200m elevation band.

To shed light on the significance of these changes, we perform a one-tailed t-test that assesses the likelihood that a 10-year sample with a given mean shift in R50 could be drawn from the same population as the baseline WY 1982–2001 R50 distribution. To do this, we assume the future period is a 20-year sample. The sample size is $n = 20$, so nineteen degrees of freedom are used. The region outside of the dark gray shading in Fig. 3.9 represents changes in mean R50 timing that are significant at the 5% level for each elevation. Under RCP6.0 and 8.5 (Fig. 3.9c-d), ΔR50 is significantly different at the 5% level from the baseline mean for all elevations and all GCMs. Although RCP2.6 has smaller absolutely R50 changes, ensemble-mean changes are still significant at the 5% level in the 1800-3300m elevation bin, but not for all GCMs. Under RCP4.5 (Fig. 3.9b), ensemble-mean ΔR50, despite being within the range of interannual variability at most elevations, is significant at all elevations.

Lastly, under RCP8.5, ΔR50 is significantly different at the 1% level from the baseline mean for all elevations and all GCMs (not shown). Estimates of recent global greenhouse gas emissions indicate they are closely approaching and possibly exceeding the RCP8.5 pathway (Le Quéré et al. 2015). Should emissions continue to follow RCP8.5, it is very likely that future advances in snowmelt runoff timing will be dramatically different from internal climate variability.

3.4 Discussion

In this section, we discuss our choice of MAM ΔT2 as the predictor in the statistical ΔR50 model (Eq. 1), as well as some limitations of this choice. We also examine the origin of the statistical ΔR50 model's skill, as well as caveats of this study and our methodology.

3.4.1 Choice of spring warming as the predictor for runoff timing changes

Precipitation changes (especially its seasonality) may also affect future runoff timing, thereby suggesting its inclusion as a valid co-predictor. Previous studies have not found robust changes in California's mean precipitation, and have noted only modest projected changes in mean precipitation that are small compared to natural variability (Pierce et al. 2013b, Cayan et al. 2008, Duffy et al. 2006). Nevertheless, testing was done to include mean wet-season precipitation changes as a co-predictor along with MAM ΔT2 in the statistical ΔR50 model, but little improvement was seen. Using dynamically-downscaled MAM ΔT2 as input to the statistical ΔR50 model (Eq. 1), the model-average MAE is 7.2 days (Fig. 3.4, row 2) compared to the WRF dynamical ΔR50 projections (Fig. 3.4, row 1). In a statistical model built using both MAM ΔT2 and mean wet-season (December-March) precipitation changes as co-regressors and input, less than 4% improvement was seen in the model-average MAE. Additional testing was done to determine if ΔT2 or precipitation changes averaged over other months produced a more skillful model than one that relies on only MAM ΔT2, but no value was gained. Including changes to April 1st SWE as a co-predictor also added no value to the model. Overall, this indicates that advances in R50 are nearly entirely driven by warming, consistent with previous studies of observed and projected runoff timing changes over the Sierra Nevada and Western United States (e.g. Stewart et al. 2004).

We note that the dynamical downscaling framework imposes identical interannual variability levels between the baseline and future time slices. Possible changes to interannual variability patterns in the 21st century, for example the El Nino-Southern Oscillation phenomenon (Cai et al. 2014), could significantly impact overall precipitation levels and timing through atmospheric teleconnections, a factor that is not fully accounted for in this study. However, as the focus of this study is the change in mean runoff timing, it is difficult to see how the absence of El-Nino-driven changes in overall precipitation would affect the conclusions significantly.

3.4.2 Importance of warming patterns that consider snow albedo feedback in projecting ΔR50

The ΔR50 statistical model (Eq. 1) is designed to produce ΔR50 outcomes given MAM ΔT2 (from raw or downscaled GCM output) as input. In section 3.3.1, we assessed errors in the statistical ΔR50 projections associated with use of the hybrid downscaled MAM ΔT2 projections of W2016 as input (Fig. 3.4, row 2) compared to the use of WRF dynamically-downscaled MAM ΔT2 projections (Fig. 3.4, row 3). Both WRF dynamically-downscaled and hybrid-downscaled MAM ΔT2 projections explicitly consider warming enhancement due to snow albedo feedback (SAF) and its intricate spatial structure (Fig. 3.5). Here we quantify the importance of using high-resolution warming patterns that explicitly consider SAF as input to the ΔR50 statistical model.

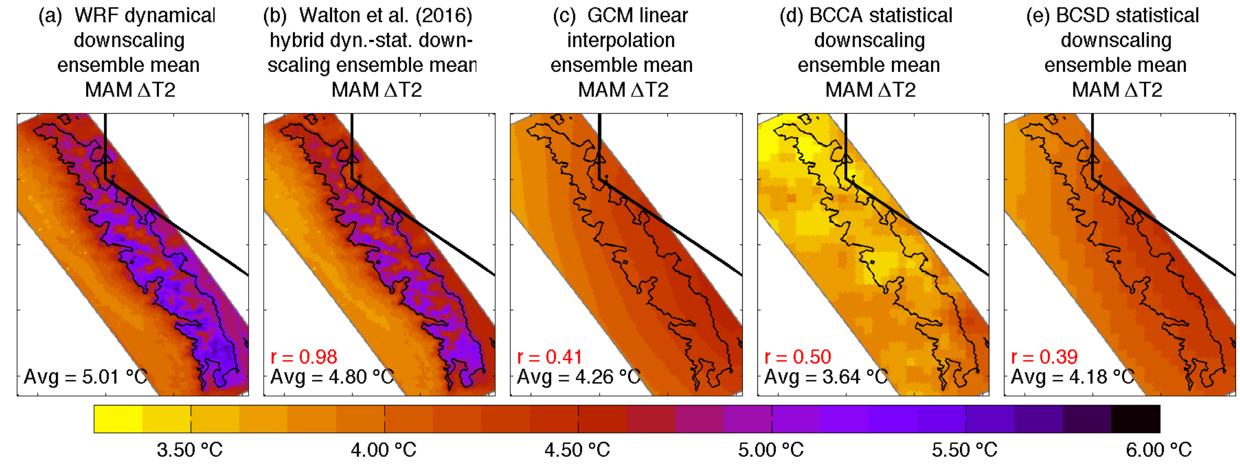

Fig. 3.10: End-of-21st-century change in near-surface March–May temperature (unit: °C) under the RCP8.5 forcing scenario averaged over five GCMs (CNRM-CM5, GFDL-CM3, INM-CM4, IPSL-CM5A-LR, and MPI-ESM-LR) downscaled using 5 methods: (a) WRF dynamical downscaling, (b) Walton et al. (2016)'s statistical downscaling, (c) linear interpolation, (d) BCCA, and (e) BCSD. Black text denotes domain-average warming within black contoured region. Red text in b-e denotes the spatial correlation with (a) within the black contoured region.

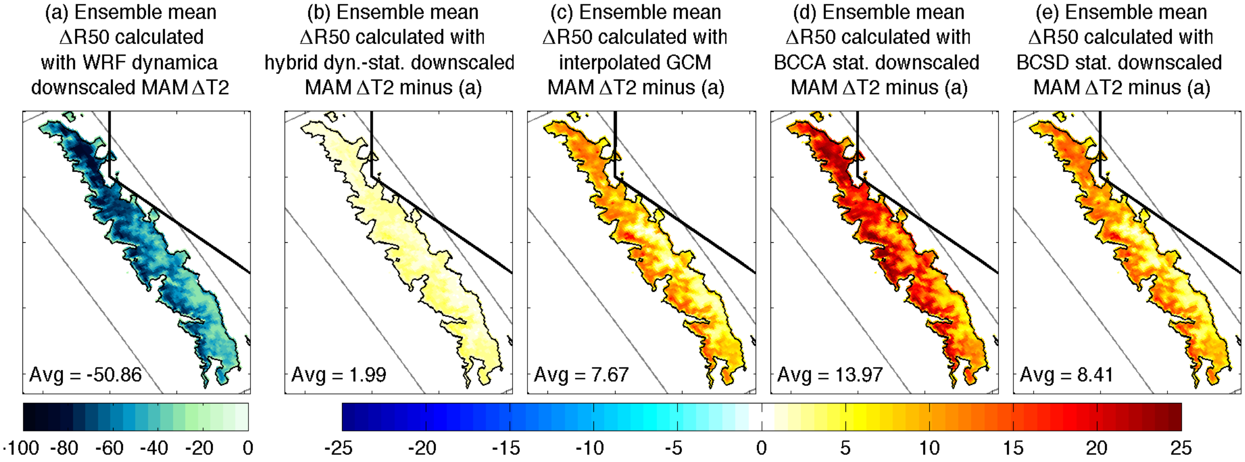

Fig. 3.11: Statistical projection of end-of-21st-century change in R50 (unit: days) under the RCP8.5 forcing scenario averaged over five GCMs (CNRM-CM5, GFDL-CM3, INM-CM4, IPSL-CM5A-LR, and MPI-ESM-LR) calculated with MAM ΔT2 from **(a)** WRF dynamical downscaling, **(b)** hybrid dynamical-statistical downscaling of Walton et al. (2016), **(c)** linear interpolation of GCM output, **(d)** BCCA statistical downscaling, and **(e)** BCSD statistical downscaling. In **b-e, a** is subtracted to highlight differences. Results are shown for locations with climatological baseline R50 on or after March 1st, and black text denotes domain-average value.

For this exercise, we consider three methods of projecting MAM ΔT2 that do not consider SAF, at least not explicitly: linear interpolation of GCM output, Bias Correction and Constructed Analogs (BCCA; Hidalgo et al., 2008; Maurer and Hidalgo, 2008) and Bias Correction with Spatial Disaggregation (BCSD; Wood et al., 2002; Wood et al., 2004; Maurer, 2007). BCCA and BCSD are two commonly used statistical downscaling techniques. Linear interpolation is a simple and naïve method of downscaling GCM output that represents a baseline measure of downscaling skill against which the other methods can be compared. BCCA and BCSD temperature projections were obtained online from the archive of Downscaled CMIP3 and CMIP5 Climate and Hydrology Projections [Reclamation, 2013]. BCCA temperature projections are available as daily maximum and minimum temperatures at 1/8 degree resolution; we average these together to produce monthly average temperatures. Similar processing was applied to BCSD maximum and minimum temperatures, which are available as monthly averages.

Fig. 3.10 presents the end-of-21st-century change (WY 2092-2101 average minus WY 1992-2001 average) in near-surface MAM temperature under the RCP8.5 forcing scenario averaged over five GCMs (CNRM-CM5, GFDL-CM3, INM-CM4, IPSL-CM5A-LR, and MPI-ESM-LR) downscaled using 5 methods: (a) WRF dynamical downscaling, (b) hybrid downscaling, (c) linear interpolation, (d) BCCA and (e) BCSD. Both dynamical downscaling (Fig. 3.9a and Fig 3.5a-e) and hybrid downscaling (Fig. 3.9b and Fig. 3.5f-j) reveal warming amplification due to snow cover loss, a crucial factor that modulates warming. However, warming patterns produced through linear interpolation (Fig. 3.9c), BCCA (Fig. 3.9d) and BCSD (Fig. 3.9e) do not feature a warming enhancement at mid-elevations and in the southern Sierras linked to snow cover loss and SAF. We note that warming signals produced through BCSD downscaling are nearly identical to those produced using linear interpolation. This similarly arises because BCSD applies the same bias correction to both the baseline and future time periods, and thus BCSD climate change signals closely match those produced through linear interpolation of raw GCM output. For a comprehensive analysis of the difference in warming patterns that arise through the various downscaling methods, the reader is referred to W2016.

Next, we analyze the patterns of runoff timing that arise from the ΔR50 statistical model (Eq. 1) calculated with the five methods of downscaled MAM ΔT2 in Fig. 3.10 as input. Fig. 3.11a presents WRF-generated ΔR50 values averaged over the five GCMs, while Fig. 3.11b-e show the differences between WRF ΔR50 outcomes and those produced with MAM ΔT2 from the other four downscaling methods. Using W2016's hybrid downscaled MAM ΔT2 model as input to the ΔR50 statistical model produces ensemble-mean ΔR50 outcomes (Fig. 3.11b) very similar to those produced with WRF dynamically downscaled MAM ΔT2 as input (domain average mean absolute error is only 1.99 days). However, ΔR50 outcomes produced using linearly interpolated, BCCA and BCSD (Fig. 3.11c-e) MAM ΔT2 systematically underestimate the magnitude of ΔR50 in WRF (Fig. 3.11a), with domain-average differences of 7.67, 13.97 and 8.41 days, respectively. Differences between ΔR50 outcomes produced using WRF MAM ΔT2 and those produced using linear interpolation, BCCA and BCSD are greatest in the Northern Sierras and at mid-elevations on the western slopes. In these regions, linear interpolation, BCCA and BCSD systematically underestimate warming due to their inability to capture warming amplification due to SAF. For example, ΔR50 outcomes produced using BCCA MAM ΔT2 are 20-30 days less than those produced using WRF's MAM ΔT2 at these locations. However, at the highest elevations (>3000 m), WRF's MAM ΔT2 (Fig. 3.10a) roughly agrees with that of linear interpolation (Fig. 3.10c) and BCSD (Fig. 3.10e). This approximate agreement in MAM ΔT2, together with a weaker linear sensitivity of ΔR50 to MAM ΔT2 at the highest elevations (Fig.

3.6b) are the main reasons ΔR50 calculations from WRF's MAM ΔT2 are within 10 days of those calculated from linear interpolated or BCSD MAM ΔT2 at the highest elevations.

This idea is further explored in Fig. 3.9, where thin black (green) lines show the elevational profile of ensemble-mean ΔR50 calculated with BCSD-downscaled (BCCA-downscaled) spring warming as input. As mentioned before, the elevational profile of ΔR50 calculated with BCSD-downscaled spring warming is nearly identical to that produced using linearly interpolated GCM spring warming. For each RCP, using BCSD or BCCA downscaled MAM ΔT2 as input to the R50 statistical model (black and green lines, respectively) underestimates the magnitude of the R50 advance at elevations below 2700m compared to that calculated using W2016's hybrid downscaled MAM ΔT2 (solid colored lines). This is due to the underestimation of mid-elevation (2000-2700m) warming in GCMs that stems from their inability to resolve SAF. Overall, this exercise and Figs. 3.9-3.11 indicate the importance of high-resolution warming patterns that explicitly consider SAF as input to the statistical ΔR50 model in order to mimic the ΔR50 outcomes projected by WRF (section 3.2.3).

3.5 Summary and Implications

By developing a statistical model for the date in the water year (WY, October 1 – September 30) by which 50% of the cumulative WY surface runoff has occurred (R50), we are able to create multi-model projections of high-resolution changes to Sierra Nevada runoff timing for the end-of-the-21st century under a range of emissions scenarios. Projections are based on linear relationships between springtime warming and runoff timing changes (WY 2092–2101 average minus WY 1992–2001 average) according to five dynamically downscaled GCMs.

Hybrid dynamical-statistical downscaled temperature that explicitly accounts for snow albedo feedback (Walton et al. 2016) is then used to project runoff timing changes for all GCMs within forcing scenarios RCP2.6, 4.5, 6.0, and 8.5. Evaluation of the statistical model for runoff timing projections shows that it is able to successfully reproduce dynamically downscaled solutions and, moreover, can credibly downscale any GCM given only its regionalized springtime temperature change.

Warming-driven advances in R50 are greatest under RCP8.5, the most aggressive forcing scenario. Advances of up to 60 days are projected in the ensemble-mean for the 2000–2750m elevation band, with some models projecting advances of over 75 days. Runoff timing over these elevations is most sensitive to temperature changes given its proximity to the freezing line, where warming enhanced by snow albedo feedback leads to strong shifts toward more liquid precipitation and advances in snowmelt timing. Above and below this elevation band, advances are still significant, but lower in magnitude (20–50 days). Advances in runoff timing are also found in warming scenarios that curtail greenhouse gas emissions, but are significantly less than in RCP8.8. For example, under RCP4.5, which is arguably the most realistic mitigation scenario given estimates of recent global greenhouse gas emissions (Le Quéré et al. 2015), runoff timing advances in the 2000–2750m elevation band are reduced to under 40 days, roughly one-third less than under RCP8.5. Similarly, runoff timing advances at higher (e.g. above 2800m) and lower (e.g. below 2000m) elevations are less severe in both RCP4.5 and RCP6.0. It is interesting to note that under RCP2.6, the most optimistic forcing scenario (and perhaps unrealistically optimistic), though mean runoff timing changes are generally within the envelope of interannual variability at all elevations, they are still statistically significant in the 1800–3300m elevation band.

An advance in runoff by 50–70 days is likely to have major implications for California's water resource infrastructure, and it would be helpful from both a societal and policy perspective to examine whether the current infrastructure – built on the assumption that the snowpack of the Sierras melts gradually throughout the dry season – can accommodate such drastic changes to snowmelt timing. Reservoir operational rule curves specify the monthly target water level for each reservoir. Rule curves were developed in the mid-1900s when most of California's dams were built, and the historical data used inform them reflects the hydroclimate of only the first half of the 20th century (Willis et al. 2011). Given significant changes to snowmelt runoff timing found in this study, it will likely be necessary to update rule curves to avoid detrimental and wasteful water releases. Changes to runoff timing will also have important consequences for water rights tied to specific seasons or months. Lastly, shifts in runoff timing have implications beyond California's water resources, including aquatic ecosystem vitality, wildfire activity (via soil moisture changes) and recreational activities throughout the Sierra Nevada. Long-term climate and streamflow observations throughout the Sierra Nevada will continue to be crucial for detection of runoff timing trends.

4 Future soil moisture drying in the Sierra Nevada

4.1 Introduction

Understanding the response of soil moisture (SM) in the Sierra Nevada Mountains to future warming scenarios is critical to determining impacts of regional climate change. First, wildfire risk in the Western US is strongly linked to SM, as the depletion of SM results in very dry foliage and surface fuels, thereby increasing the potential for rife wildfire (Swetnam and Betancourt 1998). Second, because SM is critical to plant development and ecosystem productivity, changes in SM could cause changes to vegetative cover. Third, SM drying may expand the spatial extent, severity and frequency of droughts over the Western US (Sheffield and Wood 2008), and droughts have extreme economic and social impacts (Howitt et al. 2014). Lastly, because the Sierra Nevada Mountains provide more than 60% of California's consumptive water (Bales et al. 2011), it is critical to assess the response of its snow-dominated hydrological cycle to climate change in order to satisfy California's municipal, agricultural, and ecological freshwater demands in the 21st century.

In the Sierra Nevada, future SM may increase early in the snow melt season (January-March) due to the thawing of previously frozen landscapes and increased snow melt, with only a minor increases in potential evaporation during these months of relatively low net radiation. However, later in the melt season (April-August), SM may decrease dramatically, as snow melt is exhausted earlier and evaporative demand increases greatly due to the non-linearity of the Clausius-Clapeyron relationship (Blankinship et al. 2014, Barnett et al. 2005). This framework for understanding seasonal SM changes is complicated by uncertainties in future precipitation (P) projections, as GCMs disagree on the sign of future P changes over California (Das et al.

2013, Neelin et al. 2013, Berg et al. 2015). Future *P* decreases would certainly exacerbate warming-driven SM losses, though even additional *P* may not prevent spring/summer SM drying given strong warming-driven reductions in snowpack and advances in runoff timing.

Using output from global climate models (GCMs) in the Coupled Model Intercomparison Project Phase 5 (CMIP5, Taylor et al. 2012), several studies have examined the response of SM to rising greenhouse gas concentrations in the 21st century. Analyzing output from 11 CMIP5 GCMs, Dai (2013) found strong model agreement that end-of-21st-century (2080–2099) annual surface (upper 10cm) SM over California is projected to decrease around 10% under the Representative Concentration Pathway 4.5 (RCP4.5) forcing scenario compared to 1980–1999. Similarly, in an analysis of end-of-21st-century projections from 32 CMIP5 GCMs under the RCP8.5 forcing scenario, Collins et al. (2013, Figure 12.23) found robust and significant annual mean surface SM declines of about 1-2 mm over California; these declines are consistent with large-scale regional warming and are expected to increase the risk of agricultural drought.

Seager et al. (2013) expanded on previous assessments of future annual-mean SM by exploring future SM changes, which are important because much of the Sierra Nevada's water storage relies on inflows from winter *P*, but crops depend on summertime SM. Focusing on near future (2021–2040) projections from 16 CMIP5 GCMs under RCP8.5 over California and Nevada, Seager et al. (2013) found winter (JFM) ensemble-mean *P* increases (with little change in ensemble median *P*), which, together with warming-driven JFM evaporation (*E*) increases, has little net effect on JFM SM, runoff and *P* minus *E*. However, in the other seasons, Seager et al. found most GCMs have both decreasing *P* and increasing *E*, which cause spring and summer declines in both runoff and SM. Lastly, Seneviratne et al. (2013) examined end-of-21st-century regional responses of SM as projected by five Earth System Models in the Global Land-

Atmosphere Climate Experiment - Coupled Model Intercomparison Project Phase 5 (GLACE-CMIP5) experiment under RCP8.5. The authors found strong model agreement in declining summertime (JJA) SM of 5-15% over the much of Southwestern United States (including parts of California), attributed to projected mean changes in JJA *P* and *E*.

While GCMs offer insight into future SM changes under various emissions scenarios, their coarse resolution prevents the adequate representation of the complex topography of the Sierra Nevada and the associated orographic processes. GCMs may miss orographic precipitation, temperature (*T*) variations due to snow-albedo-feedback (which influence ET fluxes) and snowpack structure, all of which influence SM and its spatial distribution in the Sierra Nevada. So, downscaling methods are often used to regionalize GCM climate change signals to much higher spatial resolutions (Giorgi et al. 1994, Snyder et al. 2002, Timbal et al. 2003, Hayhoe et al. 2004, Leung et al. 2004, Tebaldi et al. 2005, Duffy et al. 2006, Cabré et al. 2010, Salathé et al. 2010, Pierce et al. 2013).

Downscaling is typically done either statistically (using empirical relationships) or dynamically (using a regional climate model). Statistical downscaling has aided previous studies of climate change impacts to SM and surface hydrology. Its low computational cost allows statistical downscaling to be quickly applied to many GCMs and forcing scenarios (Pierce and Cayan 2013). However, statistical methods may miss key processes such as snow albedo feedback (Walton et al. 2016) and may show substantially reduced accuracy when applied to a warmer climate (Gutierrez et al. 2013). In a study of future SM over the Southwest United States, Cayan et al. (2010) employed a widely-used statistical downscaling technique, bias corrected constructed analogues (BCCA; Hidalgo et al. 2008, Maurer and Hidalgo 2008) to regionalize *T* and *P* output from two GCMs from the Coupled Model Intercomparison Project

Phase 3 (CMIP3). Statistically downscaled *T* and *P* were used to force the Variable Infiltration Capacity (VIC) hydrological model, and Cayan et al. found increased future aridity and drought severity associated with rising summertime *T* in the Southwest United States. Christensen and Lettenmaier (2007) used another common statistical downscaling technique, Bias Correction with Spatial Disaggregation (BCSD; Wood et al. 2002; Wood et al. 2004), to downscale *T* and *P* output from 11 CMIP3 GCMs for the Colorado River Basin, and then used the downscaled climate scenarios to force VIC. Nearly all of the statistically downscaled scenarios projected annual SM declines around 10% by the end-of-21st-century under the most aggressive warming scenario ("A2 emissions scenario") that the authors considered.

Dynamical downscaling using a regional climate model is another way to regionalize GCM climate change signals. Dynamical downscaling directly simulates complex fine-scale physical processes, like orographic precipitation, snowpack accumulation and melt, and runoff. Having more physically realistic simulation of these key inputs should improve modeling of SM in the Sierra Nevada. Running a regional climate model is often very computationally expensive, so dynamical downscaling studies are usually limited to only one or two downscaled GCMs. For example, Sato et al. (2007) used the Terrestrial Environment Research Center Regional Atmospheric Modeling System (TERC-RAMS) to dynamically downscale one GCM under the A2 emissions scenario over Mongolia. They found July SM declines of around 5% due to decreased *P* and warming-driven PET increases, suggesting the frequency of severe droughts may increase due to climate change. Over the greater Los Angeles region, Schwartz et al. (2016a) dynamically downscaled five CMIP5 GCMs using the Weather Research and Forecasting model (WRF), and found that future warming causes soils to dry earlier in the year, but with no change in annual SM due to available water limitations in the semi-arid

Mediterranean-type climate regime. Thus, previous studies, which employ both dynamical and statistical downscaling techniques, demonstrate that the response of SM to climate change is both regional-specific and sensitive to the magnitude and phasing of *T* and *P* changes.

Perhaps due to the computational demands of regional climate models, there has been no dynamically downscaled-based CMIP5 analysis of 21st century SM changes over the California Sierra Nevada (to our knowledge). The goal of this paper is to provide a high-resolution multi-model examination of end-of-21st-century SM changes over the Sierra Nevada. This study uses a hybrid dynamical-statistical downscaling approach pioneered by Walton et al. (2015). Under this approach, a handful of GCMs are downscaled dynamically, then the dynamical results are extended to a full ensemble of GCMs using a statistical model. This approach allows us to produce results with the physical realism of dynamical downscaling for an entire ensemble of GCMs, without the high computational cost of dynamically downscaling each one.

Here is a brief overview of our study. First, five CMIP5 GCMs are dynamically downscaled (sections 4.2-4.3). Then, output from the dynamical simulations is used to build a statistical model for SM (section 4.4). In section 4.5, we use the statistical model to project end-of-21st-century SM for all available CMIP5 models for all future emissions scenarios examined in the IPCC Fifth Assessment Report (van Vuuren et al. 2011). This allows for the quantification of ensemble-mean future SM changes in the Sierra Nevada, along with the associated uncertainty due to inter-model spread and emissions scenarios. Finally, sections 4.6 and 4.7 discuss the study's results and limitations, along with a summary the major findings and their implications. This study is part of a larger project that includes separate downscaling-based assessments of the CMIP5 ensemble's end-of-21st-century projections for temperature (Walton et al. 2016), snowpack (Sun et al. 2016b) and surface runoff timing (Schwartz et al. 2016b) over the Sierra

Nevada. Collectively, these studies offer a high-resolution picture of future regional hydroclimate.

4.2 Dynamical downscaling framework and evaluation

4.2.1 Dynamical downscaling framework

The dynamically downscaling simulations used in this study are the same as that employed in Walton et al. (2016), Sun et al. (2016) and Schwartz et al. (2016b). The text in section 4.2.1 is derived from Schwartz et al. (2016b) with minor modifications. Dynamical downscaling is performed using the Weather Research and Forecasting (WRF) model version 3.5 (Skamarock et al. 2008). WRF is coupled to the community Noah land surface model with multi-parameterization options (Noah-MP, Niu et al. 2011). Three one-way nested domains are used to represent the intense topography of the Sierra Nevada as accurately as possible (Fig. 4.1a). The outermost domain (not shown) spans the U.S. West Coast and adjacent Pacific Ocean at 27 km horizontal resolution. The middle domain (D2), at 9 km resolution, covers all of California. Finally, the innermost domain (D3), at 3 km resolution, spans the eastern edges of the Sacramento and San Joaquin Valleys to the leeside of the California Sierra Nevada Mountains (Fig. 4.1b); this domain is the focus of this study. As the emphasis of this study is 0-10cm SM, we exclude lake, reservoir and urban locations in our analysis.

WRF parameterization testing has been done to improve the simulation of hydroclimate, with a focus on Sierra Nevada snowpack and streamflow. The suite of physical parameterizations includes the New Thompson microphysics scheme (Thompson et al. 2008), Dudhia shortwave radiation scheme (Dudhia 1989), Rapid Radiative Transfer Model longwave (RRTM) longwave radiation scheme (Mlawer et al. 1997), MYNN Level 2.5 surface/boundary layer scheme (Nakanishi and Niino 2006), and Old Kain-Fritsch cumulus convection scheme (Kain and Fritsch 1990). Spectral nudging of temperature, zonal and meridional winds, and geopotential height above the boundary layer is employed over the outermost domain.

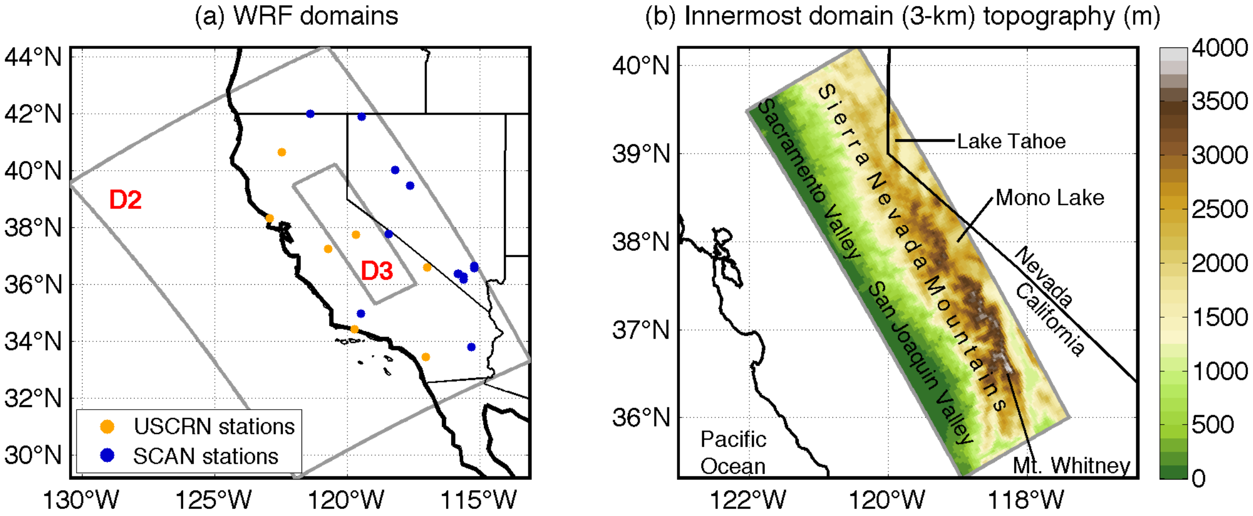

Fig. 4.1: (a) Model setup, showing the two innermost nested domains: D2 (9 km horizontal resolution) and D3 (3 km horizontal resolution). Circles show the locations of 7 NOAA U.S. Climate Reference Network (USCRN) stations (orange) and 13 USDA Soil Climate Analysis Network (SCAN) stations (blue) used for model evaluation. (b) Topography (m) of the innermost domain (3-km resolution) of the regional simulation, with the state borders of California and Nevada in black.

Climate changes signals are produced from a single baseline simulation and five future simulations. The baseline simulation spans October 1991 to September 2001 (water years 1992–2001; hereinafter “WY 1992–2001”) and is a dynamical downscaling of the National Centers for Environmental Prediction’s 6-hourly North America Regional Reanalysis (NARR; Mesinger et al. 2006). NARR is a relatively coarse-resolution (32 km) reanalysis dataset that provides the lateral boundary forcings and initial conditions for the outermost WRF domain in Fig. 4.1a. The baseline simulation allows us to assess the model’s ability to simulate regional SM through comparison to available observations (Section 4.2.2) and serves as a climate state against which we can compare future climate simulations to quantify change.

Using the same model configuration as the baseline, we perform a five-member ensemble of dynamical downscaling experiments to simulate end-of-21st-century climate. The future simulations span October 2091 to September 2101 (water years 2092–2101, hereinafter "WY 2092–2101"). We dynamically downscale GCM experiments forced by the Representative Concentration Pathway 8.5 (RCP8.5) forcing scenario (Van Vuuren et al. 2011) for five CMIP5 GCMs: CNRM-CM5, GFDL-CM3, INM-CM4, IPSL-CM5A-LR, and MPI-ESM-LR. Out of all available GCMs forced by RCP8.5, this five-member ensemble approximately spans the range of end-of-21st-century near-surface T and P changes over California (Walton et al. 2016, Fig. 2).

To produce boundary conditions for the future WRF simulations, we add a perturbation reflecting the mean change in GCM climatology to NARR data for WY 1992–2001, following the "pseudo-global warming" (PGW) method (Schar et al. 1996, Hara et al. 2008, Kawase et al. 2009, and Rasmussen et al. 2011). This method allows us to assess how WY 1992–2001 would transpire if the mean climate were altered to reflect climate changes projected by each of the five selected GCMs. We first quantify differences in GCM monthly climatology between the historical and end-of-21st-century RCP8.5 experiments (2081–2100 average minus 1981–2000 average) for temperature, humidity, zonal and meridional winds, and geopotential height. Then, for each of the five selected GCMs, we perturb the baseline 6-hourly NARR reanalysis data for each month by adding the corresponding monthly mean climatological change. The perturbed NARR fields then serve as WRF boundary conditions for the five future simulations.

This approach allows us to quantify how GCM climate change signals are expressed at the regional scale, without the future simulations being subject to significant mean state biases often found in GCMs. For additional information on the dynamically downscaled simulations, the reader is referred to Walton et al. (2016).

4.2.2 Model evaluation

We evaluate WRF's ability to simulate historical spatial and temporal SM variability by comparing simulated surface (0-10cm) SM to available observational data. Due to the scarcity in long-term, large-scale SM observations (Robock et al. 2000; Seneviratne et al. 2013), there are unfortunately limited in situ SM observations within this study's focus domain (Fig. 4.1b) during the baseline period (WY 1992–2001). In an effort to assess both climatological SM and its interannual variability, our evaluation of WRF-simulated SM focuses on the 9-km resolution domain (D2 in Fig. 4.1a) of the regional downscaling simulation, and we extend the historical simulation for D2 to span WY 1992-2015. Using a larger domain and longer time period for this evaluation exercise provides a greater number of SM observations to compare with WRF-simulated SM.

In situ SM observations were obtained from two observational networks: the U.S. Department of Agriculture's National Soil Survey Center's Soil Climate Analysis Network (SCAN; Schaefer et al. 2007, http://www.wcc.nrcs.usda.gov) and the National Oceanic and Atmospheric Administration's U.S. Climate Reference Network (USCRN; Leduc et al. 2009, http://www.ncdc.noaa.gov/crn/). SCAN provides daily fractional SM (m^3/m^3) data at a depth of 4 inches (~10.16cm), and USCRN provides daily SM at a depth of 10 cm. After obtaining data from all stations within the 9-km resolution domain with some daily SM data over WY 1992-2015, daily SM observations were averaged to produce a time series of monthly average SM.

Months with more than seven missing days of data are not used for this evaluation exercise. Additionally, to assess both climatological SM and its interannual variability, we include only stations with at least three years of data. Thirteen SCAN stations and seven USCRN stations meet these criteria, and their locations are shown in Fig. 4.1a by blue and orange circles, respectively.

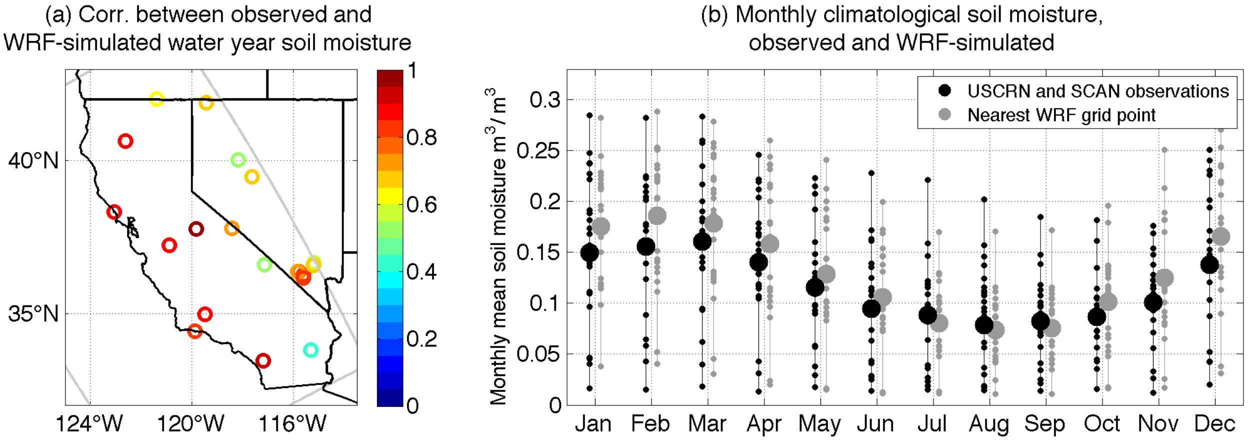

Fig. 4.2: Evaluation of the dynamical downscaling framework's ability to simulate soil moisture compared to available in situ observations from stations in the National Oceanic and Atmospheric Administration's U.S. Climate Reference Network (USCRN) and the U.S. Department of Agriculture's National Soil Survey Center's Soil Climate Analysis Network (SCAN). In situ observations are compared to WRF output at the nearest grid point in the 9-km domain over water years 1992-2015. (a) Correlation coefficients of annual mean soil moisture between observational stations and the nearest grid point in the 9-km WRF output. (b) Comparison of observed and WRF-simulated monthly climatological soil moisture at observational stations (black) and the nearest grid point in the 9-km WRF output (gray). Large circles represent station-averages, and small circles represent individual stations.

In Fig. 4.2a, we correlate available mean water year SM observations with that simulated at the nearest WRF grid point in the 9-km output over WY 1992-2015. Correlations greater than $r = 0.50$ are found across all but one stations, with 16 stations having correlations above $r = 0.60$. Very high correlations ($r > 0.80$) are found throughout coastal stations and in the stations close to the Sierra Nevada. Stations with relatively low correlations are generally in extremely dry desert regions (where SM has little interannual variability). Overall, the interannual variability in SM observed at SCAN and USCRN stations throughout California and neighboring state is reproduced by WRF reasonably well.

Fig. 4.2b compares monthly climatological SM for SCAN and USCRN stations (black) with that simulated by the nearest grid point in the 9 km WRF domain (gray), where large circles show the station-average climatological monthly SM and small circles represent the 20 stations. WRF's simulation of the annual SM cycle is consistent compared to observation, with station-average correlation r = 0.78 and station-average root mean squared error in monthly climatological SM values of 0.031 m^3/m^3. WRF reasonably simulates both the magnitude and phasing of monthly SM, where soils are relatively moist December through April, and dry the remaining months. The seasonality of SM in the domain of interest stems from the region's distinct wet/cool (October-March) and dry/warm (April-September) seasons. Wet-season P and spring snowmelt moisten surface soils November-May, but spring/summer evapotranspiration deplete SM until it reaches its September minimum. Overall, Fig. 4.2b indicates WRF is able to simulate seasonal variations in SM reasonably well across the domain.

We note that prior studies have evaluated the realism of the spatial and temporal patterns in temperature and snow cover (Walton et al. 2016), snow water equivalent (Sun et al. 2016), and surface runoff timing (Schwartz et al. 2016b) for these dynamically downscaled simulations. Overall, Fig. 4.2 and the aforementioned studies demonstrate that this WRF framework simulates SM variability during the historical period with reasonable accuracy where reliable observational data are available; this give us confidence that our dynamical downscaling framework is likely to be able to reproduce spatial, seasonal and interannual SM variations throughout the Sierra Nevada.

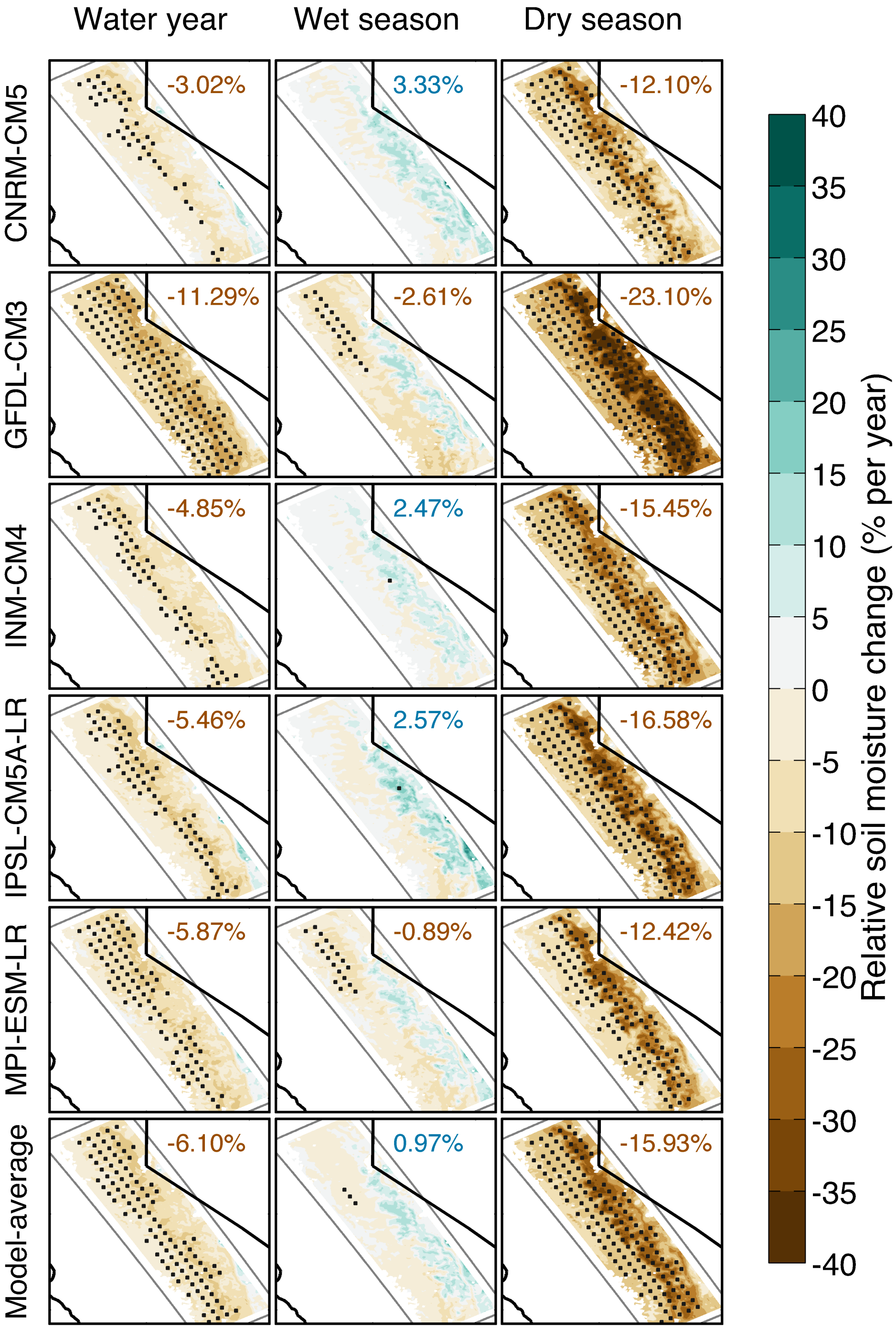

Fig. 4.3: End-of-21st century relative change in 0–10cm soil moisture (unit: % per year) averaged over the water year (October–September, left column), wet season (October–March, center column) and dry season (April–September, right column) under the RCP8.5 forcing scenario according to the five dynamically downscaled models (rows 1-5) and the model-average (row 6). Stippling indicates statistical significance at the 95% level using a two-tailed Student's t-test. Domain-averages are reported in the upper right inset of each panel, with brown text denoting domain-average 0–10cm soil moisture drying and blue text denoting domain-average 0–10cm soil moisture moistening.

4.3 Dynamically downscaled end-of-21st-century SM changes under RCP8.5

4.3.1 Water year and seasonal soil moisture changes

Fig. 4.3 presents the dynamically downscaled end-of-21st-century (WY 2092–2101) fractional change (unit: %/year) in surface (upper 10cm) SM relative to the baseline (WY 1992–2001) under the RCP8.5 emissions scenario for five GCMs (CNRM-CM5, GFDL-CM3, INM-CM4, IPSL-CM5A-LR, and MPI-ESM-LR) and the five-model ensemble mean (bottom row). Results are shown for the 3-km resolution domain (D3 in Fig. 4.1a). Soil moisture changes (ΔSM) are shown for the "water year" (October-September, left column), "wet season" (October-March, center column) and "dry season" (April-September, right column). Separation of the water year into the "wet season" and "dry season" is based on California receiving most of its precipitation October-March, as discussed in Section 4.2.2 and Cayan and Roads (1984). Stippling indicates locations where end-of-21st-century ΔSM is statistically significant at the 95% level using a two-tailed Student's t-test.

Domain averages are noted in the upper right of each panel, showing that spatially averaged water-year SM changes range between -4.85% to -11.29%, with a model-mean of -6.10%. Although this indicates some model uncertainly regarding the magnitude of the water-year ΔSM (hereinafter ΔSM_{water_year}), a similar spatial pattern emerges in each of the five dynamically downscaled GCMs. For each GCM, ΔSM_{water_year} are greatest and significant (as indicated by cross-hatching) along the western slopes of the Sierra Nevada at elevations between 1750-2500m. These regions, which are near the baseline snow line, have the strongest warming enhancement due to snow albedo feedback (Walton et al. 2016), greatest April 1st snow water equivalent (SWE) loss (Sun et al. 2016b) and largest advances in surface runoff timing (Schwartz et al. 2016b). SM_{water_year} declines are relatively weaker and/or not significant in the low-lying eastern edges of the Sacramento and San Joaquin Valleys, along the southeastern Sierra Nevada, and at the highest elevations in the Southern Sierra Nevada.

Important differences are evident between wet season changes (Fig. 4.3, center column) and dry season (Fig. 4.3, right column). For all GCMs, wet season SM changes (hereinafter "ΔSM_{wet_ssn}") across the domain are generally weakly negative or weakly positive, and most are not statistically significant. The model-average spatial-average is quite small (0.97%), and this near-zero change largely reflects the cancellation of weak SM increases (0 to +5%) at the highest elevations in the Sierras and weak SM decreases (0 to -5%) in the Central Valley and Western Sierra.

Conversely, dry season (April-September) SM changes (hereinafter "ΔSM_{dry_ssn}") are robustly and significantly negative throughout most of the domain for all five downscaled GCMs, with an ensemble-mean spatial average of -15.9% by end-of-21st-century. Spatial patterns in ΔSM_{dry_ssn} are quite similar to those described above for the water year. We note that nearly all robust and statistically significant soil moisture changes are negative, which corroborates previous global-scale studies of future soil moisture that have found that robust soil moisture changes are generally decreases (Collins et al. 2013), despite robust precipitation increases in some locations. Given the robust and statistically significant SM_{dry_ssn} declines projected in each of the dynamical downscaling simulation, a key focus of this study is to understand the drivers leading to such drying, as well as the inter-model spread in SM_{dry_ssn} declines.

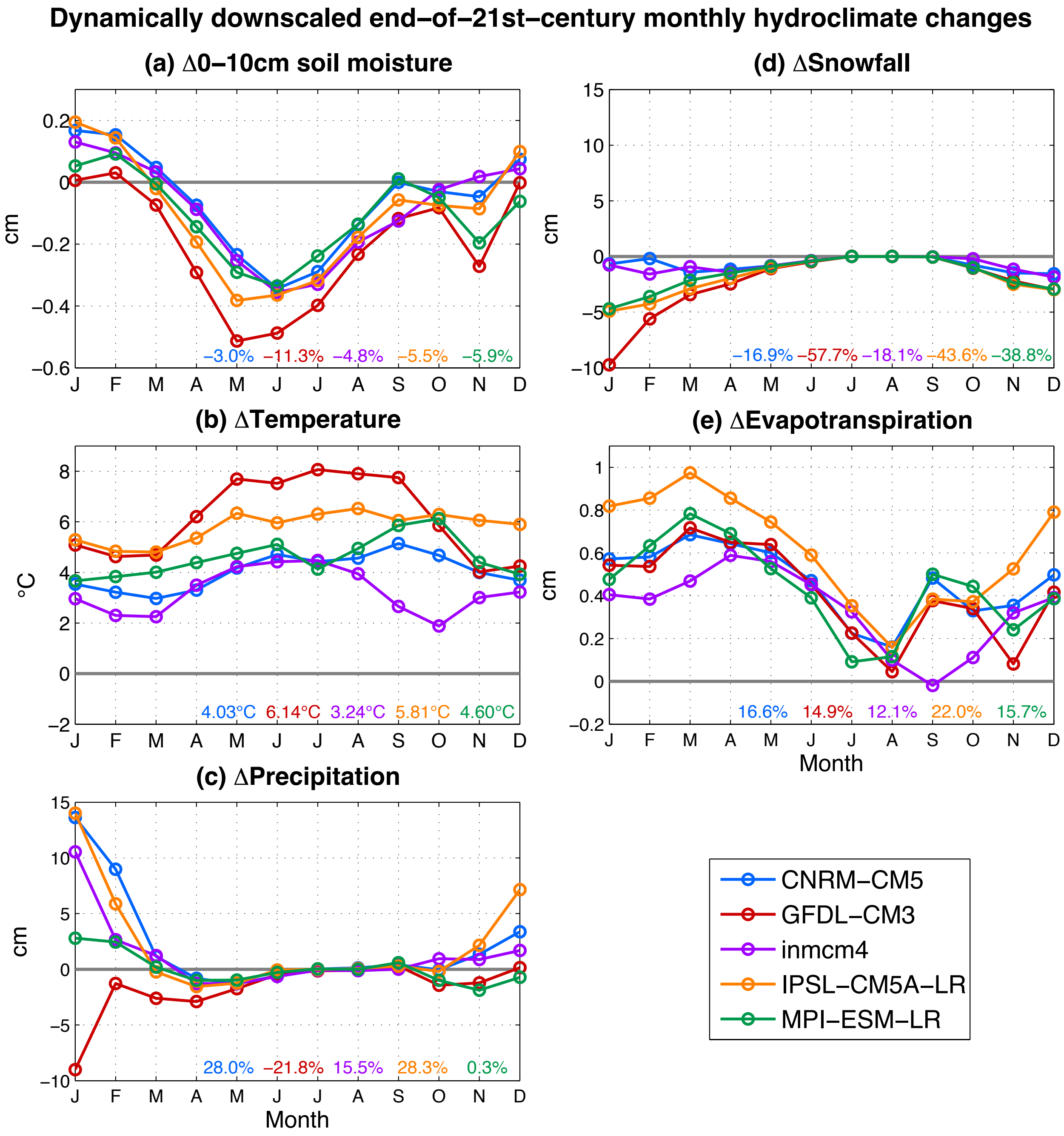

Fig. 4.4: WRF dynamically-downscaled end-of-21^{st}-century monthly (January-December) absolute changes (WY 2092–2102 average minus WY 1992–2001 average) in (a) 0–10cm soil moisture, (b) 2-m air temperature, (c) precipitation, (d) snow and (e) evapotranspiration. Changes reflect averages over the domain (Fig. 4.1b) for the five dynamically-downscaled global climate models: CNRM-CM5 (blue), GFDL-CM3 (red), inmcm4 (purple), IPSL-CM5A-LR (orange) and MPI-ESM-LR (green). Annual mean relative changes (unit: % per year) are reported in the bottom right inset for each global climate model in (a) and (c-e). Annual mean absolute warming (unit: °C per year) is reported in (b). The line y=0 is shown in black.

4.3.2 Drivers of dry-season soil moisture declines

We now aim to understand the causes behind end-of-21st-century dry season (April-September) upper 10cm SM (SM_{dry_ssn}) declines projected throughout the domain in each of the dynamically downscaled GCM simulations (Fig. 4.3, right column). Fig. 4.4 presents end-of-21st-century monthly (January-December) absolute changes (future minus baseline) in key hydroclimate variables: (a) upper 10cm SM, (b) T, (c) P, (d) snow and (e) evapotranspiration (ET). Monthly changes are presented as domain-averages. In Fig. 4.4a and c-e, annual mean relative changes (unit: % per year) are reported in the bottom right inset of each panel for each GCM. In Fig. 4.4b, annual mean absolute warming (unit: °C per year) is reported.

Fig. 4.4a shows robust declines in SM_{dry_ssn}, which are slightly offset by small (but insignificant) wintertime increases. The strong spatial and temporal inter-model agreement in ΔSM_{dry_ssn} seen in Figs. 4.4 and 4.5a – despite large uncertainty in the sign and magnitude of October-May ΔP (Fig. 4.4c) – suggests a common driver of SM_{dry_ssn} declines for each downscaled GCM.

The mechanism behind SM_{dry_ssn} declines is rooted in the impact of near surface (2-meter) warming (Fig. 4.4b) on the region's snow-dominated hydroclimate. For each of the five dynamically downscaled GCMs (even those with projected annual P increases), warming reduces snow (Fig. 4.4d) by decreasing the fraction of P that falls as snow and through enhanced snowpack melting. (For a comprehensive analysis of end-of-21st-century snowpack changes in the Sierra Nevada, we direct the reader to Sun et al. 2016b.) Snowpack changes create a new pool of liquid water that slightly moistens winter soils (Fig. 4.4a) and advances surface runoff timing (Schwartz et al. 2016b). This available liquid moisture, together with significant warming

(Fig. 4.4b) enhances *ET* rates (Fig. 4.4e). Enhanced *ET* significantly dries spring and summer soils, in spite of any increase in wintertime *P*.

To understand how this warming mechanism acts on each GCM, we examine dynamically downscaled *T* (Fig. 4.4b) and *P* (Fig. 4.4c) changes. Of the five dynamically downscaled GCMs, GFDL-CM3 has the greatest end-of-21st-century SM_{dry_ssn} decline, with domain-average change of -23.10% (Fig. 4.3). This can be explained through GFDL-CM3's unique decrease in annual *P* (domain average -20.4 cm/yr or -22%, Fig. 4.4c red), which slightly reduces wet season SM (domain average -2.61%). Decreasing *P*, coupled with strong domain-average annual ΔT of +6.14 °C (Fig. 4.4b, red) that enhances annual ET by +15% (Fig. 4.4e), shed light on GFDL-CM3's dramatic loss of SM_{dry_ssn}.

Interestingly, projected ΔT in IPSL-CM5A-LR (domain average 5.81 °C) is nearly as much as in GFDL-CM3, but it is associated with the largest annual *P* increase (28.3%) in this 5-model ensemble. However, this additional *P* falls more so as rain instead of snow (domain-average change in snowfall of -43.6%, Fig. 4.4d orange); this shift results in the moistening of SM_{wet_ssn} at some high-elevation locations by as much as 20% (Fig. 4.3) and dramatic advances in surface runoff timing (Schwartz et al. 2016b). Warming acts on the new pools of liquid surface water by enhancing *ET* (Fig. 4.4e orange), but the net effect of SM_{dry_ssn} declines in IPSL-CM5A-LR (-16.58%) is weaker than that in GFDL-CM3 (-23.10%) due to their divergent signs of ΔP.

CNRM-CM5 (Fig. 4.4, blue) and inmcm4 (Fig. 4.4, purple) behave very similarly to IPSL-CM5A-LR, but their dry season soils dry to a lesser degree (-12.10% and -15.45%, respectively) because they project roughly one third less warming. Relatively modest annual warming of CNRM-CM5 (+4.03 °C) and inmcm4 (+3.24 °C) compared to IPSL-CM5A-LR has the effect of buffering snow loss by a factor of around 2.5 (-16.9% and -18.1%, respectively, compared to -43.6%). This buffering limits the formation of available water for evaporative demands, which explains CNRM-CM5 and inmcm4's small ΔET compared to IPSL-CM5A-LR (Fig. 4.4e). This weaker ET increase provides for less overall SM loss for CNRM-CM5 and inmcm4. Despite its near-zero change in annual *P* (domain average +0.3%), MPI-ESM-LR's strong warming (+4.60 °C) (and the associated 38.8% loss of snowfall) allows ET to increase nearly as much as in CNRM-CM5, shedding light on the similar domain-average SM$_{dry\_ssn}$ declines in these models.

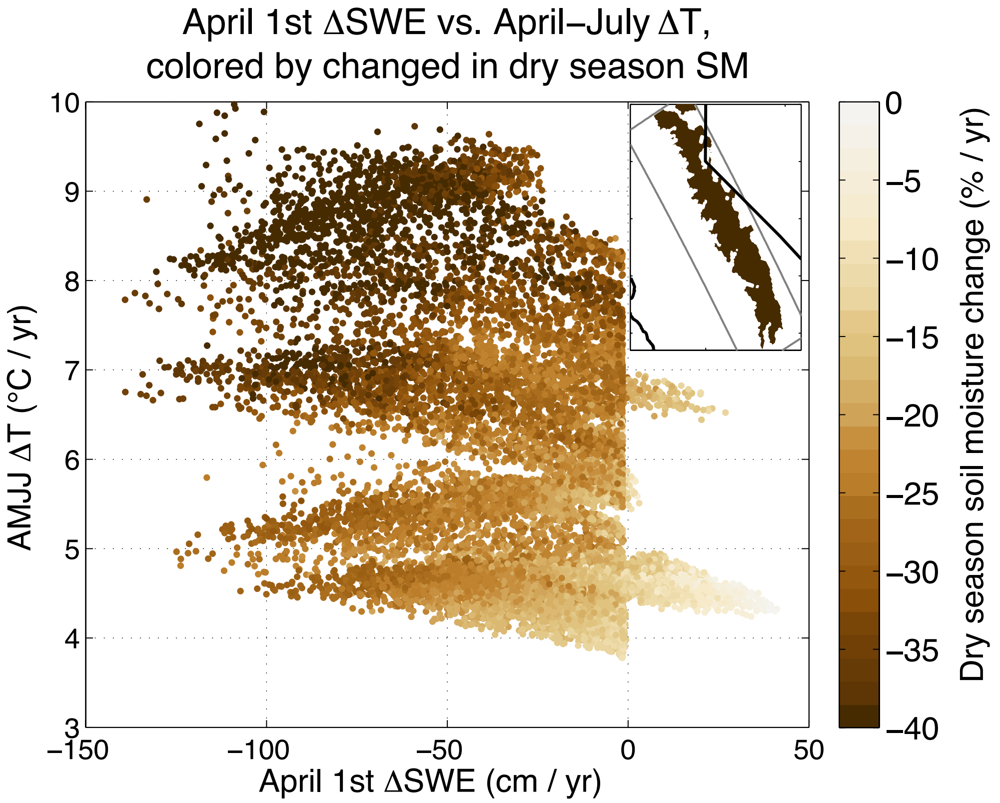

Fig. 4.5: Scatterplot of five-model dynamically downscaled end-of-21st-century RCP8.5 absolute change in April 1st snow water equivalent (SWE, unit: cm per year) versus mean end-of-21st-century change in 2-m temperature averaged over April–July (unit: °C per year). Colors indicate the relative change in dry-season (April–September) 0–10 cm soil moisture (unit: % per year). Results are shown for grid points with greater than 1.5cm of baseline climatological April 1st SWE; this region is highlighted in brown in the top right inlay.

Fig. 4.5 corroborates the influences of ΔP and ΔT on declining SM_{dry_ssn}. Fig. 4.5 presents a scatter plot of end-of-21st-century April 1st snow water equivalent change ($\Delta\mathrm{SWE}_{April\_1st}$, unit: cm per year) vs. near-surface April–July warming (ΔT_{AMJJ}, unit: °C per year), colored by fractional $\Delta\mathrm{SM}_{dry\_ssn}$ (unit: % per year). Results are shown for the five dynamically downscaled GCMs at all grid points with greater than 1.5cm of baseline climatological SWE_{April_1st} (this region is highlighted in the top right inlay).

Several relationships can be gleaned from this scatter plot. First, there is a positive relationship ($r = 0.73$) between spatial patterns of $\Delta\mathrm{SWE}_{April\_1st}$ and $\Delta\mathrm{SM}_{dry\_ssn}$. This relationship emerges because $\Delta\mathrm{SWE}_{April\_1st}$ is a measure of the amount of moisture available to increase SM_{dry_ssn} (through snowpack melting). Thus, grid points with large losses of SWE_{April_1st} also have strong SM_{dry_ssn} declines. Second, there is a negative relationship ($r = -0.71$) between $\Delta\mathrm{SWE}_{April\_1st}$ and ΔT_{AMJJ}, as ΔT_{AMJJ} is a rough measure of the extra energy available to enhance ET, which serves to decrease SM_{dry_ssn}. Thus, for a given change in SWE_{April_1st}, the magnitude of SM_{dry_ssn} drying increases with stronger ΔT_{AMJJ}.

The relationships gleaned from Fig. 4.5 suggest $\Delta\mathrm{SWE}_{April\_1st}$ and ΔT_{AMJJ} might be reasonable co-predictors for dry season $\Delta\mathrm{SM}_{dry\_ssn}$, which will be explored in section 4.4. Fig. 4.5 demonstrates that despite any wintertime P (and SM) increases, thermodynamically induced impacts of diminished snowpack and elevated ET conspire to produce statistically significant spring and summertime SM drying. Overall, Figs. 4.5-4.6 provide evidence that anthropogenic warming (through both its effects on decreasing SWE_{April_1st} and enhancing ET) will fundamentally transform Sierra Nevada hydrology by the end-of-21st-century.

4.4 Hybrid dynamical-statistical soil moisture model

Results in section 4.3.1 focused only on end-of-21st-century SM_{dry_ssn} projections under the RCP8.5 emissions scenario for five selected GCMs, highlighting spatial patterns in ΔSM_{dry_ssn} and the relationships between ΔSM_{dry_ssn}, ΔSWE_{April_1st} and ΔT_{AMJJ}. These results, however, do not offer adequate information to comprehensively evaluate uncertainty in ΔSM_{dry_ssn} due to forcing scenario or intermodel spread. In this section, we develop a computationally efficient yet physically sound model to project SM_{dry_ssn} for all available CMIP5 GCMs and all forcing scenarios. Section 4.3.1 describes this model, and section 4.3.2 provides an evaluation of its ability to mimic dynamical SM_{dry_ssn} projections presented in section 4.3.1.

Section 4.3.2 discussed the positive relationship between ΔSM_{dry_ssn} and ΔSWE_{April_1st} and negative relationship between ΔSM_{dry_ssn} and ΔT_{AMJJ} in the dynamical simulations. Thus, ΔSWE_{April_1st} and ΔT_{AMJJ} are credible co-predictors for ΔSM_{dry_ssn}; these co-predictors are also physically-sensible as the former is a measure of snowpack available to increase SM_{dry_ssn} as it melts, and the latter quantifies the degree to which warming can decrease SM_{dry_ssn} through enhanced ET. Given these relationships, we seek to construct a modeling framework that projects ΔSM_{dry_ssn} given ΔSWE_{April_1st} and ΔT_{AMJJ}. This modeling framework, in which relationships from dynamically downscaled GCM output are exploited to design a statistical model (that can then downscale projections for other GCMs in the CMIP5 ensemble), is an example of hybrid dynamical-statistical downscaling. This computationally-efficient technique is a valuable tool for ensemble projections of future hydroclimate because it captures patterns and physical processes that may emerge only through dynamical downscaling (Walton et al. 2015, Sun et al. 2016a).

4.4.1 Hybrid model description

For each grid point in the 3 km resolution domain, we use multiple linear regression to determine how ΔSM_{dry_ssn} depends on ΔSWE_{April_1st} and ΔT_{AMJJ}. In order to create a more robust model, data at that grid point *and* its eight neighboring grid points is used. In all, 45 data points (5 models × 9 grid points) are used to model ΔSM_{dry_ssn} at a given location. Multiple linear regression produces the following equation:

$$(1) \qquad \Delta SM_{dry\_ssn,\, GCM,i,j} \cong \alpha_{i,j} * \text{April } 1^{st}\ \Delta SWE_{GCM,i,j} + \beta_{i,j} * \text{AMJJ } \Delta T_{GCM,i,j}$$

where (i,j) are coordinates of the grid point in the 3 km resolution domain, coefficient α is the linear sensitivity of ΔSM_{dry_ssn} to ΔSWE_{April_1st}, and coefficient β is the linear sensitivity of ΔSM_{dry_ssn} to ΔT_{AMJJ}. We force the linear relationship to have no residual term, which is an expression of the physical constraint that one would not anticipate a change in ΔSM_{dry_ssn} given no change in both ΔSWE_{April_1st} and ΔT_{AMJJ}. Eq. (1) can be used to obtain mean end-of-21st-century fractional ΔSM_{dry_ssn} given ΔSWE_{April_1st} and ΔT_{AMJJ}. At grid points where mean ΔSWE_{April_1st} is 0 cm in all dynamically downscaled GCMs, ΔSM_{dry_ssn} is determined only by the linear regression of dynamically downscaled ΔSM_{dry_ssn} onto ΔT_{AMJJ}. (Section 4.6.1 presents a discussion of regions and elevations where SM_{dry_ssn} changes are driven by loss of SWE_{April_1st} or by enhanced ET due to ΔT_{AMJJ}.)

The goal of the hybrid dynamical-statistical model (Eq. 1) is to project ΔSM_{dry_ssn} given ΔSWE_{April_1st} and ΔT_{AMJJ} . To obtain ΔSM_{dry_ssn} for the full CMIP5 ensemble and all forcing scenarios, we utilize projections of ΔSWE_{April_1st} from Sun et al. (2016b, hereinafter "S2016b") and ΔT_{AMJJ} from Walton et al. (2016, hereinafter "W2016"). S2016b used hybrid dynamical-statistical downscaling (with December-March ΔT and ΔP as predictors) to produce 3-km resolution $\Delta\text{SWE}_{April\_1st}$ for our study domain for all available CMIP5 GCMs and forcing scenarios RCP8.5, 6.0, 4.5 and 2.6. W2016 also used a hybrid downscaling approach that relies on GCM regional-mean ΔT and east-west ΔT contrast as predictors (along with a feedback between ΔT and snow cover change to mimic snow-albedo feedback) to produce 3-km resolution monthly ΔT over the Sierra Nevada for all CMIP5 GCMs and RCPs.

With $\Delta\text{SWE}_{April\_1st}$ from S2016b and ΔT_{AMJJ} from W2016 as input, we are able to apply the hybrid dynamical-statistical $\Delta\text{SM}_{dry\_ssn}$ model (Eq. 1) to all CMIP5 GCMs and forcing scenarios. Before we present hybrid downscaled end-of-21st-century projections of SM_{dry_ssn}, we first evaluate the hybrid model's ability to mimic the dynamical model.

4.4.2 Hybrid model evaluation

Ideally, $\Delta\text{SM}_{dry\_ssn}$ projections would be made by dynamically downscaling all CMIP5 GCMs and forcing scenarios. However, hybrid dynamical-statistical projections are used instead to conserve scarce computational resources. In this section, we evaluate how well our dynamical-statistical projections can approximate dynamical downscaling. There are two primary sources of error in this approximation. The first error stems from our choice to approximate $\Delta\text{SM}_{dry\_ssn}$ as a linear combination of $\Delta\text{SWE}_{April\_1st}$ and ΔT_{AMJJ}. However, we expect this error to be small given the strong linear correlation between $\Delta\text{SM}_{dry\_ssn}$ and $\Delta\text{SWE}_{April\_1st}$ and strong linear anti-correlation between $\Delta\text{SM}_{dry\_ssn}$ and ΔT_{AMJJ}. We can quantify this error for each GCM by projecting $\Delta\text{SM}_{dry\_ssn}$ using Eq. (1) with dynamically downscaled WRF $\Delta\text{SWE}_{April\_1st}$ and ΔT_{AMJJ} under RCP8.5 as input. This statistical $\Delta\text{SM}_{dry\_ssn}$ projection for each GCM is presented in Fig. 4.6 (center column), and can be compared to dynamically downscaled $\Delta\text{SM}_{dry\_ssn}$ (left column).

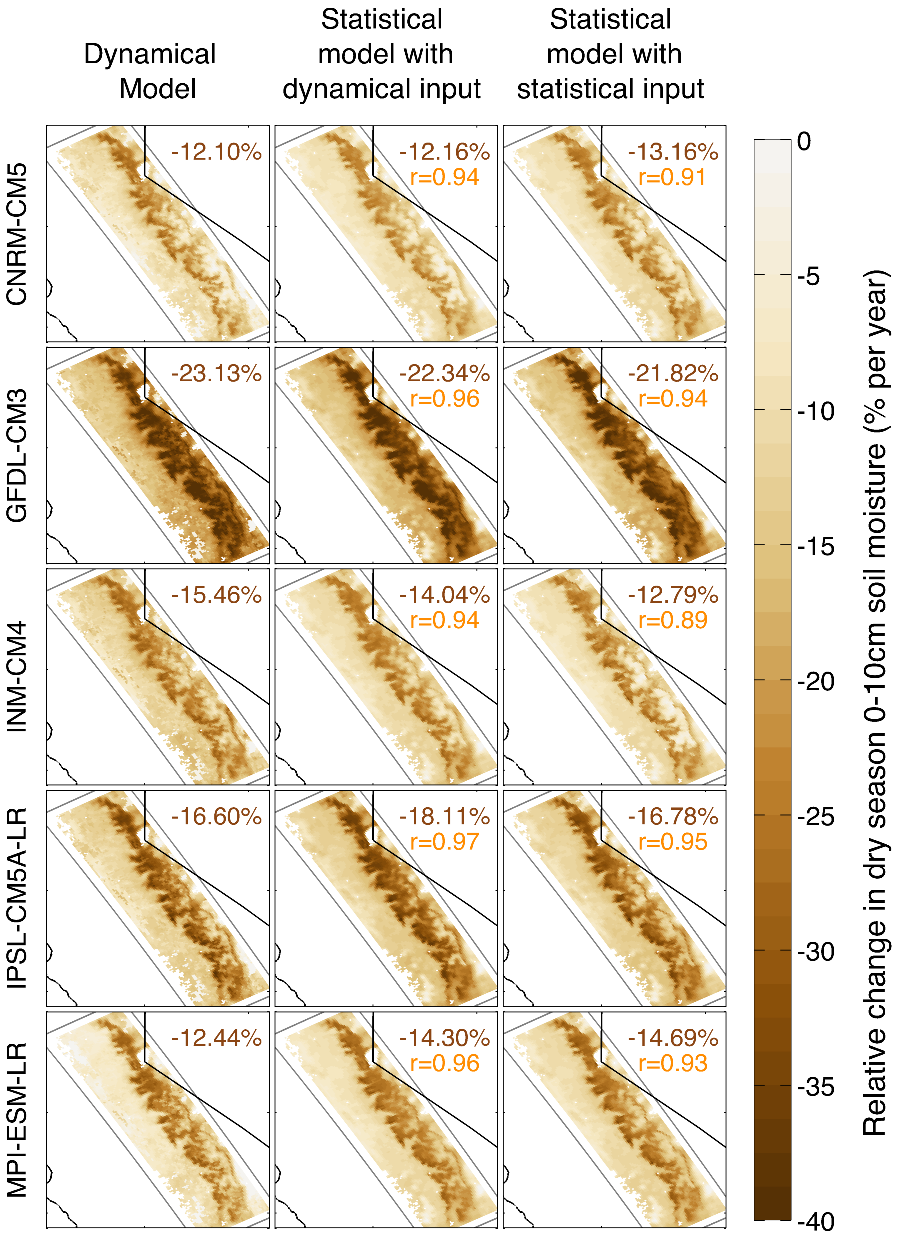

Fig. 4.6: Relative change in end-of-21st-century dry season (April–September) 0–10cm soil moisture under the RCP8.5 emissions scenario for CNRM-CM5, GFDL-CM3, inmcm4, IPSL-CM5A-LR and MPI-ESM-LR produced from three methods. Column 1: Dynamically-downscaled WRF output. Column 2: Statistical projection calculated with WRF dynamically-downscaled changes in April 1st SWE and April–July near-surface warming as input. Column 3: Statistical projection calculated with hybrid dynamical-statistical downscaled change in April 1st SWE (Sun et al. 2016) and April–July near-surface warming (Walton et al. 2016) as input. Results are shown for non-urban land points. Brown text indicates domain-average relative change in dry season soil moisture (unit: % per year); orange text in columns 2-3 indicates the spatial correlation coefficient with column 1.

Spatial patterns of ΔSM_{dry_ssn} approximated with Eq. (1) are highly correlated with their dynamical counterparts ($r > 0.94$). Moreover, the domain-average ΔSM_{dry_ssn} approximated by Eq. (1) is close to those of the dynamical model for each GCM. The ability of the hybrid ΔSM_{dry_ssn} model (Eq. 1) to mimic the dynamical model given perfect ΔSWE_{April_1st} and ΔT_{AMJJ} as input backs our decision to model ΔSM_{dry_ssn} as a linear combination of ΔSWE_{April_1st} and ΔT_{AMJJ}.

The second source of error in projecting ΔSM_{dry_ssn} for all CMIP5 GCMs and forcing scenarios using Eq. (1) arises from the use of S2016b's ΔSWE_{April_1st} and W2016's ΔT_{AMJJ} (described in section 4.4.1) as input. We evaluate this error by comparing ΔSM_{dry_ssn} patterns produced by dynamical downscaling (Fig. 4.7, left column) to those produced using the hybrid dynamical-statistical ΔSM_{dry_ssn} model (Eq. 1) with S2016b's ΔSWE_{April_1st} and W2016's ΔT_{AMJJ} as input; these ΔSM_{dry_ssn} projections are presented in Fig. 4.6 (right column). Though spatial patterns of ΔSM_{dry_ssn} in Fig. 4.6 (right column) are not as highly-correlated with their dynamical counterparts (left column) as the patterns of ΔSM_{dry_ssn} with dynamical input (center column), ΔSM_{dry_ssn} produced with S2016b's ΔSWE_{April_1st} and W2016's ΔT_{AMJJ} is still well correlated with the dynamical output ($r > 0.89$ for all GCMs). Moreover, errors in domain-average ΔSM_{dry_ssn} in Fig. 4.6 (right column) are small and similar to those in Fig. 4.6 (center column), demonstrating that use of S2016b's ΔSWE_{April_1st} and W2016's ΔT_{AMJJ} as input to the hybrid ΔSM_{dry_ssn} model (Eq. 1) does not deteriorate the subsequent ΔSM_{dry_ssn} projection. With S2016b's ΔSWE_{April_1st} and W2016's ΔT_{AMJJ}, we are able to credibly estimate mean changes in SM_{dry_ssn} for any GCM as if it were dynamically downscaled.

We also note that unlike commonly used statistical downscaling methods, both S2016b's ΔSWE_{April_1st} and W2016's ΔT_{AMJJ} include effects of snow albedo feedback (SAF) on warming.

SAF is a crucial component of future climate change in the snow-dominated Sierra Nevada, and has been shown to be critical to the simulation of summertime (June-September) soil moisture over regions with seasonal winter snow cover (Hall et al. 2008).

This evaluation exercise reveals another important finding: WRF's $\Delta\text{SM}_{dry\_ssn}$ patterns can be determined based on only two pieces of information about a GCM: its change in April 1st SWE and April-July near-surface temperature. This statement is powerful because it indicates that we have diagnosed these two parameters as the key predictors for future spring/summertime SM. Testing was done to determine if ΔSWE or ΔT averaged over other months produced a more skillful model than one relying on April 1st ΔSWE and April-July ΔT, but no improvement could be found. Overall, this indicates that changes in SWE_{April_1st} and T_{AMJJ} are the key predictors for $\Delta\text{SM}_{dry\_ssn}$ in the Sierra Nevada, and it is powerful to reduce changes in SM_{dry_ssn} down to a linear combination of two physically-sensible factors.

4.5 Hybrid dynamical-statistical soil moisture projections for full GCM ensemble, all forcing scenarios

Using the hybrid dynamical-statistical $\Delta\text{SM}_{dry\_ssn}$ model (Eq. 1) with S2016b's $\Delta\text{SWE}_{April\_1st}$ and W2016's ΔT_{AMJJ} as input, we can quickly project mean end-of-21st-century $\Delta\text{SM}_{dry\_ssn}$ relative to the end-of-20th-century for all available CMIP5 GCMs under forcing scenarios RCP2.6 (26 GCMs), RCP4.5 (34 GCMs), RCP6.0 (20 GCMs) and RCP8.5 (35 GCMs). Fig. 4.7 presents end-of-21st-century $\Delta\text{SM}_{dry\_ssn}$ projections (unit: % per year) under forcing scenarios RCP2.6, RCP4.5, RCP6.0 and RCP8.5 (columns 1-4) for the GCM ensemble mean (row 2) and 10th and 90th percentiles of the GCM distribution (rows 1 and 3, respectively).

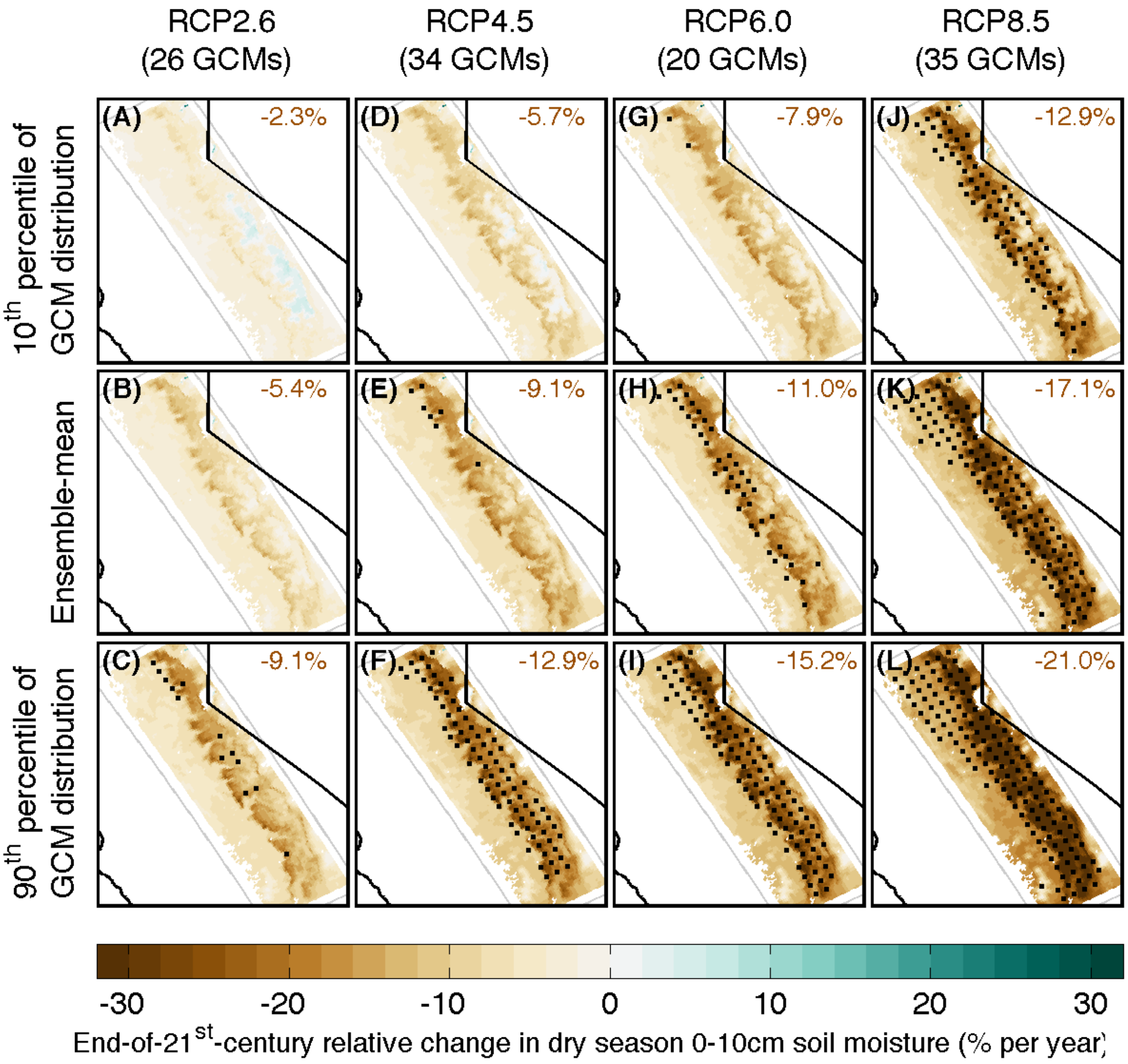

Fig. 4.7: Hybrid dynamical-statistical projections of relative change in end-of-21st-century dry season (April–September) 0–10cm soil moisture under emissions scenarios RCP2.6, RCP4.5, RCP6.0 and RCP8.5. Unit: % per year. Row 2 presents the ensemble-mean change. Rows 1 and 3 present the 10th and 90th percentiles of the GCM distribution, respectively. Brown shading indicates soil drying, while blue shading indicated soil moistening. The number of GCMs included in the ensemble for each RCP is denoted at the top of each column. Brown text in upper right indicates the domain-average relative change in dry season soil moisture at non-urban land points. Black stippling denotes regions where the absolute change in 0-10cm soil moisture is greater than the standard deviation of the baseline (WY 1992–2001) 0-10cm soil moisture.

Black stippling in Fig. 4.7 denotes absolute changes in SM_{dry_ssn} that are greater than one standard deviation of the baseline (WY 1992-2001) SM_{dry_ssn}, which is a measure of interannual variability. Spatial patterns of hybrid downscaled ΔSM_{dry_ssn} are similar for each GCM and RCP combination, with strongest SM_{dry_ssn} declines projected in the northern Sierras and at mid-elevations on the western mountain slopes; these regions are also precisely where April 1st SWE losses are greatest (S2016b) and SAF-amplified warming is greatest (W2016). The magnitude of SM_{dry_ssn} drying expectedly increases with RCP and in GCMs with strong projected warming and SWE_{April_1st} loss.

These ensemble projections allow for the characterization of uncertainty due forcing scenario. Considering that current greenhouse gas emissions already surpass those projected by RCP8.5, this aggressive warming scenario may be the most credible (Peters et al. 2013). If emissions continue to track or exceed those of RCP8.5, the 35-model ensemble-mean projected end-of-21st-century change in domain-average SM_{dry_ssn} is -17.1% (Fig. 4.7k). Moreover, under RCP8.5 it is highly likely that end-of-21st-century spring and summer soils at elevations above 1000m in the Sierra will be dramatically drier than end-of-20th-century. However, if GHG emissions are curtailed such that a mitigation (RCP2.6) or stabilization (RCP4.5) scenario can be achieved, the most-likely (ensemble mean) SM_{dry_ssn} outcome would be a domain-average decline of -5.4% (Fig. 4.7b) and -9.1% (Fig. 4.7e) under RCP2.6 and RCP4.5, respectively. Achieving RCP2.6 or RCP4.5 would avoid a greater than one standard deviation change in SM_{dry_ssn} throughout nearly the entire domain, shedding light on the criticality of curbing emissions in preventing SM drying due to climate change. If RCP6.0 is attained, ensemble mean ΔSM_{dry_ssn} would be greater than one standard deviation of baseline SM_{dry_ssn} only at elevations between 1750-2750m in the Western and Northern Sierra, but changes at elevations outside this region would generally be within the range of baseline interannual SM_{dry_ssn} variability (Fig. 4.7h).

In addition to characterizing uncertainty in future SM_{dry_ssn} due to forcing scenario, hybrid downscaled ensemble projections illustrate uncertainty stemming from GCM spread; we can examine this uncertainty by evaluating differences in patterns of ΔSM_{dry_ssn} that correspond to the 10th and 90th percentiles of the GCM distribution. For each RCP, the "near-full" (10-90%) ensemble range in ΔSM_{dry_ssn} is greatest above 2000m (and most pronounced above 3000m), reflecting the large spread in ΔSWE_{April_1st} and ΔT_{AMJJ} projections at higher elevations. Under RCP8.5, the average change in SM_{dry_ssn} corresponding to the 10th percentile of the GCM distribution is -17.4% in the 1500-3000m elevation band, compared to -27.1% for the 90th percentile of the GCM distribution; despite this large near-full ensemble range, absolute changes in SM_{dry_ssn} are greater than one standard deviation of baseline SM_{dry_ssn} at elevations between 1500-3000m for all GCMs under RCP8.5.

4.6 Discussion

4.6.1 Are soil moisture losses driven by SWE loss or ET increases?

Spatial patterns of coefficients α (average expected relative change in SM_{dry_ssn} per centimeter April 1st SWE loss) and β (average expected relative change in SM_{dry_ssn} per degree April-July near surface warming) from Eq. (1), together with spatial patterns of ΔSWE_{April_1st} and ΔT_{AMJJ} from the dynamical simulations can shed light on regions where SM_{dry_ssn} changes are driven by loss of SWE_{April_1st} or by enhanced ET due to ΔT_{AMJJ}.

Figs. 4.8a and 4.8b present the spatial pattern of ΔSM_{dry_ssn} explained by ΔSWE_{April_1st} and ΔT_{AMJJ}, respectively. The spatial pattern in Fig 4.8a is obtained by multiplying α (average expected relative change in dry season soil moisture per centimeter April 1st SWE loss, unit: % per cm) by the dynamically downscaled 5-model ensemble mean change in SWE_{April_1st} (cm). The spatial pattern in Fig 4.8b is obtained by multiplying β (average expected relative change in dry season soil moisture per degree April-June near-surface warming, unit: % per °C) by the dynamically downscaled 5-model ensemble mean April-July warming. The hybrid dynamical-statistical soil moisture model is designed such that the sum of these spatial patterns approximately equals the dynamically downscaled 5-model ensemble mean relative change in end-of-21st-century SM_{dry_ssn} under RCP8.5.

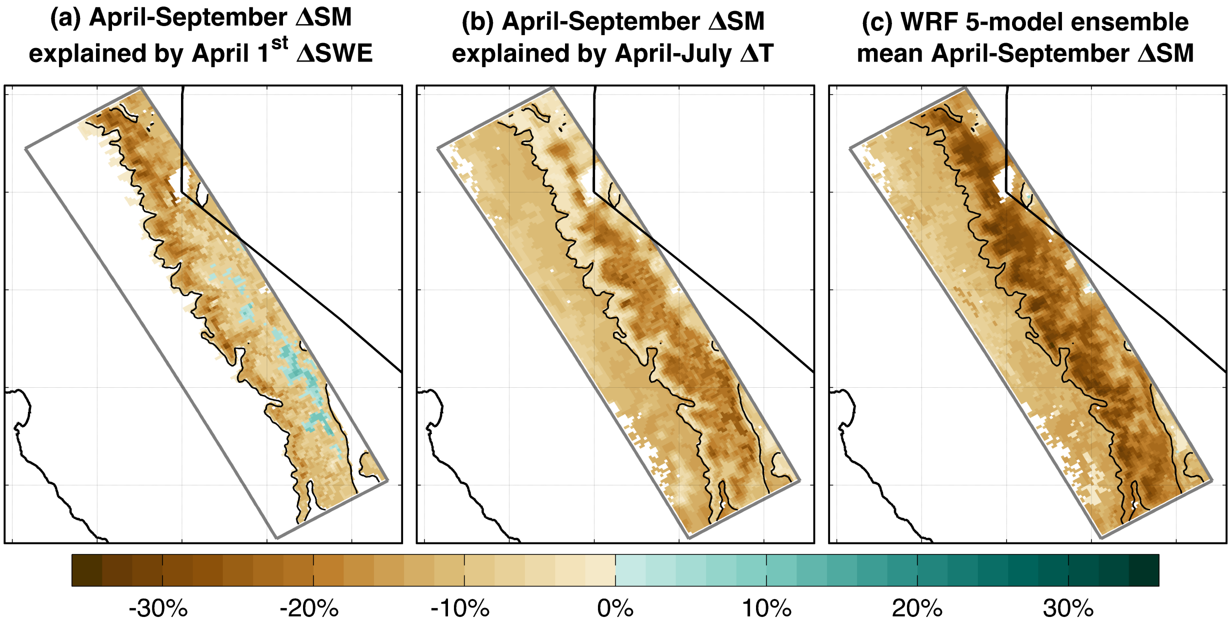

Fig. 4.8: Spatial pattern of end-of-21st century dry season (April-September) soil moisture drying explained by (a) changes in April 1st snow water equivalent (SWE) and (b) April-July warming. The spatial pattern in (a) is obtained by multiplying α (average expected relative change in dry season soil moisture per centimeter April 1st SWE loss) by the dynamically downscaled 5-model ensemble mean absolute change in April 1st SWE. The spatial pattern in (b) is obtained by multiplying β (average expected relative change in dry season soil moisture per degree April-June near-surface warming) by the dynamically downscaled 5-model ensemble mean April-July warming. The dynamically downscaled 5-model ensemble mean end-of-21st-century change in April-September soil moisture relative to the end-of-20th-century is shown in (c). The 2000 m topography contour is shown in black.

In the low-lying Sacramento and San Joaquin Valleys, April-September SM drying is explained exclusively by warming-driven ET enhancement, as baseline SWE_{April_1st} at these low-elevation (below 1400m) locations is nearly 0 cm and the end-of-21st-century change in SWE_{April_1st} is similarly negligible. Conversely, declining SM_{dry_ssn} at some mid-elevation locations along the western mountain slopes and in the northern Sierras is almost entirely explained by changes in SWE_{April_1st}. In the 2000-2500m elevation range, changes in April 1st SWE explain a spatial-averaged dry season SM drying of -13.2%, while changes in April-July near-surface temperature explain additional drying of a similar magnitude (-11.8%); this suggests both ΔT_{AMJJ} and $\Delta \mathrm{SWE}_{April\_1st}$ play critical roles in explaining declining $\Delta \mathrm{SM}_{dry\_ssn}$ at these locations, contributing to the large intermodel spread in SM_{dry_ssn} within this elevation band (Fig. 4.7). At higher elevations (2500-3000m), changes in April 1st SWE explain a SM_{dry_ssn} change of -3.2%, but changes in SM_{dry_ssn} within this elevation band are largely explained by April-July warming, which leads to an additional -17.8% SM_{dry_ssn} drying.

Because the highest elevations (above 3000m) in the southern Sierras are well above the baseline snow line, end-of-21st-century P continues to fall mostly as snow, and thus SWE_{April_1st} losses are buffered. Interestingly, ensemble-mean SWE_{April_1st} at these locations is projected to slightly increase in the dynamical downscaling simulations due to increased winter P (Fig. 4.4c), and this increased SWE is expected to moisten SM_{dry_ssn} by 5-15% at the highest elevations. However, SM_{dry_ssn} drying due to warming-driven ET enhancement outweighs SM_{dry_ssn} moistening due to increased April 1st SWE, and so the net result is declining SM_{dry_ssn} at the highest elevations (Fig. 4.8c). Overall, Fig. 4.8 sheds light on the regions and elevations within the Sierra Nevada where SM_{dry_ssn} declines are explained by changes in April 1st SWE versus by early summer warming (and the associated increase in ET).

4.6.2 Increased length of summer dry period

In addition to projected decreases in the magnitude of SM_{dry_ssn}, the dynamical simulations also reveal a lengthening of the summer dry period, where the summer dry period is taken to be the number of consecutive days during which near-surface SM is below a threshold level based on baseline SM.

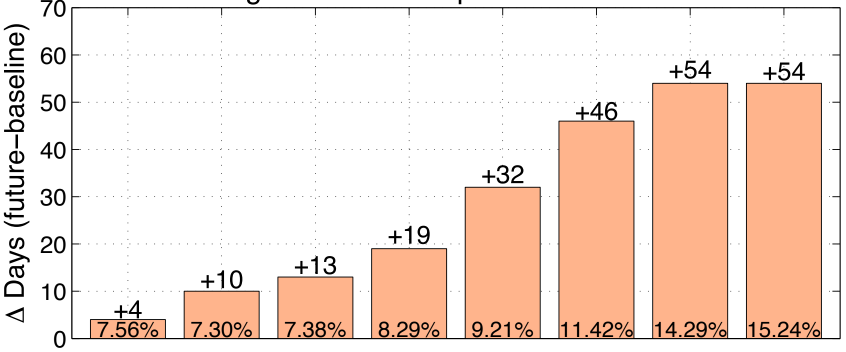
(a) Change in number of days per year with climatological SM ≤ 20th percentile of baseline SM

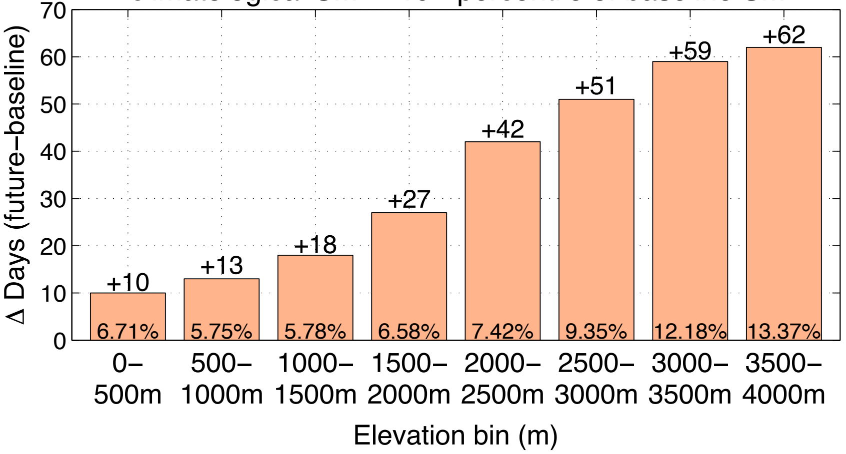
(b) Change in number of days per year with climatological SM ≤ 10th percentile of baseline SM

Fig. 4.9: Bar plot showing the dynamically-downscaled end-of-21st-century change (WY 2092-2101 minus WY 1992-2001) in the number of days per year with 0-10cm soil moisture less than or equal to the (a) 20th and (b) 10th percentiles of baseline daily soil moisture distribution. Results are averaged over grid points within 500m elevation bins and over the five dynamically downscaled GCMs. Text above each bar denotes the ensemble-mean change (unit: days), and text within the bar denotes the volumetric soil moisture corresponding to the (a) 20th and (b) 10th percentiles of the baseline daily soil moisture distribution for the corresponding 500m elevation bin.

Fig. 4.9 presents the dynamically downscaled 5-model ensemble-mean end-of-21st-century change (WY 2092-2101 minus WY 1992-2001) in the number of days per year with 0-10cm SM less than or equal to the (a) 20th and (b) 10th percentiles of baseline daily soil moisture distribution. Results are averaged over grid points within 500m elevation bins and over the five dynamically downscaled GCMs. Text above each bar denotes the ensemble-mean change (unit: days), and text within the bar denotes the volumetric soil moisture corresponding to the (a) 20th and (b) 10th percentiles of the baseline daily soil moisture distribution for the corresponding 500m elevation bin. The 10th and 20th percentiles of the baseline daily soil moisture distribution correspond to 37 and 74 days per year, respectively. For example, the 20th percentile of baseline daily climatological SM in the 2000-2500m elevation range corresponds to a SM of 9.21%, and it is projected that by the end-of-21st-century, an additional 32 days per year will have SM below this value.

Fig. 4.9 reveals ensemble-mean projected lengthening of the summer dry period, as all elevations experience an increase in the number of days per year during which SM is below a threshold based on the baseline daily SM distribution. The increase in the length of the summer dry period is greatest at higher elevation. Additionally, at grid points above 3500m, it is projected that by the end-of-21st-century, there will be almost three times the number of days per year with SM less than or equal to the volumetric SM content corresponding to the 10th percentile of the baseline daily SM distribution (13.37%). This longer and drier summer dry period results from reduced snowpack, earlier runoff and enhanced ET, and has implications for wildfire that will be considered in section 4.7.

4.6.3 Study limitations

The pseudo global-warming method described in section 4.2.1 imposes the same internal variability on both the baseline and future simulations. A consequence of this framework is that the frequency of synoptic events entering the outermost domain does not change in the future, but their characteristics (e.g. intensity, duration) freely evolve while propagating inwards (though this evolution is somewhat constrained due to spectral nudging). Possible future changes to natural climate variability over the Pacific Ocean, like the El Nino-Southern Oscillation (Cai et al. 2014), could impact California *P* (and SM) through teleconnections and our dynamical downscaling framework does not fully account for this possibility. However, this study aims to understand how a 10-year historical period of SM responds to large-scale end-of-21st-century perturbations, and due to the limitations of our methodology, we can only address mean changes in SM.

4.7 Summary and implications

By dynamically downscaling five CMIP5 GCMs, this study presents a high-resolution examination of how soil moisture in the Sierra Nevada region responds to an aggressive warming scenario by the end of the 21st century. The dynamical simulations reveal robust, statistically significant declines in dry season (April–September) near-surface (0-10cm) soil moisture, with a domain-average ensemble-mean end-of-21st-century change of -15.9% under RCP8.5. The depletion of dry season soil moisture is attributed to thermodynamically driven snowpack reductions (through both more precipitation as rain than snow and enhanced melting) and evapotranspiration enhancement; together, these processes significantly dry spring and summertime soils despite any precipitation increases.

By developing a hybrid dynamical-statistical downscaling model, we are able to quickly project high-resolution end-of-21st-century changes to Sierra Nevada soil moisture for an ensemble of CMIP5 GCMs under a range of emissions scenarios. This hybrid model is based on dynamically downscaled relationships between dry season soil moisture, April 1st snow water equivalent and April–July warming. Uncertainty in future dry season soil moisture stems from both forcing scenario and intermodel spread, and it cannot be said that soil moisture throughout the entire Sierra Nevada region will inevitably dry. However, the overwhelming evidence presented here suggests that the most likely (ensemble-mean) result is domain-wide soil moisture drying, with the strongest drying at mid-elevations in the western and northern Sierra. While this conclusion supports projected large-scale soil moisture drying over the Western US (Collins et al. 2013), it is clear that downscaling allows us to reach strong conclusions about future regional soil moisture by capturing the Sierra's fine-scale topography and associated orographic processes.

Though this study does not directly examine drought per se, its major result of depleted spring and summer soil moisture is consistent with previous 21st-century projections of increased drought severity and intensity over California. Cook et al. (2015) used several soil moisture-based metrics to examine drought severity over the US Southwest, including California, within the CMIP5 GCMs. They found remarkably higher drought risk in the 21st century compared to historical conditions within all models, a result owing to increased summertime evaporative demands that offset any precipitation gains. In addition to projected increases in Western US drought severity and frequency, Sheffield and Wood (2008) found that the spatial extent of droughts might also expand due to projected SM decreases.

Significant drying of Sierra Nevada soil moisture is likely to have major implications for future wildfire activity over California. The strong seasonality of Sierra Nevada hydroclimate, with cool and wet winters that promote plant growth during the warm and dry summers, already supports wildfire activity. Moreover, forest wildfire activity in the Western United States has increased in recent decades (Westerling et al. 2006; Littell et al. 2009; Dennison et al. 2014). This increase has been attributed to spring/summer warming, reduced snowpack, earlier snowmelt and longer/drier summer fire season soils (Westerling et al. 2006). The major result of this study suggests it is likely that future wildfire activity will increase in the future as a result of drier fire season soils. This corroborates previous work that projects larger and more frequent wildfires in the coming decades both in the Western US (Westerling and Bryant 2008; Spracklen et al. 2009), Mediterranean-type ecosystems (Batllori et al. 2013) and globally (Flannigan et al. 2009). Moreover, our projections of a longer and drier summer dry period are consistent with previous research on observed increases in the length of the summer fire season (Westerling et al. 2006).

5 On the relationship between runoff timing and elevation in California's Sierra Nevada

5.1 Introduction

As noted in Chapters 3-4, understanding the response of the snow-dominated hydrological cycle of California's Sierra Nevada to future warming scenarios is critical to satisfying freshwater demands for municipal, economic and ecological purposes. In Chapter 3, we produced and examined 3-km spatial resolution dynamically-downscaled end-of-21st-century runoff timing projections for five global climate models (GCMs) from phase 5 of the Coupled Model Intercomparison Project under the RCP8.5 forcing scenario. The projections reveal that future warming significantly advances snowmelt-driven surface runoff timing throughout the Sierra Nevada, particularly at mid-elevations in both the western and northern Sierras. While this examination was done at the gridpoint level, it is also critical to understand chances to runoff timing at the watershed level in order to manage surface water resources. This is especially true in deeply drawn-upon hydrologic systems like the Sierra Nevada Mountains of California (Stewart 2013).

Past research has often emphasized the large-scale, systematic response of regional watersheds to large-scale changes in atmospheric conditions, precipitation and temperature. Regional or watershed-level differences within that systematic response have largely been explained through variations in elevation, latitude or longitude. For example, in an examination of the timing of snowmelt runoff for 84 rivers in the western United States over water years 1950–2003, McCabe and Clark (2005) found that the timing of snowmelt runoff for many has shifted to earlier in the snowmelt season, and that most of the largest runoff timing trends occur at sites with the lowest elevations; this relationship between changes in snowmelt runoff timing and elevation was found to be consistent with previous studies (Mote et al. 2005; Regonda et al. 2005; Stewart et al. 2004). Similarly, Stewart et al. (2005) investigated the timing of snowmelt-derived streamflow at a network of 302 gauges in Western North American over 1948 to 2002, finding extensive and regionally-coherent trends toward earlier snowmelt and streamflow, with the strongest trends at mid-elevation gauges in the interior Northwest, Western Canada, and coastal Alaska.

Elevational variations in snowpack and runoff have also been examined within the Sierra Nevada Mountains. In an assessment of the sensitivity of spring snowpack to climatic change based on analysis from 177 snow courses in the Sierra Nevada Mountains over 1950-2002 and gridded monthly mean temperature and total precipitation, Howat and Tulaczyk (2005) found lower-elevation watersheds in the northern Sierra Nevada to be most sensitive to warming, with greatest sensitivity in areas around the Feather, American, and Yuba river drainages. Moreover, in an assessment of the response of fifteen Sierra Nevada watersheds to future warming using the Water Evaluation and Planning System model forced by the DAYMET dataset perturbed by temperature increases, Young et al. (2009) found the 1750m to 2750m elevation range to be most sensitive to moderate warming, as that elevation range experienced the largest reduction in snowmelt volume. Moreover, Young et al. (2009) noted that because the upper elevations of the Feather, Yuba and American River watersheds predominantly fall in this elevation range, those watersheds are expected to be most affected, while higher elevation mountainous regions in the southern portion of the Sierras are expected to be impacted less by warming due to colder overall temperatures. Similarly, in a study of snowmelt dominated streamflow in four large Sierra

Nevada basins (Feather River, American River, Tuolumne River and Kings River), Maurer et al. (2007) used the Variable Infiltration Capacity (VIC) hydrologic model forced by downscaled GCM output perturbed by spatially uniform temperature increases to explore the vulnerability of runoff timing to warming at different elevations. They identified elevations in the 2000 to 2800m range as most sensitive to temperature increases.

Despite previous research attempts to characterize the vulnerability of Sierra Nevada watersheds to future warming, previous assessments of elevational variations in future runoff timing throughout the Sierra Nevada often entail idealized warming scenarios, in which a historical climatology is perturbed by a spatially uniform temperature change (e.g. Young et al. 2009, Maurer et al. 2007) to evaluate hydroclimate sensitivity within particular watersheds. There has not been a CMIP5 downscaling based assessment of the runoff timing changes at the watershed-level throughout the Sierra that takes into account the heterogeneity of future warming. This provides little insight into the elevational dependency of runoff timing changes on climate conditions other than temperature, as well as inadequate information to comprehensively evaluate future hydroclimate changes for all Sierra Nevada watersheds.

This study aims to respond to this gap by examining whether individual watersheds in the Sierra Nevada Mountain Range are projected to respond to climate change differently due to the non-uniform expression of climate change across the landscape or inherent physical watershed characteristics (e.g. distribution of elevation within the watershed, slope, aspect, etc). In particular, this study investigates the relationship between elevation and runoff timing at both the gridpoint and watershed levels for an end-of-20th-century historical baseline period and an end-of-21st-century projected future period under an aggressive "business-as-usual" forcing scenario (RCP8.5). This investigation reveals that runoff timing at certain elevation ranges and within particular watersheds throughout the Sierra Nevada is more vulnerable to climatic changes than others.

The goal of this study is to assess changes to runoff timing at the watershed-level in California's Sierra Nevada Mountains. In doing so, we reveal elevational-variations in runoff timing changes, and examine the extent to which runoff timing changes can be explained by elevation. This quantitative information is critical for water management, and helps to bridge the gap between the climate modeling community and state water planners. This study relies on dynamical downscaling of five GCMs from the Coupled Model Intercomparison Project phase 5 (CMIP5, Taylor et al. 2012) under the RCP8.5 forcing scenario. By downscaling coarse-resolution GCM output, we are able to resolve the complex topography of the Sierra Nevada and local topographic effects that are needed for credible simulations of Sierra Nevada hydroclimate that can be used to inform regional water resources planning and adaptation strategies (e.g., Fowler et al. 2007).

This chapter is organized as follows: Section 5.2 describes the methods and data used in this study, including a description of the dynamical downscaling model configuration, watershed boundary dataset, and runoff timing metric. Section 5.3 presents end-of-20th-century climatological runoff timing patterns in California's Sierra Nevada at the grid point level; elevational variations in these patterns are explored are shed light on the extent to which future runoff timing changes can be explained by elevation. Section 5.4 describes end-of-21st-century runoff timing changes for Sierra Nevada at the watershed level and discusses sub-regional patterns in the response and sensitivity of runoff timing for Sierra Nevada watersheds. Finally, section 5.5 summarizes the major findings of this chapter and their implications.

5.2 Methods

5.2.1 Dynamical downscaling framework

The dynamical downscaling framework in this study is the same as that employed in Walton et al. (2016), Sun et al. (2016), and Chapters 3-4. The text in section 5.2.1 is derived from Schwartz et al. (2016b) with minor modifications.

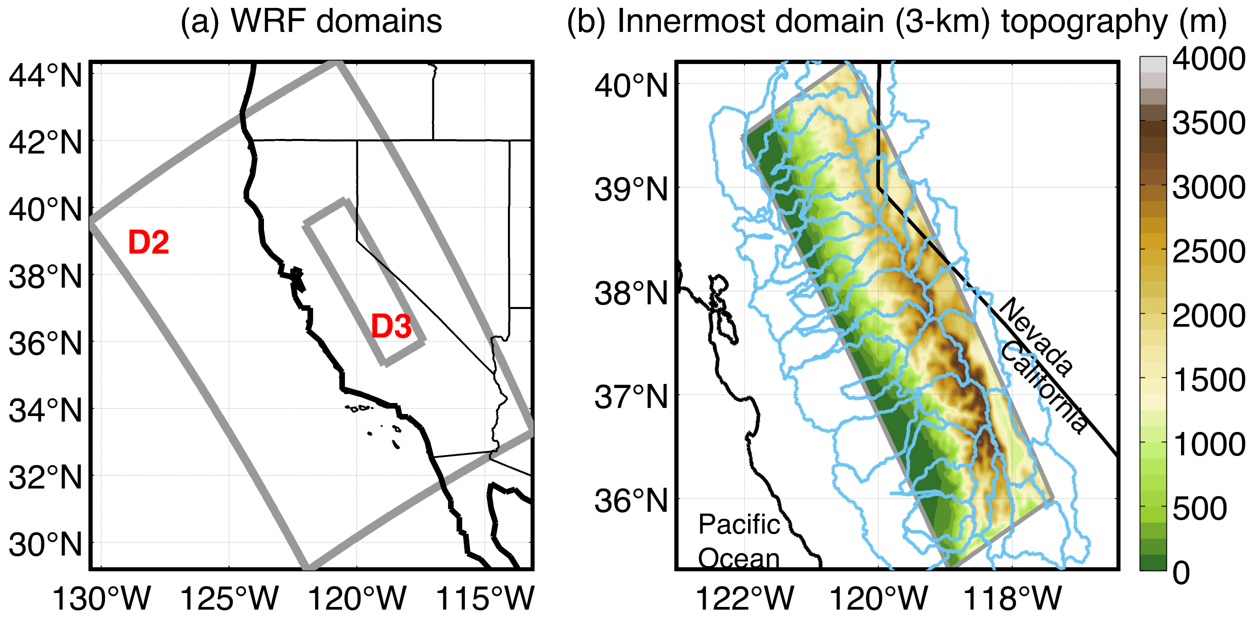

Fig. 5.1: a) Model setup, showing the two innermost nested domains: D2 (9 km horizontal resolution) and D3 (3 km horizontal resolution). (b) Topography (m) of the innermost domain (3-km resolution) of the regional simulation, with the state borders of California and Nevada in black. Blue lines in (b) outline the 47 watersheds of the Sierra Nevada Mountains according to the United States Geological Survey's Watershed Boundary Database (http://nhd.usgs.gov/wbd.html), which delineates the spatial extent of surface water drainage.

Dynamical downscaling is performed using the Weather Research and Forecasting (WRF) model version 3.5 (Skamarock et al. 2008). WRF is coupled to the community Noah land surface model with multi-parameterization options (Noah-MP, Niu et al. 2011). Three one-way nested domains are used to represent the complex topography of California and the Sierra

Nevada as accurately as possible (Fig. 5.1a). The outermost domain spans the entire U.S. West Coast and adjacent Pacific Ocean at 27 km horizontal resolution. The middle domain, at 9 km resolution, covers all of California. Finally, the innermost domain, at 3 km resolution, spans the eastern edge of the Central Valley to the leeside of the California Sierra Nevada Mountains (Fig. 5.1b); this domain is the focus of this study.

In each domain, all variables within five grid cells from the horizontal lateral boundary are relaxed toward the corresponding values at the boundaries. To provide a better representation of surface and boundary layer processes, the model's vertical resolution is enhanced near the surface, with 30 out of 43 total sigma-levels below 3 km. WRF parameterization testing has been done to optimize the model's performance in hydroclimate simulations, with the aim of improving the realism of simulated snowpack and streamflow processes in the Sierra Nevada. The package of physical parameterizations consists of the New Thompson microphysics scheme (Thompson et al. 2008), Dudhia shortwave radiation scheme (Dudhia 1989), Rapid Radiative Transfer Model longwave (RRTM) longwave radiation scheme (Mlawer et al. 1997), MYNN Level 2.5 surface/boundary layer scheme (Nakanishi and Niino 2006), and Old Kain-Fritsch cumulus convection scheme (Kain and Fritsch 1990). Spectral nudging of temperature, zonal and meridional winds, and geopotential height is employed above the boundary layer (roughly 850 hPa) over the outermost 27 km resolution domain.

Climate changes signals are produced from a single baseline simulation and five future simulations. The baseline simulation spans October 1991 to September 2001 (water years 1992–2001; hereinafter "WY 1992–2001") and is a dynamical downscaling of the National Centers for Environmental Prediction's 6-hourly North America Regional Reanalysis (NARR; Mesinger et al. 2006). NARR is a relatively coarse-resolution (32 km) reanalysis dataset that provides the lateral boundary forcings and initial conditions for the outermost WRF domain in Fig. 1a. The baseline simulation allows us to evaluate the model's ability to simulate regional runoff timing based on a comparison to observational data (Section 3.2.2) and serves as a climate state against which we can compare future climate simulations to measure change.

Using the same model configuration as the baseline, we perform a five-member ensemble of dynamical downscaling experiments to simulate a future end-of-21st-century climate. The simulations go from October 2091 to September 2101 (water years 2092–2101, hereinafter "WY 2092–2101"). We dynamically downscale GCM experiments forced by the Representative Concentration Pathway 8.5 (RCP8.5) forcing scenario (Riahi et al. 2011). Out of all available CMIP5 GCMs forced by RCP8.5, we select five: CNRM-CM5, GFDL-CM3, INM-CM4, IPSL-CM5A-LR, and MPI-ESM-LR. These GCMs approximately sample the range of end-of-21st century near-surface temperature and precipitation changes over California (Walton et al. 2016).

To produce boundary conditions for the future WRF simulations, we add a perturbation reflecting the mean change in GCM climatology to NARR data for WY 1992–2001, following Schar et al. (1996), Hara et al. (2008), Kawase et al. (2009) and Rasmussen et al. (2011). To calculate these GCM climate changes, we first quantify the differences in GCM monthly climatology between the historical and RCP8.5 experiments (2081–2100 average minus 1981–2000 average). Differences are calculated for temperature, humidity, zonal and meridional winds, and geopotential height. Then, for each of the five dynamically-downscaled GCMs, we perturb the baseline 6-hourly NARR reanalysis data for each month by the corresponding monthly mean climatological change. The perturbed NARR fields then serve as WRF boundary conditions for five future climate simulations. This method allows us to assess how WY 1992–2001 would transpire if the mean climate were altered to reflect the climate changes projected by each of five

GCMs. It allows us to quantify how the climate change signals simulated in the GCMs are expressed at the regional scale, without the future simulations being subject to significant biases in mean state often found in GCMs. For additional information on model setup, parameterizations and design of future simulations, the reader is referred to Walton et al. (2016).

5.2.2 Description of USGS HUC boundaries

To delineate watershed boundaries, we rely on the United States Geological Survey's eight-digit Hydrological Unit Code (HUC-8) dataset available at water.usgs.gov/GIS/huc.html. This watershed boundary dataset delineates the spatial extent of surface water drainage. Forty-seven 8-digit HUC units are found within the innermost domain of our dynamical downscaling simulation, and light blue lines in Fig. 5.1b outline these watersheds. The heavy computational cost of dynamical downscaling prevents us from simulating the complete spatial extent of each HUC-8 within California at 3-km resolution, and Fig. 5.1b shows us that our innermost domain, which is centered on the spine of the Sierra Nevada Mountains, captures the strong majority of higher elevation grid points within each of the 47 HUC-8 watersheds at a high spatial resolution. These higher elevation grid points are the primary contributors to surface runoff generation throughout the Sierra Nevada. Previous research has noted that water from the Sierra Nevada is the source of most water used for agricultural and municipal purposes in California, and hence runoff in the Sierra defines hydrologic supply statewide (Mao et al. 2015). As such, our domain captures the most important areas of watersheds in the Sierra Nevada, particularly the areas that generate much of the Sierra's snowmelt-driven surface runoff used for agricultural and municipal purposes in California.

5.2.3 Runoff timing metric

As a measure of runoff timing, we consider the date in the water year (October 1 – September 30; hereinafter WY) by which 50% of the cumulative WY surface runoff has occurred (R50). R50 (often called the center of runoff volume) is widely used as a metric of snowmelt timing (Stewart et al. 2004, Stewart et al. 2005, McCabe and Clark 2005, Hayhoe et al. 2007, Kim and Jain 2011, Khattak et al. 2011). Regonda et al. (2005) suggest that R50 is a more robust indicator of snowmelt timing (in its relation to climatic variability and change) than the day of peak flow.

5.2.4 Evaluation of downscaling framework's simulation of runoff timing

Section 3.2.2 assesses the ability of this dynamical downscaling framework to reproduce runoff timing variations during the baseline period by comparing simulated R50 to observations obtained from the United States Geological Survey Hydro-Climatic Data Network-2009 (USGS HCDN-2009, http://waterdata/usgs.gov/nwis/), and we briefly recapitulate the findings of that evaluation exercise here. Section 3.2.2 found strong agreement between simulated and observed R50 dates, indicating the dynamical downscaling framework is able to capture the main features of spatial and temporal variability in runoff timing across the Sierra Nevada. Given that the 11 USGS streamflow gauges used in the evaluation exercise represent a variety of elevations, drainage areas and USGS eight-digit Hydrologic Unit Codes across Sierra Nevada creeks and rivers, it is very reasonable to analyze changes to runoff timing on a watershed basis.

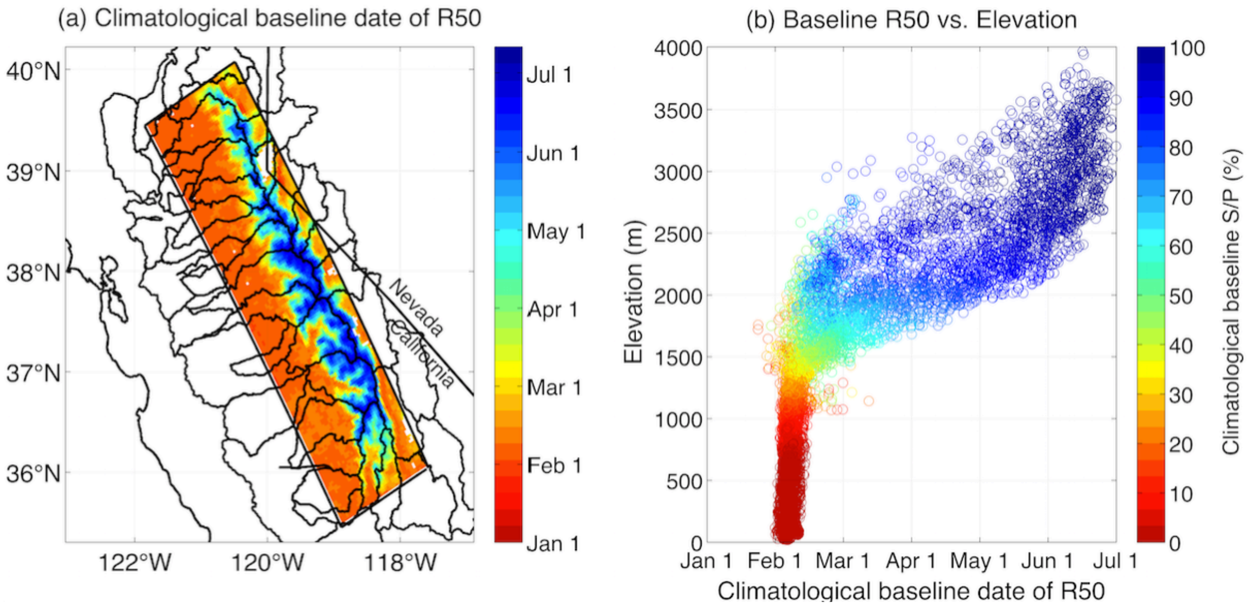

Fig. 5.2: (a) Baseline (October 1991–September 2001) climatological date of R50, which represents the date in the water year (October 1–September 30) by which 50% of the cumulative surface runoff has occurred. Black lines outline the 47 watersheds of the Sierra Nevada Mountains according to the United States Geological Survey's Watershed Boundary Database (http://nhd.usgs.gov/wbd.html), which delineates the spatial extent of surface water drainage. (b) Baseline (October 1991–September 2001) climatological date of R50 as a function of elevation (m). Colors in (b) indicate the climatological baseline fraction of precipitation as snow.

5.3 Runoff timing and elevation at the gridpoint level

Fig. 5.2a presents the spatial pattern of baseline (WY 1992–2001) climatological date of R50 in the 3-km spatial resolution domain (seen in Fig. 5.1b), and Fig. 5.2b presents the baseline (WY 1992–2001) climatological date of R50 as a function of elevation for each gridpoint in Fig. 5.2a. Colors in Fig. 5.2b indicate the climatological fraction of precipitation as snow (S/P) for each gridpoint. Climatological R50 generally occurs after March 1st throughout the mountainous regions of the Sierra Nevada (elevations greater than 1500m) and shifts to even later in the water year as both elevation and S/P increase. At lower elevations in the Northern Sierras where annual S/P ranges from 0.6 to 0.8, climatological R50 generally occurs before the start of summer.

However, mid to high elevations over the Central and Southern Sierras have a higher S/P ratio (0.8 to 0.95), which generates snowmelt-driven surface runoff throughout the summer months, pushing back climatological R50. For example, R50 in the mountains just southwest of Mono Lake occurs as late as the beginning of July. Throughout the Central Valley, Owens Valley and western Great Basin Desert (along the California-Nevada border), annual precipitation is low, and any precipitation typically falls as rain (S/P < 0.2), so surface runoff timing matches precipitation timing and R50 is generally in February.

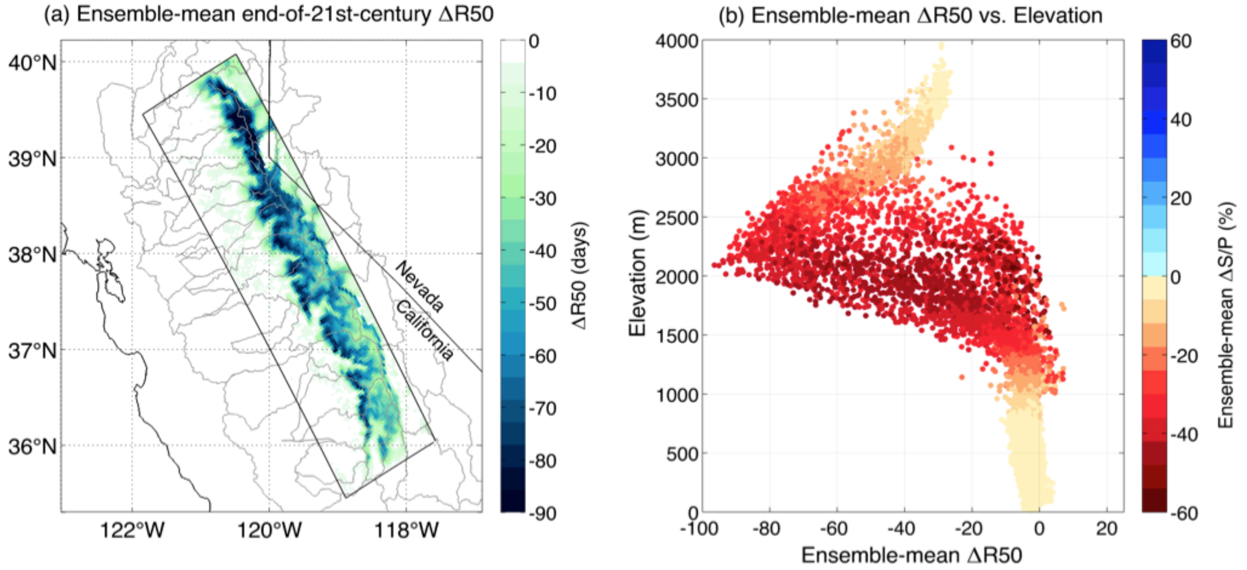

Fig. 5.3: (a) End-of-21^{st}-century change (water years 2092-2101 average minus 1992-2001 average, unit: days) in R50 under the RCP8.5 emissions scenario averaged over five dynamically downscaled GCMs (CNRM-CM5, GFDL-CM3, inmcm4, IPSL-CM5A-LR, and MPI-ESM-LR). Gray lines outline the 47 watersheds of the Sierra Nevada Mountains. (b) Five model ensemble-mean end-of-21^{st}-century change in R50 (days) as a function of elevation (m), colored by the five-model ensemble-mean end-of-21^{st}-century absolute change in the fraction of precipitation as snow (%).

The dynamically downscaled WRF end-of-21^{st}-century change (WY 2092–2101 minus WY 1992–2001) in R50 (ΔR50, unit: days) under the RCP8.5 emissions scenario average over five GCMs (CNRM-CM5, GFDL-CM3, INM-CM4, IPSL-CM5A-LR, and MPI-ESM-LR) is presented in Fig 5.3a. As discussed in Chapter 3, advances in R50 are projected at all locations with substantial climatological baseline snowmelt-driven surface runoff. Moreover, the spatial pattern in Fig. 5.3a can be explained primarily by dynamically-downscaled 10-year mean near-surface (2-meter) springtime warming projections. Ensemble-mean advances in mean R50 are greatest in the Northern Sierras and the western-facing mountain slopes, and smaller at the highest elevations in the Southern Sierras.

Fig. 5.3b presents ensemble-mean end-of-21st-century ΔR50 as a function of elevation, where colors indicate the five-model ensemble-mean end-of-21st-century absolute change in fraction of precipitation as snow (S/P). Fig. 5.3b clearly indicates that elevations between 1800m and 2500m are projected to have the greatest and most significant runoff timing advances, as those elevations are close to the climatological freezing line, making them most susceptible to dramatic decreases in S/P. Decreased frozen precipitation, together with earlier snowmelt, results in strong R50 advances at these elevations. At higher elevations in the Southern Sierras (e.g. above 3000m), changes to S/P are quite small (around -5%), so advances in R50 are almost exclusively due to earlier snowmelt and not also due to decreased snowpack accumulation (through decreased S/P). The finding that the greatest advances in R50 timing are in the 1800m to 2500m elevation range is consistent with both Maurer et al. (2007) and Young et al. (2009).

Given strong elevational variations in ΔR50 (Fig. 5.3a), we aim to investigate the extent to which runoff timing changes can be determined by elevation alone at the grid point level. To do this, we build a simple statistical model that projects ΔR50 for each 100m elevation bin based on the average ΔR50 for that elevation bin as simulated through dynamical downscaling. Fig 5.4 presents the end-of-21st-century change (WY 2092-2101 minus WY 1992-2001) in R50 under the RCP8.5 emissions scenario as a function of elevation, where black dots represent individual grid points in the innermost domain of Fig. 5.1a., and the red line in Fig 5.4 presents the average change in R50 averaged across each 100-m elevation bin.

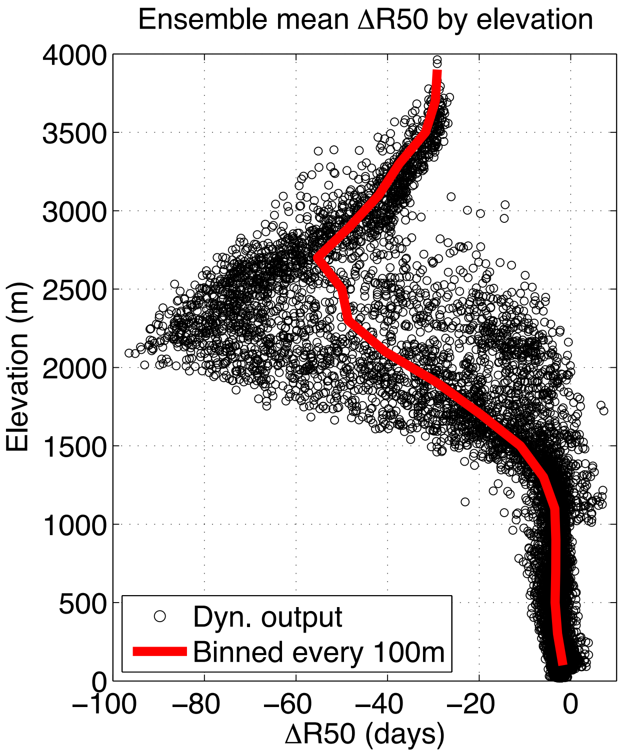

Fig. 5.4: End-of-21st-century change (water years 2092-2101 average minus 1992-2001 average, unit: days) in R50 under the RCP8.5 emissions scenario as a function of elevation (unit: m). Results are averaged over five dynamically downscaled GCMs. The red line shows the average change in R50 for each 100m elevation bin.

Next, we examine the spatial pattern of R50 that is produced using the elevation-averaged change in R50 for each grid point. Fig. 5.5b presents the five-model ensemble-mean end-of-21st-century change (WY 2092-2101 minus WY 1992-2001) in R50 under RCP8.5 that is produced using the elevation-based approach described above. This can be compared to the five-model ensemble-mean end-of-21st-century change (WY 2092-2101 minus WY 1992-2001) in R50 under RCP8.5 that is produced through dynamical downscaling (Fig. 5.5a). To a first approximation, the elevation-based R50 model is able to capture some of the ΔR50 spatial pattern, and the spatial correlation coefficient between patterns seen in Fig. 5.5a and Fig. 5.5b is $r = 0.80$, indicating that elevational averages in ΔR50 alone can explain 64% of the spatial variations in runoff timing changes that arise through dynamical downscaling.

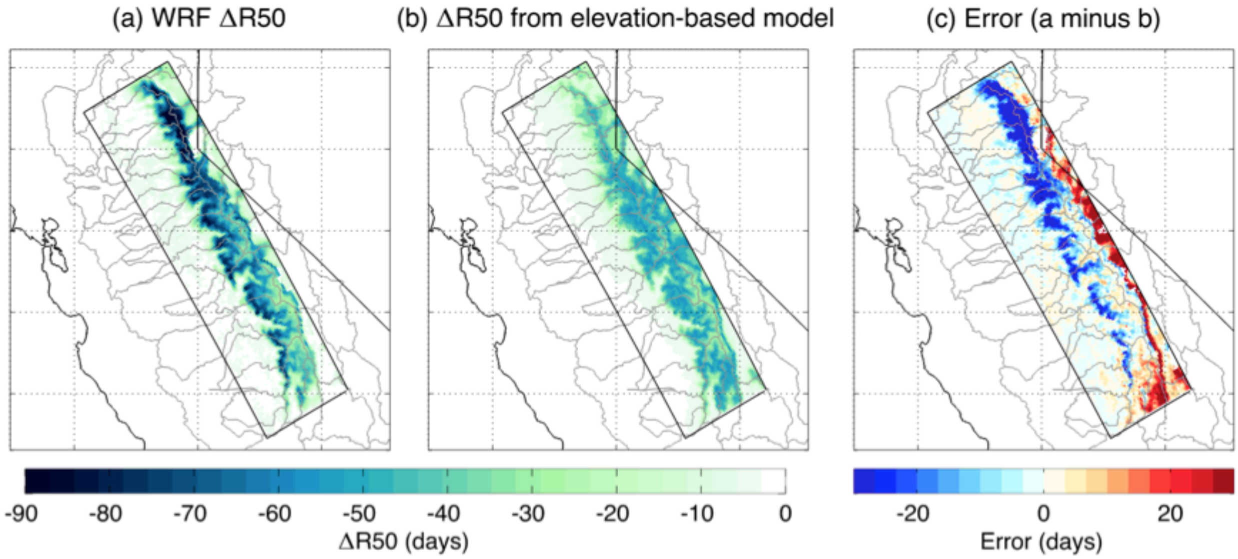

Fig. 5.5: End-of-21st-century change (water years 2092-2101 average minus 1992-2001 average, unit: days) in R50 under the RCP8.5 emissions scenario (a) simulated through dynamical downscaling and (b) produced from an elevation-based model. Results are averaged over five dynamically downscaled GCMs. (c) Difference between subplots (a) and (b), which highlights regions where the elevation-based model underestimates the advance of R50 (blue) and overestimates the advance of R50 (red). Unit: days.

The errors in runoff timing projections produced by this elevation-based approach are presented in Fig. 5.5c; this shows the difference between Fig. 5.5a and Fig 5.5b. Regions where the elevation-based model underestimates the advance of R50 are presented in blue, while regions where the elevation-based model overestimated the advance of R50 are presented in red. Fig. 5.5c reveals a noticeable and strong east vs. west pattern in the model bias, as the elevation-based R50 model systematically underestimates the advance of R50 (by 20-30 days) at mid-elevations (1500-2800m) in the western Sierras and systematically overestimates the advance of R50 at the same elevations in the eastern Sierras. This reveals that for gridpoints with the same elevation, those on the western slopes of the Sierra are projected to have greater advances in mean end-of-21st-century R50 than gridpoints at the same elevation in the eastern Sierras, suggesting the possibility of a greater vulnerability of western Sierra Nevada watersheds to climatic change. The difference in runoff timing changes between the eastern and western Sierras is perhaps due to physical watershed characteristics or the non-uniform expression of climate change across the landscape (e.g. stronger climate change signals imposed on the western Sierras than eastern Sierras). However, at higher elevations (e.g. above 2800m), the differences between end-of-21st-century advances in R50 in the western Sierras and at gridpoints of similar elevations in the eastern Sierras are not strong.

Moreover, the elevation of greatest ΔR50 in the western Sierras is approximately 2100m, while this elevation is higher in the eastern Sierras (around 2300m). This strong difference between R50 outcomes in the eastern and western Sierra Nevada at elevations between 1500m to 2800m might be due to differences in lapse rate on the windward and leeward sides of the Sierras, which would affect the elevation of the freezing line (and therefore the elevation of the snowline, strongest SAF enhanced-warming, SWE reductions and snow cover loss). As moist air from the Pacific and coastal California ascends up the windward western Sierra, it rises at approximately a moist adiabatic lapse rate. Moisture is wrung out of air passing over the Sierras toward the inland desert, and hence air subsides down the eastern Sierras closer to the dry adiabatic lapse rate. This suggests that the elevation of the freezing line in the eastern Sierra Nevada should be higher than in the western Sierra and sheds light on why the strongest R50 advances are projected to occur at a lower elevation in the western Sierra Nevada than in the eastern Sierra Nevada.

5.4 Runoff timing and elevation at the watershed level

Section 5.3 explored the relationship between runoff timing and elevation at the grid point level, and shed light on how this relationship varies in the western versus eastern Sierras. In this section, we aim to understand runoff timing changes at the watershed level’ this assessment is critical for surface water resources management, especially in deeply drawn-upon hydrologic systems like the Sierra Nevada Mountains (Stewart et al. 2013) of California and Nevada.

Fig. 5.6 presents the five-model ensemble-mean watershed-average end-of-21st-century R50 change as simulated through dynamical downscaling. Watershed-average R50 changes are not calculated by averaging R50 across the watershed, but rather by summing the daily climatological hydrograph across all gridpoints within a watershed, and then finding the centroid of that watershed-average hydrograph. This approach weights locations that generate significant surface runoff higher than those that produce little surface runoff, and allows us to examine R50 changes in a way that considers large advances in R50 to be the most significant and relevant at grid points with substantial annual surface runoff.

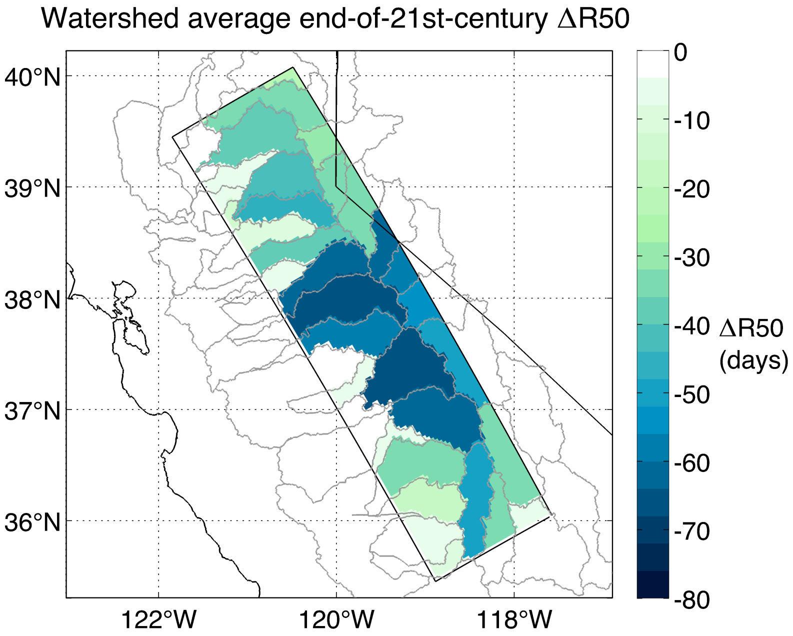

Fig. 5.6: Dynamically downscaled end-of-21st-century change (water years 2092-2101 average minus 1992-2001 average, unit: days) in R50 under the RCP8.5 emissions scenario. Watershed average changes are presented for the 47 watersheds of the Sierra Nevada. Results are averaged over five dynamically downscaled GCMs (CNRM-CM5, GFDL-CM3, inmcm4, IPSL-CM5A-LR, and MPI-ESM-LR). Gray lines outline the 47 watersheds of the Sierra Nevada Mountains.

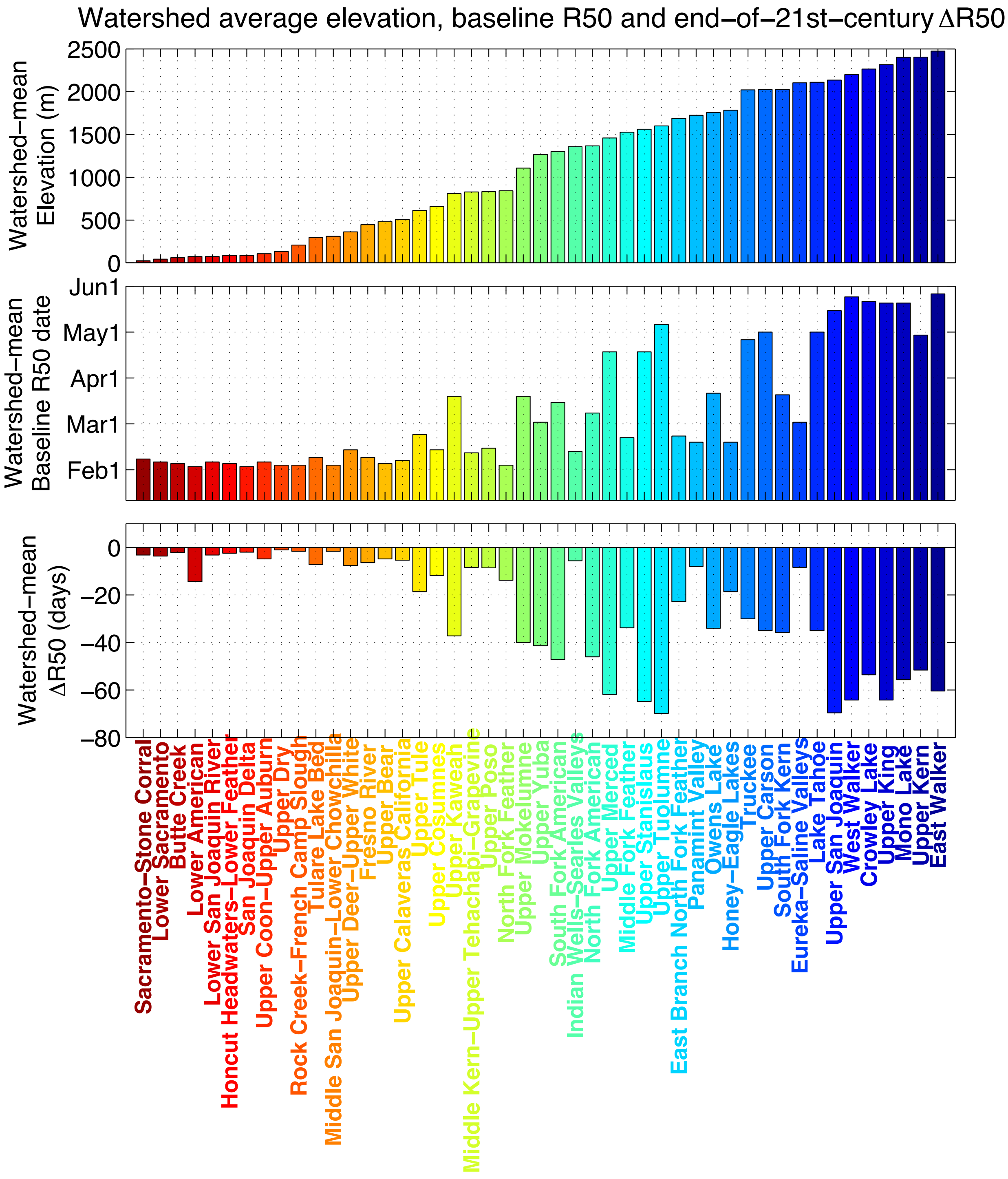

Fig. 5.7: Watershed average elevation (top, unit: meters), baseline (WY 1992-2001) R50 (middle) and end-of-21st-century change (water years 2092-2101 average minus 1992-2001 average, unit: days) in R50 under the RCP8.5 emissions scenario (bottom). Watershed names are presented at the bottom of the figure, and are arranged in order of watershed-mean elevation. End-of-21st-century changes in R50 are averaged over five dynamically downscaled GCMs (CNRM-CM5, GFDL-CM3, inmcm4, IPSL-CM5A-LR, and MPI-ESM-LR).

The spatial pattern in Fig. 5.6 reveals that watersheds in the central Sierra, on both the eastern and western slopes, are projected to have the most dramatic advances in watershed-average R50. This stems from not only having locations within the watershed with strong R50 advances, but also from those locations being ones that greatly contribute to surface runoff generation within the watershed. The magnitude of watershed-average changes in R50 in southern Sierra watersheds is less than those in neighboring watersheds to the north (in the central Sierra). Advances in R50 at the gridpoint level are generally small throughout these watersheds (Fig. 5.3a) because they are at elevations high enough and temperatures cold enough to remain below freezing under future warming scenarios.

To explore the relationship between elevation and watershed-average R50, Fig 5.6 presents watershed-average elevation (top), baseline climatological R50 (middle) and end-of-21st-century ΔR50 for each of the 47 watersheds of the Sierra Nevada, arranged from lowest mean elevation (dark red) to highest mean elevation (dark blue). Watersheds with mean elevations below 1000m (e.g. Lower Sacramento, Lower American, Tulare Lake Bed, etc.) are low enough (and therefore warm enough) that most precipitation falls as rain during the baseline period, so climatological runoff timing occurs in February at those low-elevation watersheds (Fig. 5.6, middle). Given already low S/P in these low elevation watersheds, impacts of future climate change on runoff timing are small (advances of 0-10 days, Fig. 5.6 bottom).

For watersheds with mean elevations above around 2000m (e.g. Lake Tahoe, Upper San Joaquin, West Walker, Crowley Lake, Upper King, Mono Lake, Upper Kern and East Walker), a clear relationship emerges between watershed-average elevation and its change in end-of-21st-century R50. Because the average elevation within those watersheds coincides with regions of greatest snow albedo feedback (Walton et al. 2016) and greatest April 1st snow water equivalent loss (Sun et al. 2016), advances in R50 are quite dramatic, with watershed-averages on the order of 50-70 days.

The relationship between watershed-average elevation and its end-of-21st-century R50 change for watersheds with mean elevations between 1000m-2000m is not as clear as that of watersheds with higher (e.g. above 2000m) or lower (e.g. below 1000m) mean elevations. For example, some watersheds with mean elevations in the 1000-2000m elevation range have significant watershed-average end-of-21st-century advances in R50 of about 60 days (e.g. Upper Merced, Upper Stanislaus, Upper Tuolumne), while others have mean advances of only 10-20 days (e.g. Middle Fork Feather, Panamint Valley, Indian Wells-Searles Valleys). It is surprising that some mid to high elevation watersheds exhibit strong advances in end-of-21st-century R50 while others project much smaller advances.

Of course, some of the range of watershed-average R50 sensitivity across these mid to high elevation watersheds can be explained through the examination of the watershed's elevation distribution (and not just watershed-mean elevation). The Middle Fork Feather Watershed, for example, has an average elevation of 1525m with a standard deviation of only 414m, suggesting much of the watershed's area is in a narrow range of elevations close to the historical climatological snowline. The Upper Merced Watershed has a similar average elevation (1459m), but a much large standard deviation of elevation distribution (945m), indicating area within this watershed is spread across a wider range of elevations and thus a greater portion of the Upper Merced is at heights either far above or far below the historical snowline, and thus not strongly susceptible to R50 changes under warming. The differences in elevation distributions between these watersheds of similar mean elevation help to shed light on differences in future R50 sensitivity between watersheds with similar average elevations.

5.5 Summary and implications

Assessing impacts of future temperature and precipitation changes to streams and rivers that originate in the Sierra Nevada is critical to understanding potential impacts to California's water supply, ecosystem health and economy. The objective of this chapter was to examine the relationship between elevation and runoff timing and to explore the extent to which gridpoint-to-gridpoint or watershed-to-watershed differences in runoff timing can be explained through elevation. This examination relies on dynamically downscaled simulations of end-of-20th-century historical climate and end-of-21st-century future climate projections. This chapter provides an initial attempt to characterize and explain gridpoint-to-gridpoint and watershed-to-watershed differences in runoff timing changes for the Sierra Nevada through elevational variations.

We find that elevations in the range of 1800m and 2500m are projected to have the greatest and most significant runoff timing advances, as this range of elevations experiences dramatic decreases in the fraction of precipitation as snow. Similarly, watersheds projected to have the most significant advances in surface runoff timing are those with mean elevations between 1500m to 2500m. The surface runoff generated in these watersheds occurs at elevations high enough to sustain seasonal snow cover and snowpack (that contributes to surface runoff) but not cold enough to remain below freezing under strong future warming. As a result, decreased frozen precipitation, together with earlier snowmelt, results in strong R50 advances at these elevations, and watersheds with mean elevations in the 1500m to 2500m range are most sensitive.

Overall, we find that the watersheds with the greatest projected advances in end-of-21st-century runoff timing are those in the central Sierra Nevada, as a great portion of their area is at elevations where R50 is significantly affected by warming and substantial surface runoff is produced at these elevations. Future work will connect watershed sensitivities to the communities they serve (e.g. the Tuolumne River Watershed and city of San Francisco) to characterize the vulnerability of water resources to future climate change impacts at the city level.

The results from this chapter should be viewed with the caveat that the dynamical downscaling framework imposes identical interannual variability levels between the baseline and future time slices. Possible changes to interannual variability patterns in the 21st century, for example the El Nino-Southern Oscillation phenomenon (Cai et al. 2014), could significantly impact overall precipitation levels and timing through atmospheric teleconnections, a factor that is not fully accounted for in this study. However, as the focus of this study is the change in mean runoff timing at the grid point and watershed levels, it is difficult to see how the absence of El-Nino-driven changes in overall precipitation would affect the conclusions significantly.

Through an investigation of the relationship between elevation and runoff timing, this chapter provides a first attempt at assessing changes to runoff timing at the watershed-level in California's Sierra Nevada Mountains. Future research will consider how the non-uniform expression of climate change across the landscape might impact watershed runoff timing vulnerability. Advances in watershed runoff timing projected in this study are likely to have major implications for California's water resource infrastructure, and it would be helpful from both a societal and policy perspective to examine whether the current infrastructure – built on the assumption that the snowpack of the Sierras melts gradually throughout the dry season – can accommodate such drastic changes to snowmelt timing.

6 References

Adam, J.C., A.F. Hamlet, D.P. Lettenmaier, 2009: Implications of global climate change for snowmelt hydrology in the twenty-first century. Hydrol. Process. 23, 962–972.

Aguado, E., D. Cayan, L. Riddle, and M. Roos, 1992: Climatic fluctuations and the timing of West Coast streamflow, J. Clim., 5, 1468–1483.

Arritt, R.W., and M. Rummukainen, 2011: Challenges in regional-scale climate modeling, Bull. Amer. Meteor. Soc., 92, 365–368, doi:10.1175/2010BAMS2971.1.

Baldocchi, D., et al., 2001: FLUXNET: A new tool to study the temporal and spatial variability of ecosystem-scale carbon dioxide, water vapor, and energy flux densities. Bull. Am. Meteorol. Soc., 82(11), 2415–2434.

Bales, R.C., J.J. Battles, Y. Chen, M.H. Conklin, E. Holst, K.L. O'Hara, P. Saksa, W. Stewart, 2011: Forests and water in the Sierra Nevada: Sierra Nevada watershed ecosystem enhancement project. Sierra Nevada Research Institute Rep. 11.1, 39 pp. [Available online at http://ucanr.edu/sites/cff/files/146199.pdf.]

Barnett, T.P., J.C. Adam, and D.P. Lettenmaier, 2005: Potential impacts of a warming climate on water availability in snow-dominated regions. Nature, 438, 303-309.

Barnett, T.P., D.W. Pierce, H.G. Hidalgo, C.B. Benjamin, D. Santer, T. Das, G. Bala, A.W. Wood, T. Nozawa, A.A. Mirin, D.R. Cayan, and M.D. Dettinger, 2008: Human-induced changes in the hydrology of the Western United States. Science, 319, 1080–1083.

Barrera-Escoda, A., M. Gonçalves, D. Guerreiro, J. Cunillera, J.M. Baldasano, 2013: Projections of temperature and precipitation extremes in the North Western Mediterranean Basin by dynamical downscaling of climate scenarios at high resolution (1971–2050). Climatic Change pp 1–16. doi:10.1007/s10584-013-1027-6.

Bates, B.C., Z.W. Kundzewics, S. Wu, and J.P. Palutikof, 2008: Climate Change and Water. Technical Paper of the Intergovernmental Panel on Climate Change. IPCC Secretariat, Geneva, Switzerland, 210 pp.

Batllori, E., M.-A. Parisien, M. A. Krawchuk, and M. A. Moritz, 2013: Climate change-induced shifts in fire for Mediterranean ecosystems. Global Ecology and Biogeography, 22, 1118-1129.

Berg, N., A. Hall, F. Sun, S. Capps, D. Walton, B. Langenbrunner, and J. Neelin, 2015: Twenty-First-Century Precipitation Changes over the Los Angeles Region. J. Climate, 28 (2), 401-421. doi:10.1175/JCLI-D-14-00316.1

Betts, R.A., O. Boucher, M. Collins, P.M Cox, P.D. Falloon, N. Gedney, D.L. Hemming, C. Huntingford, C.D. Jones, D.M.H. Sexton, and M. Webb, 2007: Projected increase in continental runoff due to plant responses to increasing carbon dioxide. Nature, 448, 1037-1042.

Blanco, H. P., J. Newell, L. Stott, M. Alberti, 2012: Water Supply Scarcity in Southern California: Assessing Water District Level Strategies. Los Angeles, CA: Center for Sustainable Cities, Price School of Public Policy, University of Southern California. http://sustainablecities.usc.edu/research/Chapter%203.%20LADWP%2012%2019%20p.pdf

Blankinship, J.C., M.W. Meadows, R.G. Lucas, and S.C. Hart, 2014: Snowmelt timing alters shallow but not deep soil moisture in the Sierra Nevada, Water Resourc. Res. 50, 1448-1456.

Budyko, M.I., and D.H. Miller, 1974: Climate and Life.International Geophysics Series, Vol. 18, Academic Press, 508 pp.

Cabré, M., S.A. Solman, and M.N. Nuñez, 2010: Creating regional climate change scenarios over southern South America for the 2020's and 2050's using the pattern scaling technique: validity and limitations, Clim. Change, 98, 449–469. doi:10.1007/s10584-009-9737-5.

Cai, W., S. Borlace, M. Lengaigne, P. van Rensch, M. Collins, G. Vecchi, A. Timmermann, A. Santoso, M. J. McPhaden, L. Wu, M. H. England, G. Wang, E. Guilyard, and F.-F. Jin, 2014: Increasing frequency of extreme El Niño events due to greenhouse warming. Nature Clim. Change, 4, 111–116, doi:10.1038/nclimate2100.

Caldwell, P.M., H.-N.S. Chin, D.C. Bader, and G. Bala (2009), Evaluation of a WRF based dynamical downscaling simulation over California. Clim. Change, 95, 499–521, doi:10.1007/s10584-009-9583-5.

Cayan, D.R., E.P. Maurer, M.D. Dettinger, M. Tyree, and K. Hayhoe, 2008: Climate change scenarios for the California region. Climatic Change, 87, 21–42, doi:10.1007/s10584-007-9377-6.

Cayan, D.R., S.A. Kammerdiener, M.D. Dettinger, J.M. Caprio, and D.H. Peterson, 2001: Changes in the onset of spring in the western United States, Bull. Am. Meteorol. Soc., 82, 399–416.

Cayan, D.R., T. Das, D. W. Pierce, T. P. Barnett, M. Tyree, and A. Gershunov, 2010: Future dryness in the southwest US and hydrology of the early 21st century drought. Proc. Nat. Aca. Sci., 107 (50), 21271-21276.

Cayan, D.R and J.O. Roads, 1984: Local Relationships between United States West Coast Precipitation and Monthly Mean Circulation Parameters. Mon. Wea. Rev., 112, 1276–1282.

Cayan, D.R., 1996: Interannual climate variability and snowpack in the western United States. Journal of Climate, 9, 928-948.

Chen, F., and J. Dudhia, 2001: Coupling an advanced land surface-hydrology model with the Penn State-NCAR MM5 modeling system. Part I: Model implementation and sensitivity. Mon. Wea. Rev., 129, 569-585.

Chiew, F.H.S., P.H. Whetton, T.A. McMahon, and A.B. Pittock, 1995: Simulation of the impacts of climate change on runoff and soil moisture in Australian catchments. Journal of Hydrolgy, 167, 121–147.

Christensen, N. S. and D. P. Lettenmaier, 2007: A multimodel ensemble approach to assessment of climate change impacts on the hydrology and water resources of the Colorado River Basin, Hydrol. Earth Syst. Sci., 11, 1417-1434.

City of Camarillo, 2010: Urban Water Management Plan 2010. Available at http://www.water.ca.gov/urbanwatermanagement/2010uwmps/Camarillo,%20City%20of/2010%20UWMP%20Final%20Draft.pdf

Collins, M., R. Knutti, J. Arblaster, J.-L. Dufresne, T. Fichefet, P. Friedlingstein, X. Gao, W.J. Gutowski, T. Johns, G. Krinner, M. Shongwe, C. Tebaldi, A.J. Weaver and M. Wehner, 2013: Long-term Climate Change: Projections, Commitments and Irreversibility. In: Climate Change 2013: The Physical Science Basis. Contribution of Working Group I to the Fifth

Assessment Report of the Intergovernmental Panel on Climate Change [Stocker, T.F., D. Qin, G.-K. Plattner, M. Tignor, S.K. Allen, J. Boschung, A. Nauels, Y. Xia, V. Bex and P.M. Midgley (eds.)]. Cambridge University Press, Cambridge, United Kingdom and New York, NY, USA.

Conil, S. and A. Hall, 2006: Local regimes of atmospheric variability: A case study of Southern California. Journal of Climate, 19, 4308-4325.

Cook, B.I., T.R. Ault, and J.E. Smerdon 2015: Unprecedented 21st century drought risk in the American Southwest and Central Plains. Science Advances, 1,1.

Cowling R.M., P.W. Rundel, B.B. Lamont, M.K. Arroyo, M. Arianoutsou, 1996: Plant diversity in Mediterranean-climate regions. Trends in Ecology and Evolution, 11: 362–366

Cowling, R.M., F. Ojeda, B.B. Lamont, P.W. Rundel, and R. Lechmere-Oertel, 2005: Rainfall reliability a neglected factor in explaining convergence and divergence of plant traits in fire-prone mediterranean-climate ecosystems. Glob. Ecol. Biogeogr. 14: 509–519.

Dai, A. 2013: Increasing drought under global warming in observations and models. Nature Climate Change, 3, 52-58.

Das, T., E. P. Maurer, D. W. Pierce, M. D. Dettinger, and D. R. Cayan, 2013: Increases in flood magnitudes in California under warming climates. J. Hydrol., 501, 101–110.

Dennison, P. E., S. C. Brewer, J. D. Arnold, and M. A. Moritz, 2014: Large wildfire trends in the western United States, 1984–2011, Geophys. Res. Lett., 41, 2928–2933.

Dettinger, M. D., and D. R. Cayan, 1995: Large-scale atmospheric forcing of recent trends toward early snowmelt runoff in California, J. Clim., 8, 606–623.

Dettinger, M.D., D.R. Cayan, M.K. Meyer, A.E. Jeton, 2004: Simulated hydrologic responses to climate variations and changes in the Merced, Carson, and American river basins, Sierra Nevada, California, 1900–2099. Clim. Change, 62, 283–317.

Dudhia, J., 1989: Numerical study of convection observed during the Winter Monsoon Experiment using a mesoscale two–dimensional model. J. Atmos. Sci., 46, 3077–3107.

Duffy, P. B., and Coauthors, 2006: Simulations of present and future climates in the western United States with four nested regional climate models, J. Clim., 19, 873–895.

Ek, M. B., K. E. Mitchell, Y. Lin, E. Rogers, P. Grunmann, V. Koren, G. Gayno, J.D. Tarpley, 2003: Implementation of Noah land surface model advances in the National Centers for Environmental Prediction operational mesoscale Eta model. Journal of Geophysical Research, 108 (D22), 8851.

Feng, S. and Q. Fu, 2013: Expansion of global drylands under a warming climate. Atmos. Chem. Phys., 13, 10 081–10 094, doi:10.5194/acp-13-10081-2013

Flannigan M.D., Krawchuck MA, de Groot WJ, Wotton BM, Gowman LM, 2009: Implications of changing climate for global wildland fire. Int J Wildland Fire 18:483–507.

Flaounas, E., P. Drobinski, M. Vrac, S. Bastin, C. LebeaupinBrossier, M. Stefanon, M. Borga, and J. Calvet, 2012: Precipitation and temperature space–time variability and extremes in the Mediterranean region: Evaluation of dynamical and statistical downscaling methods. Climate Dynamics, 40: 2687–2705. DOI: 10.1007/s00382-012-1558-y.

Fowler, H. J., S. Blenkinsop, and C. Tebaldi, 2007: Linking climate change modeling to impacts studies: Recent advances in downscaling techniques for hydrological modeling, Int. J. Climatol., 27(12), 1547 – 1578.

Giorgi, F., and L. O. Mearns, 1991: Approaches to regional climate change simulation: A review. Rev. Geophys., 29, 191–216.

Giorgi, F., C. S. Brodeur, and G. T. Bates, 1994: Regional climate change scenarios over the United States produced with a nested regional climate model, J. Clim., 7, 375–399.

Gutierrez JM, San-Martin D, Brands S, Manzanas R, Herrera S (2013) Reassessing statistical downscaling techniques for their robust application under climate change conditions. J Clim 26(1):171–188. doi:10.1175/ JCLI-D-11-00687.1

Hamlet, A., P. Mote, M. Clark, and D. Lettenmaier, 2005: Effects of temperature and precipitation variability on snowpack trends in the western United States. J. Climate, 18, 4545–4560.

Hara, M., T. Yoshikane, H. Kawase, and F. Kimura, 2008: Estimation of the Impact of Global Warming on Snow Depth in Japan by the Pseudo-Global-Warming Method. Hydrol. Res. Lett., 2, 61–64, doi:10.3178/hrl.2.61.

Hayhoe, K., and Coauthors (2004), Emissions pathways, climate change, and impacts on California. Proc. Natl. Acad. Sci. U. S. A., 101, 12422–12427.

Hidalgo H. G., M. D. Dettinger, D. R. Cayan, 2008: Downscaling with constructed analogues: daily precipitation and temperature fields over the Unites States, California Energy Commission technical report CEC-500-2007-123, 48 pp.

Hidalgo HG, Das T, Dettinger MD, Cayan DR, Pierce DW, Barnett TP, Bala G, Mirin A, Wood AW, Bonfils C, Santer BD, Nozawa T, 2009: Detection and attribution of streamflow timing changes to climate change in the Western United States. Journal of Climate 22:3838–3855.

Howat, I. M., and S. Tulaczyk, 2005: Climate sensitivity of spring snowpack in the Sierra Nevada, J. Geophys. Res., 110, F04021, doi:10.1029/2005JF000356.

Howitt, R.E., J. Medellin-Azuara, D. MacEwan, J. R. Lund, and D. A. Sumner, 2014: Economic Analysis of the 2014 Drought for California Agriculture. Center for Watershed Sciences, University of California, Davis, California. 20p. Available at <http://watershed.ucdavis.edu>.

Huang, G., Kadir, T. and F. Chung, 2012: Hydrological response to climate warming: The Upper Feather River Watershed, Journal of Hydrology, Volumes 426–427, 138-150.

Hughes M., A. Hall, R.G. Fovell, 2007: Dynamical controls on the diurnal cycle of temperature in complex topography. Climate Dynamics, 29, 277-292.

IPCC [Intergovernmental Panel on Climate Change]. 2014. Climate Change 2014: Impacts, adaptation and vulnerability. Part A: Global and Sectoral Aspects. Contribution of Working Group II to the Fifth Assessment Report of the Intergovernment Panel on Climate Change. Field C. B., V.R. Barros, D.J. Dokken, K.J. Mach, M.D. Mastrandrea, T.E. Bilir, M. Chatterjee, K.L. Ebi, Y.O. Estrada, R.C. Genova, B. Girma, E.S. Kissel, A.N. Levy, S. MacCracken, P.R. Mastrandrea, and L.L. White (eds.) Cambridge University Press, Cambridge, United Kingdom and New York, NY, USA, 1132 pp.

Jacquemin, B. and J. Noilhan, 1990: Sensitivity study and validation of a land surface parameterization using the HAPEX-MOBILHY data set, Bound.-Lay. Meteorol., 52, 93–134.

Jarvis, P. G., 1976: The interpretation of the variations in leaf water potential and stomatal conductance found in canopies in the field, Philos. Trans. R. Soc. London, Ser. B, 273, 593–610.

Kain, J. S., and J. M. Fritsch, 1990: A one-dimensional entraining/detraining plume model and its application in convective parameteriatons. J. Atmos. Sci., 47, 2784-2802.

Kanamitsu, M., and H. Kanamaru, 2007: Fifty-seven-year California reanalysis downscaling at 10 km (CaRD10). Part I: system detail and validation with observations. Journal of Climate, 20 (22), 5553–5571.

Kapnick, S., and A. Hall, 2010: Observed climate-snowpack relationships in California and their implications for the future. J. Clim. 23: 3446-3456, DOI:10.1175/2010JCLI203.1

Kawase, H., T. Yoshikane, M. Hara, F. Kimura, T. Yasunari, B. Ailikun, H. Ueda, and T. Inoue, 2009: Intermodel variability of future changes in the Baiu rainband estimated by the pseudo global warming downscaling method. J. Geophys. Res., 114, D24110, doi:10.1029/2009JD011803.

Khattak MS, Babel MS, Sharif M. 2011. Hydro-meteorological trends in the upper Indus river basin in Pakistan. Climate Research 46: 103–119.

Kim, J., and S. Jain, 2010: High-resolution streamflow trend analysis applicable to annual decision calendars: A western United States case study, Clim. Change, 102, 699–707, doi:10.1007/s10584-010-9933-3.

Kottek, M., Grieser, J., Beck, C., Rudolf, B., Rubel, F., 2006. World Map of the Köppen–Geiger climate classification updated. Meteorol. Z. 15, 259–263. doi:10.1127/ 0941-2948/2006/0130.

Le Quéré, C., R. Moriarty, R. M. Andrew, G. P. Peters, P. Ciais, P. Friedlingstein, S. D. Jones, S. Sitch, P. Tans, A. Arneth, T. A. Boden, L. Bopp, Y. Bozec, J. G. Canadell, F. Chevallier, C. E. Cosca, I. Harris, M. Hoppema, R. A. Houghton, J. I. House, T. Johannessen, E. Kato, A. K. Jain, R. F. Keeling, V. Kitidis, K. Klein Goldewijk, C. Koven, C. Landa, P. Landschützer, A. Lenton, I. Lima, G. Marland, J. T. Mathis, N. Metzl, Y. Nojiri, A. Olsen, W. Peters, T. Ono, B. Pfeil, B. Poulter, M. R. Raupach, P. Regnier, C. Rödenbeck, S. Saito, J. E. Salisbury, U. Schuster, J. Schwinger, R. Séférian, J. Segschneider, T. Steinhoff, B. D. Stocker, A. J. Sutton, T. Takahashi, B. Tilbrook, N. Viovy, Y.-P. Wang, R. Wanninkhof, G. Van der Werf, A. Wiltshire, and N. Zeng, 2015: Global Carbon Budget 2014. Earth System Science Data, 7: 47–85. doi:10.5194/essd-7-47-2015.

Leduc, S., Diamond, H.J., & Palecki, M.A., 2009: The United States Climate Reference Network (USCRN) annual report for the fiscal year 2009. NOAA/NESDIS National Climatic Data Center Report. http://www.ncdc.noaa.gov/crn/annual-reports.html

Leung L.R., Y. Qian, X. Bian, W.M. Washington, J. Han, J. Roads, 2004: Mid-century ensemble regional climate change scenarios for the western United States. Climatic Change 62, 75–113.

Leung, L.R., Y. Qian, X. Bian, 2003: Hydroclimate of the western United States based on observations and regional climate simulations of 1981-2000. Part I: seasonal statistics. Journal of Climate, 16, 1892-1911.

Lins, H.F, 2012: USGS Hydro-Climatic Data Network 2009 (HCDN-2009). U.S. Geological Survey Fact Sheet. 2012-3047. http://pubs.usgs.gov/fs/2012/3047.

Littell, J.S., D. McKenzie, D.L. Peterson, and A.L. Westerling. 2009: Climate and wildfire area burned in western U.S. ecoprovinces, 1916–2003. Ecol. Appl. 19:1003–1021.

Long Beach Water Department, 2010: Urban Water Management Plan. Available at http://www.water.ca.gov/urbanwatermanagement/2010uwmps/Long%20Beach%20Water%20Department/2010%20UWMP%20-%20Revised%20110915%20-%20FINAL.pdf

Mahrt, L. and M. Ek, 1984: The Influence of Atmospheric Stability on Potential Evaporation. Journal of Climate and Applied Meteorology, 23, 222–234. doi: http://dx.doi.org/10.1175/1520-0450(1984)023<0222:TIOASO>2.0.CO;2Mao, Y, B Nijssen, and DP Lettenmaier, 2015: Is climate change implicated in the 2013–2014 California drought? A hydrologic perspective. Geophys. Res. Lett., 42, 2805–2813. doi: 10.1002/2015GL063456.

Masiokas, M., R. Villalba, B. Luckman, C. Le Quesne and J.C. Aravena, 2006: Snowpack variations in the Central Andes of Argentina and Chile, 1951–2005. Large-scale atmospheric influences and implications for water resources in the region. J. Climate 19, 6334–6352.

Maurer, E. P., 2007: Uncertainty in hydrologic impacts of climate change in the Sierra Nevada, California, under two emissions scenarios, Clim. Change, 82, 309–325, doi:10.1007/s10584-006-9180-9.

Maurer, E. P., and H. G. Hidalgo, 2008: Utility of daily vs. monthly large-scale climate data: an intercomparison of two statistical downscaling methods, Hydrol. Earth Syst. Sci., 12, 551–563.

McCabe, G., and M. Clark, 2005: Trends and variability in snowmelt runoff in the western United States, J. Hydrometeorol., 6, 476–482.

Mesinger, F., and Coauthors, 2006: North American regional reanalysis, Bull. Amer. Meteor. Soc., 87(3), 343–360, doi:10.1175/BAMS-87-3-343.

Mlawer, E. J., S. J. Taubman, P. D. Brown, M. J. Iacono, and S. A. Clough, 1997: Radiative transfer for inhomogeneous atmospheres: RRTM, a validated correlated-k model for the lonwave. J. Geophys. Res., 102, 16663-16682.

Myers, N., R. A. Mittermeier, C. G. Mittermeier, G. A. B. da Fonseca, and J. Kent, 2000: Biodiversity hot spots for conservation priorities. Nature 403:853–858.

Nakanishi, M., and H. Niino, 2006: An improved Mellor-Yamada Level-3 model: Its numerical stability and application to a regional prediction of advection fog, Boundary-Layer Meteor., 119, 397–407, doi:10.1007/s10546-005-9030-8.

Neelin, J. D., B. Langenbrunner, J. E. Meyerson, A. Hall, and N. Berg, 2013: California winter precipitation change under global warming in the Coupled Model Intercomparison Project 5 ensemble. J. Climate, 26, 6238–6256.

New, M., 2002: Climate change and water resources in the southwestern Cape, South Africa. South African Journal of Science, 98: 369–376.

Niu, G.-Y., and Coauthors, 2011: The community Noah land surface model with multi-parameterization options (Noah-MP): 1. Model description and evaluation with local-scale measurements, J. Geophys. Res., 116(D12109), doi:10.1029/2010JD015139.

Pal J.S., Giorgi F, Bi X.Q., Elguindi N and others, 2007: Regional climate modeling for the developing world:the ICTP RegCM3

Pan, L.-L., S.-H. Chen, D. Cayan, M.-Y. Lin, Q. Hart, M.-H. Zhang, Y. Liu, J. Wang, 2011: Influences of climate change on California and Nevada regions revealed by a high-resolution dynamical downscaling study. Climate Dynamics, 37, 2005-2020.

Paton, F. L., H. R. Maier, and G. C. Dandy, 2013: Relative magnitudes of sources of uncertainty in assessing climate change impacts on water supply security for the southern Adelaide water supply system, Water Resour. Res., 49, 1643–1667, doi:10.1002/wrcr.20153.

Peters, G. P., R. M. Andrew, T. Boden, J. G. Canadell, P. Ciais, C. Le Quéré, G. Marland, M. R. Raupach, and C. Wilson, 2013: The challenge to keep global warming below 2 °C. Nature Climate Change, 3, 4-6.

Pierce, D. W. & Cayan, D. R, 2013: The uneven response of different snow measures to humaninduced climate warming. J. Climate 26, 4148–4167.

Pierce, D. W., T. Das, D. R. Cayan, E. P. Maurer, N. Miller, Y. Bao, and M. Tyree, 2013: Probabil-istic estimates of future changes in California temperature and precipitation using statistical and dynamical downscaling, Clim. Dyn., 40(3-4), 839–856, doi:10.1007/s00382-012-1337-9.

Qian, Y., S.J. Ghan, L.R. Leung, 2009: Downscaling hydroclimatic changes over the Western U.S. Based on CAM subgrid scheme and WRF regional climate simulations, International Journal of Climatology, 30, 675-693.

Qu, X., and A. Hall, 2014: On the persistent spread of snow-albedo feedback, Clim. Dyn., 42(1–2), 69–81, doi:10.1007/s00382-013-1945-z.

Rasmussen, R., C. Liu, K. Ikeda, D. Gochis, D. Yates, F. Chen, and E. Gutmann, 2011: High-resolution coupled climate runoff simulations of seasonal snowfall over Colorado: A process study of current and warmer climate, J. Clim., 24(12), 3015–3048.

Ratnam, J.V., S. K. Behera, S. B. Ratna, C. J. de W. Rautenbach, C. Lennard, J.-J. Luo, Y. Masumoto, K. Takahashi, and T. Yamagata, 2013: Dynamical Downscaling of Austral Summer Climate Forecasts over Southern Africa Using a Regional Coupled Model. J. Climate, 26, 6015–6032. doi: http://dx.doi.org/10.1175/JCLI-D-12-00645.1

Rauscher, S. A., J. S. Pal, N. S. Diffenbaugh, and M. M. Benedetti, 2008: Future changes in snowmelt-driven runoff timing over the western US, Geophys. Res. Lett., 35, L16703, doi:10.1029/2008GL034424.

Reclamation, 2013: Downscaled CMIP3 and CMIP5 Climate and Hydrology Projections: Release of Downscaled CMIP5 Climate Projections, Comparison with preceding Information, and Summary of User Needs. Prepared by the U.S. Department of the Interior, Bureau of Reclamation, Technical Services Center, Denver, Colorado. 47 pp.

Regonda, S. K., B. Rajagopalan, M. Clark, and J. Pitlick, 2005: Seasonal cycle shifts in hydroclimatology over the western United States, J. Clim., 18, 372–384.

Risbey, J.S. and D. Entekhabi, 1996: Observed Sacramento Basin streamflow response to precipitation and temperature changes and its relevance to climate impact studies J. Hydrol., 184, 209–223.

Robock, A., K.Ya. Vinnikov, G. Srinivasan, J.K. Entin, S.E. Hollinger, N.A. Speranskaya, S. Liu, A. Namkhai, 2000: The global soil moisture data bank. B. Am. Meteorol. Soc., 81 (6). 1281–1299.

Roos, M., 1991: A trend of decreasing snowmelt runoff in northern California. In: 59th Western Snow Conference, Juneau, AK, pp. 29–36.

Salathé Jr, E. P., L. R. Leung, Y. Qian, and Y. Zhang, 2010: Regional climate model projections for the State of Washington, Clim. Change, 102(1-2), 51–75.

Salathé Jr., E. P., R. Steed, C. F. Mass, P. H. Zahn, 2008: A High-Resolution Climate Model for the U.S. Pacific Northwest: Mesoscale Feedbacks and Local Responses to Climate Change, J. Clim., 21, 5708–5726, doi:10.1175/2008JCLI2090.1.

Sato, T., F. Kimura, and A. Kitoh, 2007: Projection of global warming onto regional precipitation over Mongolia using a regional climate model, J. Hydrology, 333, 144-154.

Schaake, J. C., V. I. Koren, Q.-Y. Duan, K. E. Mitchell, and F. Chen, 1996: Simple water balance model for estimating runoff at different spatial and temporal scales, J. Geophys. Res., 101, 7461–7475.

Schaefer, G.L, M. H. Cosh and T. J. Jackson, 2007: "The USDA Natural Resources Conservation Service Soil Climate Analysis Network (SCAN)", J. Atmos. Ocean. Technol, 24 (12),2073-2077.

Schär, C., C. Frei, D. Lüthi, and H. C. Davies, 1996: Surrogate climate-change scenarios for regional climate models. Geophys. Res. Lett., 23(6), 669–672. doi:10.1029/96GL00265.

Scheff, J. and D.M.W. Frierson, 2015: Terrestrial Aridity and Its Response to Greenhouse Warming across CMIP5 Climate Models. J. Climate, 28, 5583–5600. doi: 10.1175/JCLI-D-14-00480.1.

Schwartz, M., A. Hall, and F. Sun, 2016a: Mean surface runoff insensitive to warming in a key Mediterranean-type climate: a case study of the Los Angeles region. Submitted to J. Climate.

Schwartz, M., A. Hall, F. Sun, D. Walton, and N. Berg, 2016b: End-of-21st Century Changes to surface runoff timing and variability in the Sierra Nevada Mountain Range, in preparation.

Seager, R., M. Ting, C. Li, N. Naik, B. Cook, J. Nakamura, and H. Liu, 2013: Projections of declining surface-water availability for the southwestern United States. Nature Climate Change, 3, 482-486.

Seneviratne, S. I., et al. 2013: Impact of soil moisture-climate feedbacks on CMIP5 projections: First results from the GLACE-CMIP5 experiment, Geophys. Res. Lett., 40, 5212–5217.

Seneviratne, S.I., T. Corti, E.L. Davin, M. Hirschi, E.B. Jaeger, I. Lehner, B. Orlowsky, and A.J. Teuling, 2010: Investigating soil moisture-climate interactions in a changing climate: A review. Earth-Science Reviews, 99, 3-4, 125-161, doi:10.1016/j.earscirev.2010.02.004.

Sheffield, J., and E. F. Wood, 2008: Projected changes in drought occurrence under future global warming from multi-model, multi-scenario, IPCC AR4 simulations. Climate Dyn., 31, 79–105.

Skamarock, W.C., Klemp J.B., Dudhia J., Gill D.O., Barker D.M., Duda M.G., Huang X-Y, Wang W., Powers J.G., 2008: A Description of the Advanced Research WRF Version 3. NCAR Technical Note, NCAR/TN-475+STR.

Slack, J. R., A. M. Lumb, and J. M. Landwehr, 1993: Hydroclimatic data network (HCDN): A U.S. Geological Survey streamflow data set for the United States for the study of climate variation, 1874–1988, U.S. Geol. Surv. Water Resour. Invest. Rep. [CD-ROM], 93-4076.

Snyder, M. A., J. L. Bell, L. C. Sloan, P. B. Duffy, and B. Govindasamy, 2002: Climate responses to a doubling of atmospheric carbon dioxide for a climatically vulnerable region, Geophys. Res. Lett., 29(11), doi:10.1029/2001GL014431.

Spracklen, D. V., L. J. Mickley, J. A. Logan, R. C. Hudman, R. Yevich, M. D. Flannigan, and A. L. Westerling, 2009: Impacts of climate change from 2000 to 2050 on wildfire activity and carbonaceous aerosol concentrations in the western United States, J. Geophys. Res., 114, D20301.

Stewart, I. T., D. R. Cayan, and M. D. Dettinger, 2005: Changes toward earlier streamflow timing across western North America, J. Clim., 18, 1136–1155.

Stewart, I. T., D. R. Cayan, and M. D. Dettinger, 2004: Changes in snowmelt runoff timing in western North America under a 'Business as Usual' climate change scenario, Clim. Change, 63, 217–332.

Stewart, I. T., 2013: Connecting physical watershed characteristics to climate sensitivity for California Mountain Streams. Clim. Change, 116, 133‑148.

Sun F., D. Walton, and A Hall, 2015a: A hybrid dynamical–statistical downscaling technique, part II: End-of-century warming projections predict a new climate state in the Los Angeles region. Journal of Climate, 28, 4618-4636.

Sun, F., A. Hall, M. Schwartz, D. Walton, and N. Berg, 2016a: Twenty-First-Century Snowfall and Snowpack Changes over the Southern California Mountains. J. Climate, 29, 91–110.

Sun, F., A. Hall, M. Schwartz, D. Walton, and N. Berg, 2016b: Anthropogenic fingerprints of the Sierra Nevada snowpack change: mid-elevation loss vs. high-elevation gain. In preparation.

Swetnam, T. W., and J. L. Betancourt, 1998: Mesoscale disturbance and ecological response to decadal climate variability in the American Southwest, J. Clim., 11, 3128–3147.

Taylor, K. E., R. J. Stouffer, and G. A. Meehl, 2012: An overview of CMIP5 and the experiment design, Bull. Amer. Meteor. Soc., 93(4), 485–498, doi:10.1175/BAMS-D-11-00094.1.

Tebaldi, C., R. L. Smith, D. Nychka, and L. O. Mearns, 2005: Quantifying uncertainty in projections of regional climate change: A Bayesian approach to the analysis of multimodel ensembles, J. Clim., 18(10), 1524–1540, doi:10.1175/JCLI3363.1.

Thompson, G., P. R. Field, R. M. Rasmussen, and W. D. Hall, 2008: Explicit Forecasts of Winter Precipitation Using an Improved Bulk Microphysics Scheme. Part II: Implementation of a New Snow Parameterization, Mon. Wea. Rev., 136, 5095–5115, doi:10.1175/2008MWR2387.1.

Timbal, B., A. Dufour, and B. McAvaney,2003: An estimate of future climate change for western France using a statistical downscaling technique, Clim. Dyn., 20(7-8), 807–823, doi:10.1007/s00382-002-0298-9.

USDA Forest Service, 2009: The importance of streamflow in California's southern Sierra Nevada mountains: Kings River Experimental Watersheds. Albany, CA: U.S. Department of Agriculture, Forest Service, Pacific Southwest Research Station. 2 p http://www.fs.fed.us/psw/topics/-water/kingsriver/documents/brochures_handouts/Stream_Discharge_PUBLIC.pdf

van Vuuren, D.P., J. Edmonds, M. Kainuma, K. Riahi, A. Thomson, K. Hibbard, G. C. Hurtt, T. Kram, V. Krey, J.-F. Lamarque, T. Masui, M. Meinshausen, N. Nakicenovic, S. J. Smith, and S. K. Rose, 2011: The representative concentration pathways: an overview. Climatic Change, 109(1–2): 5–31. doi: 10.1007/s10584-011-0148-z.

Vicuna, S., E.P. Maurer, B. Joyce, J.A. Dracup, D. Purkey, 2007: The Sensitivity of California water resources to climate change scenarios J. Am. Water Resour. Assoc., 43, 482–498.

Walton D., F. Sun, A. Hall and S. Capps, 2015: A Hybrid Dynamical-Statistical Downscaling Technique, Part I: Development and Validation of the Technique. Journal of Climate, 28, 4597-4617.

Walton, D.W., A. Hall, N. Berg, M. Schwartz and F. Sun, 2016: Downscaled CMIP5 projections of elevation dependent warming and snow cover loss in California's Sierra Nevada. In review, Journal of Climate.

Washington, W. M., Weatherly, J. W., Meehl, G. A., Semtner A. J. Jr., Bettge, T. W., Craig, A. P., Strand W. G. Jr., Arblaster, J. M., Wayland, V. B., James, R., and Zhang, Y., 2000: Parallel Climate Model (PCM) Control and Transient Simulations, Clim. Dyn. 16, 755–774.

Westerling AL and BP Bryant, 2008: Climate change and wildfire in California. Climatic Change. 87:231–249.

Westerling, A. L., H. G. Hidalgo, D. R. Cayan, and T. W. Swetnam 2006: Warming and Earlier Spring Increase Western U.S. Forest Wildfire Activity. Science, 313, 940-943.

Willis, A.D., J. R. Lund, E.S. Townsley, and B. A. Faber, 2011: Climate change and flood operations in he Sacramento Basin, California. San Francisco Estuary Watershed Science, 9 (2), 1-17.

Wood, A. W., E. P. Maurer, A. Kumar, and D. P. Lettenmaier, 2002: Long-range experimental hydrologic forecasting for the eastern United States, J. Geophys. Res., 107(D20), 4429.

Wood, A. W., L. R. Leung, V. Sridhar, and D. P. Lettenmaier, 2004: Hydrologic implications of dynamical and statistical approaches to downscaling climate model outputs, Clim. Change 62,189–216, doi:10.1023/B:CLIM.0000013685.99609.9e.

Young, C.A., M. Escobar, M. Fernandes, B. Joyce, M. Kiparsky, et al., 2009: Modeling the Hydrology of California's Sierra Nevada for Sub-Watershed Scale Adaptation to Climate Change. J. Am. Water Resour. Assoc., 45 (6), 1409-1423.

Zhao, T., and A. Dai, 2015: The magnitude and causes of global drought changes in the 21st century under a low-moderate emissions scenario, J. Clim., 28(11), 4490–4512.

Ziervogel, G., P. Johnston, M. Matthew and P. Mukheibir, 2010: Using climate information for supporting climate change adaptation in water resource management in South Africa. Climatic Change,103: 537–554. DOI 10.1007/s10584-009-9771-3.